Improving the transport properties of InN thin films

A. Adikimenakis[1,*], K. Tsagaraki[1], M. Androulidaki[1], P. Chatzopoulou[3], G. P. Dimitrakopulos[3], Th. Kehagias[3], A. Kostopoulos[1,5], J. Kuzmik[4] and A. Georgakilas[1,2]

[1] Microelectronics Research Group (MRG), IESL, FORTH, 71110 Heraklion, Greece

[2] Department of Physics, University of Crete, P.O. Box 2208, GR-71003 Heraklion, Crete, Greece

[3] Physics Department, Aristotle University of Thessaloniki, GR 541 24 Thessaloniki, Greece

[4] Institute of Electrical Engineering, Slovak Academy of Sciences, 841 04 Bratislava, Slovakia

[5] Department of Electrical & Computer Engineering, Hellenic Mediterranean University (HMU), GR-71410 Heraklion, Greece

*adam@physics.uoc.gr

InN is a semiconductor predicted to provide optimum transport properties for high speed and high frequency electronic and optoelectronic devices. It exhibits the highest steady-state electron drift velocity among all semiconductors, with calculated values of about 5×10^7 cm/s [1]. However, electron transport in InN is limited by scattering from a high number of threading dislocations (TDs) in the heteroepitaxial InN layers, due to misfit strain relaxation and coalescence of relaxed crystallites. Moreover, the TDs of InN layers have been also considered to behave as unintentional donors, playing a significant role in the observed high electron concentration of InN layers.

In the present work we explore the optimization of the growth parameters of Plasma-Assisted Molecular Beam Epitaxy (PA-MBE) of InN thin films, in an effort to improve the crystalline quality of the films and reduce the TD density. We studied the correlation of InN structural and electrical properties with the growth temperature, within the upper 30°C of possible range, as well as the InN growth rate (G.R.). The results revealed a high sensitivity of the structural and electrical properties on the growth temperature [Figure 1] and, also, a smaller dependence on the growth rate. InN films with thicknesses of 600 -700 nm could be grown with electron mobility higher than 2,000 cm^2/Vs and carrier concentration of about 5×10^{17} cm^{-3}, although the TD density remains in the range of 10^{10} cm^{-2}. The InN layers with the highest measured dislocation densities exhibited also the highest bulk electron concentration and the lowest mobility values. The correlation of electron concentration and TD density, assuming TDs as exclusive sources of donors in InN, was not consistent with charged TDs being the exclusive source of unintentional donors in InN. Optical transmittance (T) measurements on a 3.7 μm InN film, grown under conditions resulting in low 10^{17} cm^{-3} electron concentration, indicated an optical bandgap of 0.623 eV at room temperature[2].

A 775 nm- thick InN (0001) film was grown under optimal growth conditions and 8-μm long and 4-μm wide resistors were fabricated with photolithography. I-V measurements were carried out in pulsed mode, in order to determine the electron velocity as a function of the applied electric field. A steady-state electron drift velocity of approximately 1×10^{8} cm s^{-1} at an electric field of 48 $kVcm^{-1}$ was determined [Figure 2], being the highest ever measured in a solid-state device[3].

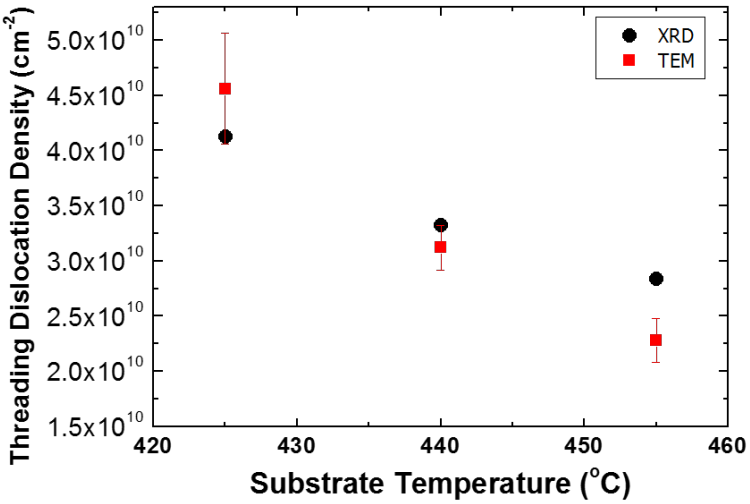

Figure 1: Dependence of TDD, determined by XRD and TEM, on growth temperature, for InN films grown with the same growth rate

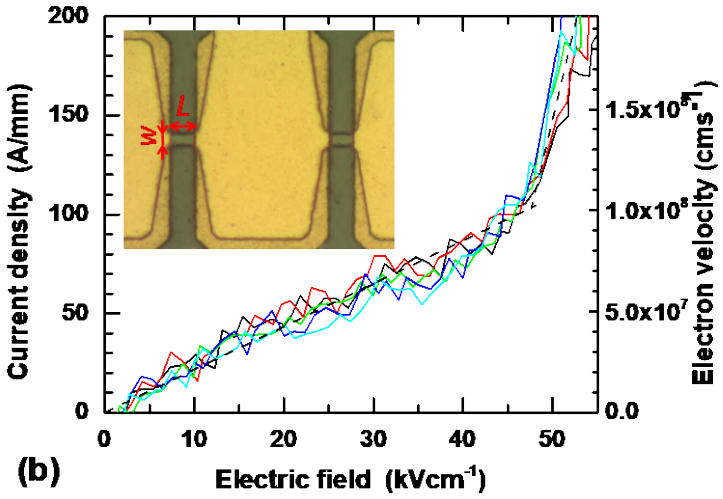

Figure 2: Current density and electron drift velocity as a function of the applied electric field for a 775 nm- thick InN film, grown under optimal growth conditions

[1] Z. Yarar, Phys. Stat. Sol. (b), 244, 3711 (2007)
[2] A. Adikimenakis et al, ECS J. Sol. St. Techn. 9, 015006 (2020)
[3] J. Kuzmík et al, AIP Advances 11, 125325 (2021)

Nonlinear analysis of electric current noise in nano-MOSFETs using Visibility Graphs

I.P. Antoniades[1,*], M.P. Hanias[2], S.G. Stavrinides[2], L. Magafas[2] and D. Tassis[1]

[1]Physics Department, Aristotle University of Thessaloniki, Thessaloniki, Greece

[2]Physics Department, International Hellenic University, St. Loucas Campus, Kavala, Greece

* iantoniades@auth.gr

It has been recently shown that noise in source-to-sink electric current in fully depleted nano-MOSFETS, especially when they are previously stressed (after a large gate voltage has been applied for a long time), does not only exhibit the well-known Brownian type noise, as expected by electron-hole recombination dynamics and phonon-electron interactions, but current fluctuations contain low-dimensional chaotic oscillations characteristic of complex systems exhibiting critical intermittent behavior[1,2,3]. In previous works, timeseries from such transistors have been analyzed with classical nonlinear analysis methods and Tsallis non-extensive statistics[2], as well as methods from the theory of critical phenomena[3]. In this work, we apply Complex Network Time-Series Analysis (CNTSA), using the Visibility Graph (VG) algorithm (described below) on timeseries coming both from stressed and fresh nano-MOSFETS. We look at graph metrics, such as the degree distribution, modularity, characteristic path length and clustering coefficient. A cross examination of such metrics for VGs generated from fresh and stressed MOSFET current timeseries, as well as various surrogate timeseries reveals consistent differences in the underlying dynamics (i) between fresh/stressed time-series, (ii) among time-series for different values of gate voltage, and (iii) between randomized surrogate timeseries and real ones. The degree distributions of all graphs show power law behavior (Fig. 1a). The above results provide additional proof for the presence of low-dimensional deterministic dynamics in the electric current fluctuations. It also suggests that CNTSA can be a useful tool in distinguishing among different chaotic or noisy series (Fig. 1b and Fig. 2) taking a 'fingerprint' of the underlying dynamics.

The Visibility Graph (VG) algorithm[4] introduced by Lacasa et al. in 2008, is one of several algorithms that constitute the CNTSA method[5]. According to this method, any timeseries (in general any sequence of ordered numbers) can be associated with a graph (complex network), by applying a predefined algorithm that assigns nodes and their interconnections (edges) to particular characteristics of the timeseries. It has been shown that topological and scaling aspects as well as temporal correlations of the underlying dynamical system are embodied in the graph structure and may be quantified by calculating any set of graph metrics such as degree, clustering coefficient, modularity, characteristic path length, diameter etc. In the VG algorithm, perhaps the most often used one in literature, given any sequence of N numbers $S(i)$, an unweighted, unidirectional graph is generated as follows: every sequence member corresponds to a node of the graph. Then, any pair of nodes i, j are connected *iff* j is 'visible' from i, i.e., if every point on the straight-line connecting series points $S(i)$ and $S(j)$ lies above all intermediate time series points $S(k)$ $(i<k<j)$. An example is shown in Fig. 3. It has been

shown that fractal time-series generate VG's that are scale free, *i.e.* have power-law degree distributions[4]. The Lyapunov exponent of a chaotic timeseries has been shown to be correlated with a graph metric known as the average local dimensionality[6]. More subtle characteristics of the underlying dynamics can also be depicted in other network metrics. For example, two chaotic time series yielding VG's of the same degree distribution may differ in their clustering coefficient distributions or modularity. In this sense, a VG may be used as novel method of taking a 'fingerprint' of the dynamical behavior.

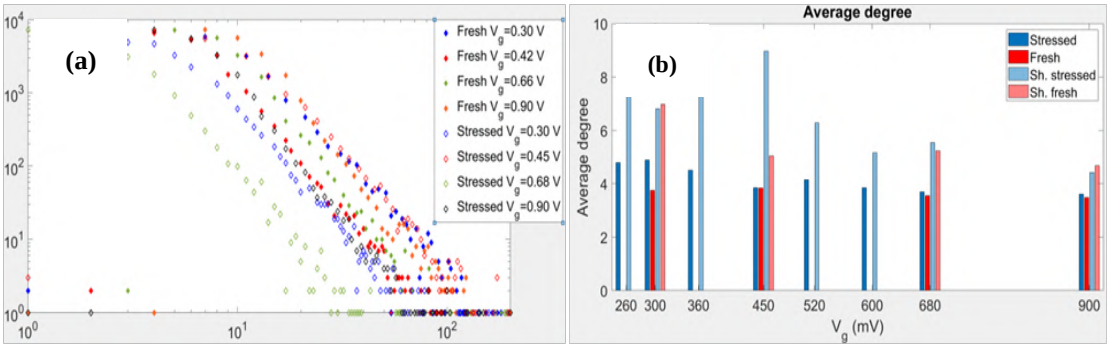

Fig. 1: (a) Degree distribution of various VGs generated from fresh and stressed transistor electric current time-series for various values of V_g (log-log scale). Distribution tails decay as a power law. (b) Average degrees of the same VGs contrasted with the average degrees of VGs generated by the respective shuffled surrogate time-series.

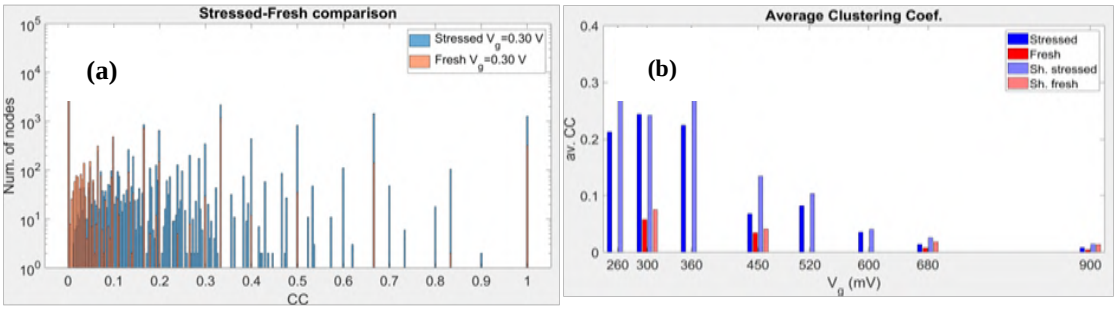

Fig. 2: (a) Clustering coefficient distribution comparison between VGs of current time-series from stressed vs. fresh MOSFETs for the same V_g value. (b) Comparison of average clustering coefficients of VGs for various V_g values with the respective averages of VGs generated by the respective shuffled surrogate time-series.

---

[1]Tassis, D.H., et al. "Chaotic behavior of random telegraph noise in nanoscale UTBB FD-SOI MOSFETs." IEEE Electron Device Letters 38.4 (2017): 517-520.
[2]Antoniades, I. P., et al. "Tsallis non-extensive statistics and multifractal analysis of the dynamics of a fully-depleted MOSFET nano-device." Physica A533 (2019): 121820.
[3]Contoyiannis, Y., et al. "Intermittency-induced criticality in the random telegraph noise of nanoscale UTBB FD-SOI MOSFETs." Microelectronic Engineering 216 (2019): 111027.
[4]L. Lacasa et al. (2008). From time series to complex networks: The visibility graph, PNAS 105 (13) 4972-4975
[5]J. Zhang and M. Small (2006). Complex Network from Pseudoperiodic Time Series: Topology versus Dynamics, Phys. Rev. Lett. 96, 238701.
[6]I.P. Antoniades et al. (2020). Complex Network Time Series Analysis of a Macroeconomic Model. In: Chaos and Complex Systems. Springer Proceedings in Complexity. Springer.

Theoretical investigation of the plasmonic properties of $SmCo_5$ nanomagnets

E. Antoniou[1,*], J. Kioseoglou[1] and H.M. Polatoglou[1]

[1]Department of Physics, Aristotle University of Thessaloniki GR-54124, Thessaloniki, Greece.

*eantonio@auth.gr

The use of nanomagnets in applications related to a variety of fields such as data storage[1], magnetic sensing[2], medicine and biology[3] is extremely interesting and promising. A lot of research has already been devoted to the synthesis of $SmCo_5$ nanomagnets and the study of their magnetic properties[4, 5, 6]. However, there is a lack of research efforts related to the plasmonic properties of nanomagnets. Our study is dedicated to the investigation of the plasmonic properties of $SmCo_5$ nanomagnets.

In particular, we first calculated the dielectric function of $SmCo_5$ in an energy range from 1 to 3 eV by conducting a series of atomistic Ab-initio simulations based on Density Functional Theory calculations. This energy range corresponds to a wavelength range for the incident electromagnetic wave from approximately 410 nm to 1240 nm which is also the part of the spectrum in which we look for plasmonic resonances in the nanomagnet models we used.

Additionally, we used the calculated dielectric function to search for plasmonic properties of $SmCo_5$ nanoparticles via the finite element method (FEM). For our simulations we designed and used models of spherical nanoparticles of different radii as well as nanoparticles of various sizes with a bipyramidal (with a pentagonal base) geometry.

The results of our calculations show that we can observe plasmonic resonances in the energy range from 1 to 3 eV, with a broad peak in the extinction cross section spectra for both geometries. We determine the sizes of the nanoparticles that are necessary for the plasmonic resonances to appear in the range of 410 nm to 1240 nm and also the anisotropy of the bipyramidal nanoparticles and its relation to the size and aspect ratio of the nanoparticles. In general, the results of our research can be particularly useful for the design and development of innovative applications that require the use of nanoparticles which combine magnetic[7] and plasmonic properties.

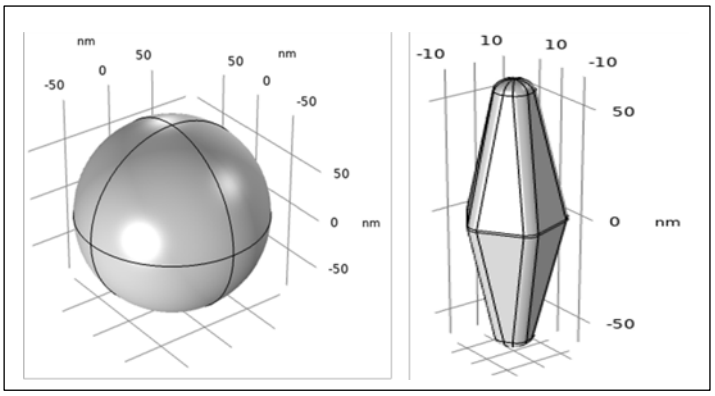

Fig. 1 The spherical nanoparticle of our simulations (left). The pentagonal geometry of nanoparticles used in our simulations (right).

[1] Yang, W. and Schmidt, H., Applied Physics Letters, 116(21), p.212401 (2020)
[2] Mekuria, T., Khalid, S., Krycka, K., Bleuel, M., Verma, H., Hong, H., Karna, S. and Seifu, D., AIP Advances, 10(6), p.065134 (2020)
[3] Guo, T., Lin, M., Huang, J., Zhou, C., Tian, W., Yu, H., Jiang, X., Ye, J., Shi, Y., Xiao, Y., Bian, X. and Feng, X., Journal of Nanomaterials, 2018, pp.1-8 (2018)
[4] Li, Q., Guo, J. and Sha, L., Materials Research Express, 5(3), p.035019 (2018)
[5] Li, C., Wu, Q., Ma, Z., Xu, H., Cong, L. and Yue, M., Journal of Materials Chemistry C, 6(31), pp.8522-8527 (2018)
[6] Gabay, A., Hu, X. and Hadjipanayis, G., Journal of Magnetism and Magnetic Materials, 368, pp.75-81 (2014)
[7] E. Antoniou, G. Sempros, M. Gjoka, C. Sarafidis, H.M. Polatoglou and J. Kioseoglou, Journal of Alloys and Compounds, Volume 882, 160699 (2021)

Flexible microheaters utilizing a combination of screen printing and inkjet printing technologies

Apostolos Apostolakis[1],* Dimitris Barmpakos[1], Aggelos Pilatis[1, 2], Dimitrios-Nikolaos Pagonis[2], Grigoris Kaltsas[1]

[1]microSENSES Laboratory, Department of Electrical and Electronics Engineering, University of West Attica, 122 43 Athens, Greece

[2]Department of Naval Architecture, University of West Attica, Egaleo 122 44, Athens, Greece

*apapostolakis@uniwa.gr

Fabrication of microheaters on flexible substrates is an attractive research topic mainly due to its wide application area [1]. Such devices have been utilized in IoT sensing applications, thermal flow sensing devices, biosensing devices, etc [2-4]. More specifically, graphene-based heaters have been utilized increasingly, as graphene has been established as an innovative material due to its excellent electronic, chemical, mechanical and thermal properties [5-6].

In the present work we demonstrate a microheater consisting of screen-printed silver electrodes (HPS-FG77 Silver Nanoflake Novacentrix (USA): Ag content 85 wt%), onto which graphene (Sigma Aldrich 793663: 2.4 wt% graphene and ethyl cellulose in cyclohexanone and terpineol) has been inkjet printed in five parallel lines, effectively forming a heating device on a Kapton substrate (Fig. 1). The heating area was approximately 1 cm^2. The substrate was pre-treated with 1M NaOH for 8 minutes, for increasing wettability; prior to printing, the substrate has been washed in an ultrasonic bath with DI water and isopropyl alcohol. I-V curves show ohmic behaviour and working electrical interface between the different printed materials (Fig. 2).

Following the electrical characterization, an experiment was set up to evaluate the operation of the devices as heaters. A constant current was provided and the corresponding voltage was measured. Furthermore, an IR camera (FLIR A655SC IR) was used to monitor temperature response to different power inputs (Fig. 3). As expected, the devices exhibited an almost linear temperature – power relationship (Fig. 4); an important finding is that Ag-Graphene contact does not exhibit hot spots, which leads to the conclusion that these materials can be effectively coupled for such application. It has been observed that the devices exhibit slightly different resistance, which in turn leads to different temperature – power relationship; this effect can be attributed to the ink-ink interface. The group is actively working on optimizing the overprinting technique, which will lead to more repeatable results.

References

[1] Dezhao Li et al., Micromachines, 7, 13 (2022).
[2] Woo-Jin Hwang et al., Sensors, 3, 11 (2011).
[3] Jonam Cho et al., Polymers, 8, 14 (2022).
[4] Z. E. Jeroise et al., Biomedical Microdevices, 3, 24 (2022).
[5] Chien-Ping Wang et al., Microelectronic Engineering, 228 (2020).
[6] Dimitris Barmpakos et al., Sensors, 3, 22 (2022).

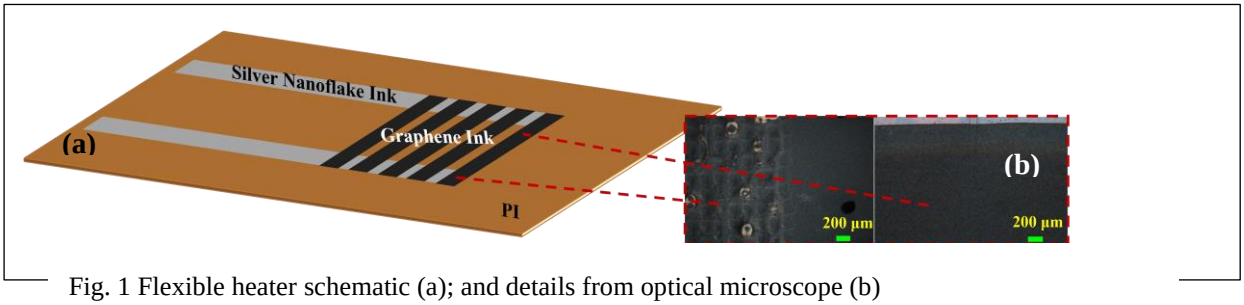

Fig. 1 Flexible heater schematic (a); and details from optical microscope (b)

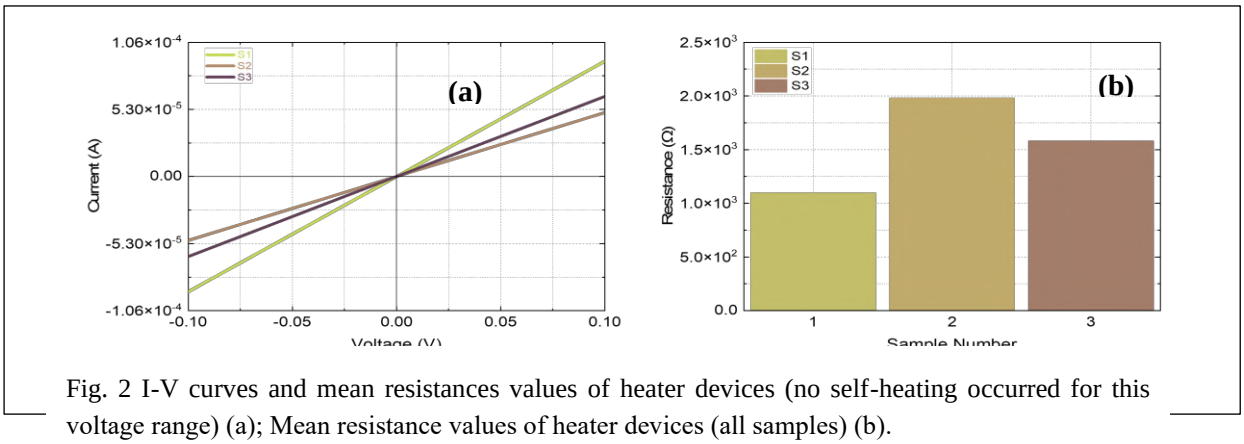

Fig. 2 I-V curves and mean resistances values of heater devices (no self-heating occurred for this voltage range) (a); Mean resistance values of heater devices (all samples) (b).

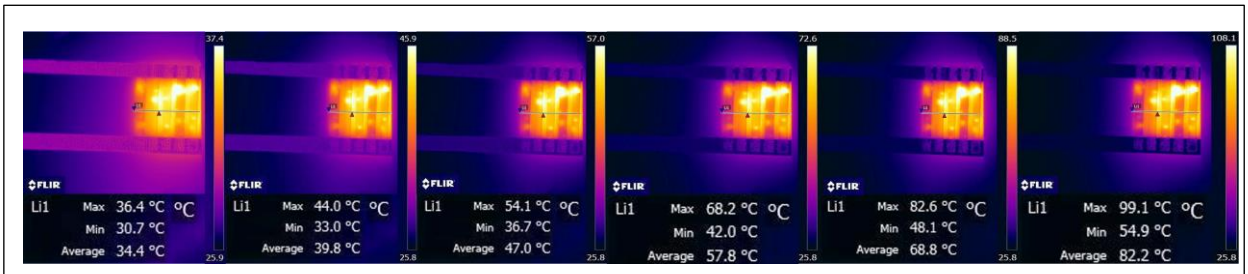

Fig. 3 Typical temperature increase in steps of increased power

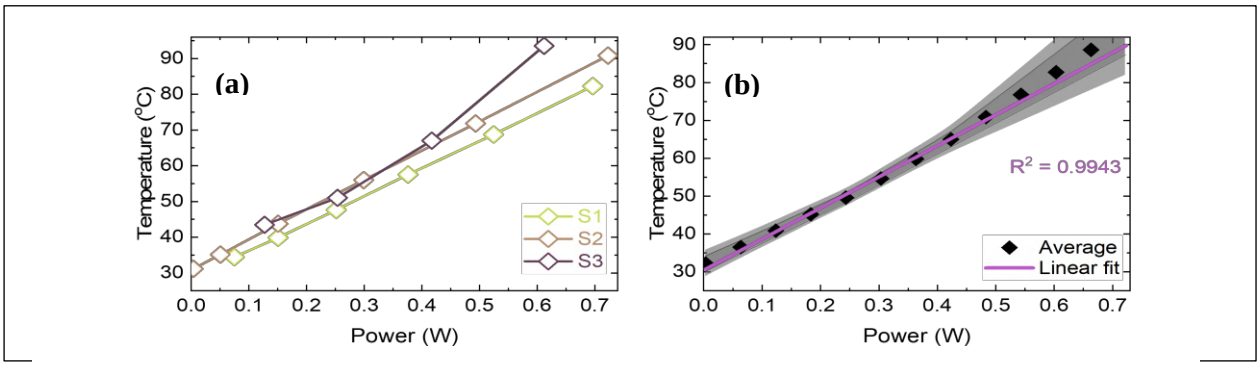

Fig. 4 Power-Temperature relationship for all samples (a); average of all samples with linear fit and std deviation band (light grey) and error band (dark grey) (b).

Void and Residual Silicon Dioxide Area: Their role on the Electrochemical Performance of Silicon Nanoparticles Encapsulated by Graphene

Dimitrios-Panagiotis Argyropoulos[1,*], George Zardalidis[1], Panagiotis Giotakos[2], Maria Daletou[2] and Filippos Farmakis[1]

[1]Democritus University of Thrace, Electrical and Computer Engineering, Xanthi, Greece

[2]Foundation of Research and Technology, Chemical Engineering Sciences, Patra, Greece

*dimiargy56@gmail.com

Silicon nanoparticles are used to enhance the anode specific capacity for the lithium-ion cell technology[1]. Due to the mechanical instability of silicon during lithiation and delithiation[2,3], an existing strategy is the enwrapping the silicon nanoparticles with graphene and the creation of a void area between them so as to accommodate the large volume modifications that occur in the silicon nanoparticle. This work aims to investigate the electrochemical performance and the associated kinetics of the hollow outer shell nanoparticles. To this end, we prepared hollow outer shell silicon nanoparticles (nps) enwrapped with graphene by using thermally grown silicon dioxide as a sacrificial layer, ball milling to enwrap silicon particles with graphene and hydro fluorine (HF) to etch the sacrificial SiO_2 layer. In addition, in order to offer a wider vision on the electrochemical behaviour of the hollow outer shell Si nps, we also prepared all the possible in-between process stages of nps and corresponding electrodes (i.e., bare Si nps, bare Si nps enwrapped with graphene, Si/SiO_2 nps and Si/SiO_2 nps enwrapped with graphene). The morphology of all particles revealed the existence of graphene encapsulation, void, and a residual layer of silicon dioxide depending on the process of each nanoparticle. Corresponding electrodes were prepared and studied in half cell configurations by means of galvanostatic cycling, cyclic voltammetry and electrochemical impedance spectroscopy. It was observed that nanoparticles encapsulated with graphene demonstrated high specific capacity but limited cycle life. In contrast, nanoparticles with void and/or SiO_2 were able to deliver improved cycle life. It is suggested that the existence of the void and/or residual SiO_2 layer limits the formation of rich Li_xSi alloys in the core silicon nanoparticle, providing higher mechanical stability during the lithiation and delithiation processes.

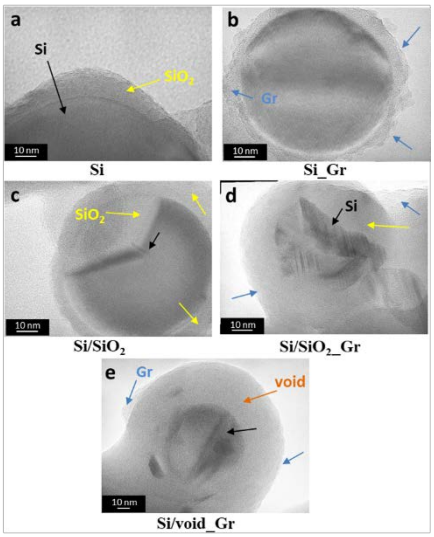

Figure 1: High Resolution TEM images of selected samples of (a) Si, (b) Si_Gr, (c) Si/SiO2, (d) Si/SiO2_Gr, and (e) Si/void_Gr powders. Black arrows: silicon, yellow arrows: SiO2, blue arrows: graphene layer, and orange arrow: void.

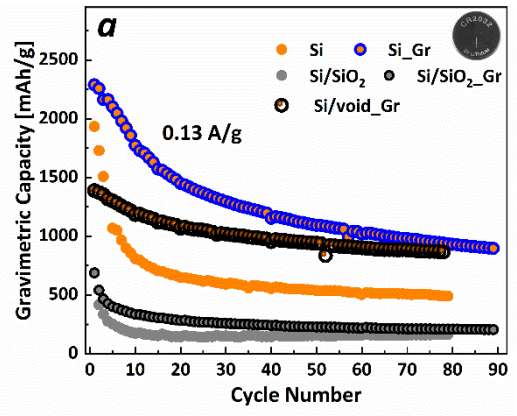

Figure 2: Discharge gravimetric specific capacity in (a) CR2032 coin-type half-cells.

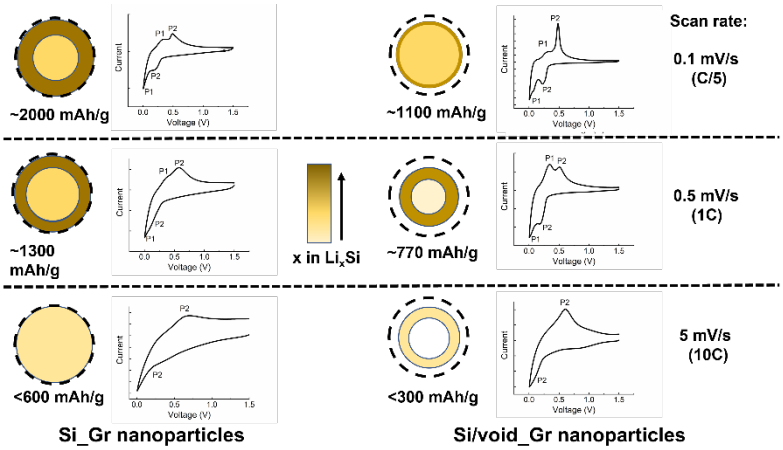

Figure 3: Schematic representation of the lithiated state at 0 V for Si_Gr and Si/void_Gr nanoparticles at various scan rates (and related C rates) with the corresponding voltammograms. The thickness of the various alloys, nanoparticles and voids is not to be considered as accurately defined

References:

1. Wu, H. & Cui, Y. Designing nanostructured Si anodes for high energy lithium ion batteries. *Nano Today* **7**, 414–429 (2012).
2. Iaboni, D. S. M. & Obrovac, M. N. Li 15 Si 4 Formation in Silicon Thin Film Negative Electrodes. *J. Electrochem. Soc.* **163**, A255–A261 (2016).
3. Yoon, T., Nguyen, C. C., Seo, D. M. & Lucht, B. L. Capacity Fading Mechanisms of Silicon Nanoparticle Negative Electrodes for Lithium Ion Batteries. *J. Electrochem. Soc.* **162**, A2325–A2330 (2015).

Heavy Metal Ion Detection in a Microfluidic Device combined with biosensors incorporating DNAzyme and Nanoparticles

M.K. Filippidou [1], A. Kanaris [1], S. Ntouskas [1], E. Aslanidis [2], E. Skotadis [2], D. Tsounidi [3], A. Rapesi [2, 3], G. Tsekenis [3], D. Tsoukalas [2], A. Tserepi [1], S. Chatzandroulis [1] *

[1] Institute of Nanoscience and Nanotechnology, NCSR ''Demokritos'', Aghia Paraskevi, Greece

[2] Department of Applied Sciences, National Technical University of Athens, Zografou, Greece

[3] Biomedical Research Foundation of the Academy of Athens, Athens, Greece

e-mail: s.chatzandroulis@inn.demokritos.gr

The presence of heavy metal ions, such as lead (Pb), cadmium (Cd) and mercury (Hg), in soil, air and water, constitutes an important global environmental threat, as these ions accumulate throughout the food chain causing chronic diseases [1, 2]. Conventional detection methods (i.e. high-performance liquid chromatography, HPLC) require bulky and expensive equipment, while the sample handling processes are usually time consuming, limiting their use to specially equipped laboratories. Thus, there is an urgent need for development of portable devices in order to replace or complement the conventional methods for detection of heavy metal ions. The solution can be provided by combining microfluidics technology[3] and electrochemical sensing [4, 5]. Such systems can be lightweight, portable, low cost and used in both laboratory and on-site measurements. Although some first efforts towards this direction have been proposed to date [6], yet there is still room for new approaches which can facilitate their uptake. In this work, we present a fast and easy to implement fabrication method based on photolithography on dry photosensitive layers, for the realization of a microfluidic based heavy metal ion detection device.

The device consists of a microfluidic mixing channel and a detection unit. In a square wave microfluidic channel with two inputs, passive mixing of the sample (i.e. water) with a buffer solution occurs prior to the detection of the heavy metal ions on biosensors. The mixing microchannel was designed to accommodate an effective mixing index over a wide range of flow rates on a small footprint [7], while the detection unit consists of 6 biosensors, each bearing interdigitated electrodes (IDEs). The fabrication process, schematically shown in Fig. 1, includes five main steps. Specifically, first an array of six IDEs is deposited on a Kapton substrate, consisting of an adhesive 10 nm thick Ti layer and 40 nm thick Au layer. The IDEs are patterned through lithography having inter-finger spacing of 10μm. Then, a 1st layer of a dry resist film is deposited on the Kapton substrate using a laminator (Fig 1 step A). Alongside, a 2nd layer of dry resist is laminated on a printed circuit board (PCB) (Fig 1 step B), to serve as a bonding layer between the two substrates (Kapton and PCB). Finally, the two substrates are bonded together, so that the PCB substrate improves the stability and the flatness of the flexible substrate, while simultaneously enables the handling of the device and the interconnection of the inlet and outlet of the solutions. A lithography step follows and the square microchannel is patterned on the 1st layer of dry resist (Fig 1 step C). Afterwards, platinum nanoparticles (PtNPs), having a mean diameter of 4 nm, are deposited between the IDEs using a modified DC magnetron sputtering system that allows the control of the PtNPs surface density. A PtNPs surface coverage close to 49% results in an interparticle distance of few nm, in which the DNAzymes will be placed. The resistance of the IDEs is approximately some hundreds of kΩ. The device is finally sealed with a polyolefin film bearing a silicone adhesive. The final device comprising a microfluidic channel and the 6 IDEs array is depicted in Fig. 2.

For the evaluation of the mixing unit, yellow and blue food coloring solutions enter the square microchannel. The resulting solution coming out of the channel outlet is green verifying the successful mixing of the two solutions. The absorbance spectra of these three solutions are depicted in Fig 3a. In particular, the main peak for the yellow solution is observed between 400-500 nm, for the blue colored solution at 600-650 nm, whereas

the green solution, being a combination of yellow and blue coloring, exhibits two main peaks at approximately 400-500 nm and 600-650 nm.

The biosensor operation principle is based on the fact that the presence of a metal ion will lead to the cleavage of the DNAzyme double strand and thus to a resistance increase, enabling the detection of heavy metal ions. A real time measurement of Pb^{2+} using the proposed DNAzyme biosensor is demonstrated in Fig 3b.

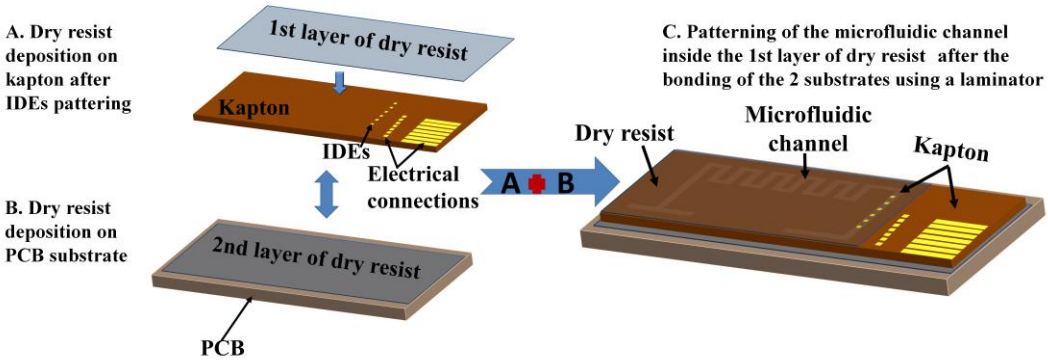

Figure 1. Schematic representation of the microfluidic channel fabrication process

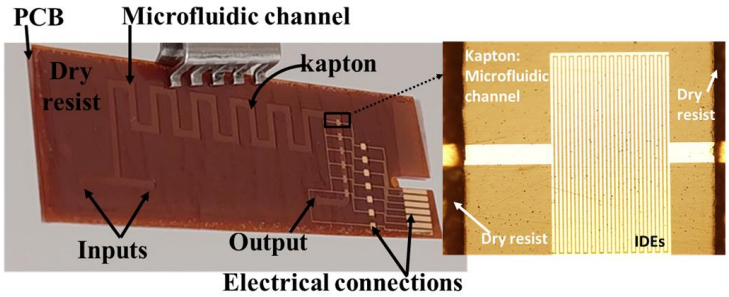

Figure 2. Final device image. Inset: optical microscopy image of the IDEs inside the microfluidic channel (10 x magnification).

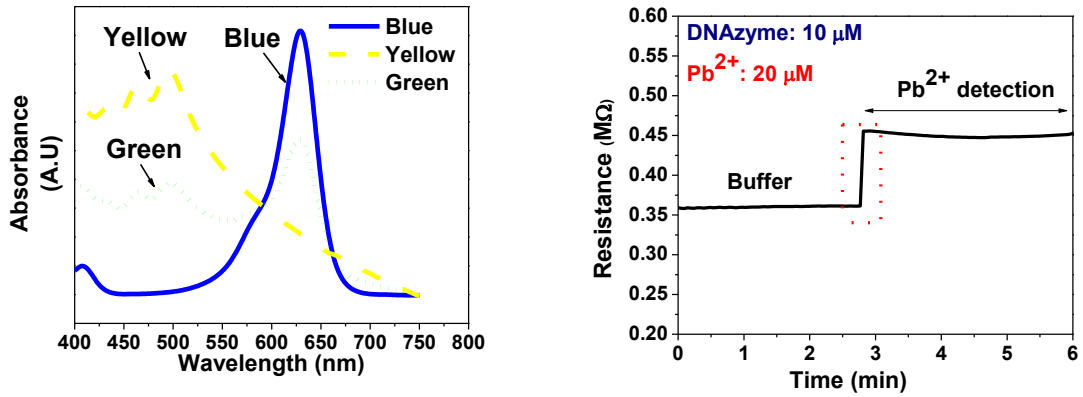

Figure 3. (a) Absorbance spectra of the starting blue and yellow solutions and the final (green) solution after mixing. **(b)** Real time measurement of Pb^{2+} using the proposed DNAzyme biosensor.

[1] G. Tsekenis, M.K. Filippidou, M. Chatzipetrou, V. Tsouti, I. Zergioti, S. Chatzandroulis, Sens. Actuators B: Chem., 208, 628(2015).
[2] H. Sharifi, J. Tashkhourian, B. Hemmateenejad, Sens. Actuators B: Chem., 359, 131551(2022).
[3] W.-H. Huang, V.-P. Mai, R.-Y. Wu, K.-L. Yeh, R.-J. Yang, Micromachines, 12, 1283(2021).
[4] M. Yuan, S. Qian, H. Cao, J. Yu, T. Ye, X. Wu, L. Chen, F. Xu, Food Chemistry, 382, 132173(2022).
[5] L.-L. Shen, G.-R. Zhang, W. Li, M. Biesalski, B.J.M. Etzold, ACS Omega, 2, 4593(2017).
[6] V. Karthik, B. Karuna, P.S. Kumar, A. Saravanan, R.V. Hemavathy, Chemosphere, 299, 134427(2022).
[7] X. Chen, T. Li, Z. Hu, Microsyst. Technol., 23, 2649(2017).

Heavy Metal Ion Detection using monolayer MoS_2 based and Pt nanoparticle based biosensors

E. Aslanidis[1,*], M. Kainourgiaki[1], E Skotadis[1], M. X. Tsigkourakos[1], A. Rapesi[1, 2], D. Tsounidi[2], G. Tsekenis[2] and D. Tsoukalas[1]

[1] Department of Applied Physics, National Technical University of Athens, 15780 Zografou, Greece

[2] Biomedical Research Foundation of the Academy of Athens, Athens, Greece

*evaaslani@central.ntua.gr

Heavy metal ions, such as Lead (Pb) and Mercury (Hg) could be a serious environmental threat when found in soil, air and water; thus their accurate and fast detection consists a major challenge. Several detection methods have been proposed in the literature such as High-performance liquid chromatography, but they are very expensive, time consuming and require specially equipped laboratories. In this work, we present two biosensing devices based on two different materials (Platinum nanoparticles (Pt NPs) and Molybdenum Disulfide (MoS_2), that are very fast, accurate and with a low limit of detection.

Pt NPs have proven to be a very precise sensing material for several applications while with the incorporation of DNAzymes they can detect heavy metal ions showing good sensitivity [1]. On the other hand MoS_2 has gained a lot of interest in recent years and it is a very good candidate for sensing heavy metal ions at very low concentrations [2]. Both devices were fabricated on oxidized silicon substrates. In the case of MoS_2 based biosensors the single-layer MoS_2 flakes were grown via CVD on a Si/SiO_2 (300nm) substrate using pure sulfur powder and an aqueous solution of sodium molybdate (Na_2MoO_4) as the S and Mo precursors respectively [3]. Ti/Au (4/40 nm) interdigitated electrodes (IDE) with electrode gap of 10 μm were formed on top of the MoS_2 flakes, using conventional photolithography and e-gun evaporation techniques. In the case of Pt NPs based biosensors, gold electrodes were deposited prior to the Pt NP deposition. Pt NPs were deposited using a modified DC magnetron system; the system allows control over Pt NPs diameter (herein 4 nm) as well as of surface coverage. In this case, NP surface coverage was 49% which is right below the percolation threshold and results in inter-particle distance of few nm.

Both biosensor devices were characterized by measuring their resistance change when a heavy-metal ion solution was drop-casted on the surface of the device. More specifically, at first buffer solution was drop-casted on top of the bio-sensors, while their resistance was constantly monitored using a Keithley 2400. This step was repeated until their resistance became immune to buffer addition. After the buffer-stabilization steps, a buffer solution containing a known heavy-metal ion concentration was drop-casted on the sensor, resulting in an increase in device resistance for both sensing-devices (Pt NPs and MoS_2). As a control experiment the sensors' response was recorded against known concentrations of Pb^{2+} and Hg^{2+} in the case of MoS_2 and Pt NP based devices respectively. Pt NPs – DNA based sensors managed to detect Pb^{2+} with concentration as low as 3 μM while they were immune to Hg^{2+} ions (Fig. 1). Pt NP based

biosensors implementing DNAzymes can be tuned to selectively detect only one ion, in our case Pb^{2+}, and be completely immune to any other ions due to their DNAzyme functionalization. On the other hand MoS_2 based biosensors managed to detect Pb^{2+} and Hg^{2+} in concentrations as low as 111 pM (Fig. 2a) and 700 pM (Fig. 2b) respectively, which is an order of magnitude less than the limit of detection for the Pt NPs based biosensors. However, the MoS_2 based biosensors are not selective since they respond to a variety of heavy metal ions [2]. The mechanisms controlling resistance change after analyte exposure for each of the devices described above will be discussed during the Conference.

This research has been co-financed by the European Regional Development Fund of the European Union and Greek national funds through the Operational Program Competitiveness, Entrepreneurship and Innovation, under the call RESEARCH – CREATE – INNOVATE (project code:T1EDK-03565)

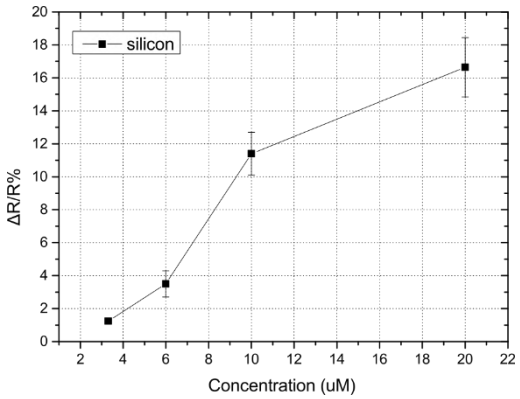

Fig. 1 PtNPs based devices ΔR/R% on Pb^{2+}

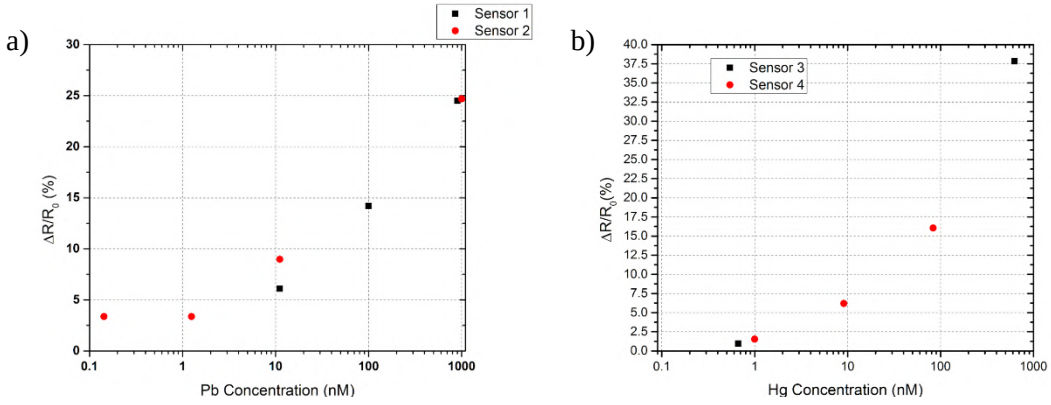

Fig. 2 MoS_2 based devices. a) ΔR/R% on Pb^{2+}, b) ΔR/R% on Hg^{2+}

[1] Skotadis E, et al. *Sensors and Actuators B: Chemical* 239 (2017): 962-969.

[2] Chang L, et al. Journal of Molecular Liquids 292 (2019): 111390.

[3] Tsigkourakos M, et al. Thin Solid Films 733 (2021): 138808.

Metal Oxide/Polymer Nanocomposites as Resist Materials

Georgia Geka [1,2], Konstantinos Kourtis[1], Eleni Makarona [2,*], George Papageorgiou [2], Andreas Germanos Karydas [3], Vassilis Psycharis [2], and Margarita Chatzichristidi [1,*]

[1] National and Kapodistrian University of Athens, Department of Chemistry, Athens, Greece

[2] NCSR "Demokritos", Institute of Nanoscience and Nanotechnology, Athens, Greece

[3] NCSR "Demokritos", Institute of Nuclear and Particle Physics, Athens, Greece

*mchatzi@chem.uoa.gr

*e.makarona@inn.demokritos.gr

Polymer nanocomposites (PNC's) are defined as polymers containing fillers with at least one external dimension smaller than 100 nm. The combination of the polymeric continuous phase and the nanoparticles discontinuous phase can modify and even enhance the mechanical, electric, and optical properties on the PNC's as compared with individual components [1]. A very promising class of materials to be used as nanofillers are metal oxides. Metal oxides are relatively easy to synthesize producing different nanostructures and nanoarchitectures that have been finding their way into a plethora of applications including sensors [2], "smart" textiles [3], bioengineering [4], catalysts [5], resists [6] e.t.c. Hydrothermal and solvothermal syntheses and growth techniques used for their production have gained significant popularity, since they are an inexpensive and facile means to obtain -through tuning of simple parameters- 3-dimensional nanostructures characterized by structural complexity, hierarchy and multiple functionalities.[7-8].

In this work, PNCs with CuO and NiO nanofillers are examined as lithographic resists in order to produce new, cost-efficient materials compatible with standard micro/nanofabrication techniques and which can become the core elements of novel devices. Firstly, CuO/PMMA nanocomposites investigated as a novel Electron Beam Lithography (EBL) resist material will be analyzed, followed by more recent studies of CuO/DNQ nanocomposites developed for optical lithography (OL). The CuO nanofillers used throughout this work were synthesized via hydrothermal synthesis, a low-cost solution-based method, which offers a high degree of design versatility through simple key parameters. Various combination of the specific parameters of the synthesis, e.g. concentration, temperature, duration of synthesis, etc., were tested in order to produce the adequate nanopowder for the production of the PNC. The EBL nanocomposites selected were evaluated as positive tone resists (Fig.1A), while the OL resists were examined for their suitability for both positive (Fig. 1B) and negative lithography. The studies were complemented by micro-X-ray fluorescence spectroscopy (μXRF) to investigate the miscibility of the nanofillers within the polymer matrix.

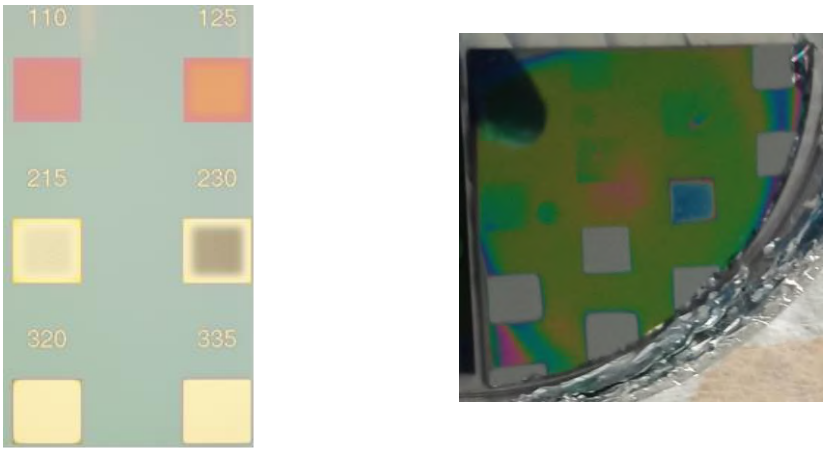

A) B)

Fig. 1: A) Optical microscope image of the contrast patterns of CuO/PMMA nanocomposite exposed in EBL used as a positive tone resist and B) Photography of the contrast patterns of CuO/AZ nanocomposite exposed at 365nm UV lamp used as a positive tone resist.

---

[1] Hussain, F., Hojjati, M., Okamoto, M., and Gorga, R.E., *J. Compos. Mater.* 40: 1511 (2006)
[2] Polymer-based Nanocomposites for Energy and Environmental Applications, Woodhead Publishing Series in Composites Science and Engineering, 2018, Pages 205-218
[3] Gowri, V.S.; Almeida, L.; De Amorim, M.T.P.; Pacheco, N.C.; Souto, A.P.; Esteves, M.F.; Sanghi, S.K., *J. Mater. Sci.*, 45, 2427 (2010)
[4] Balen, R.; da Costa, W.V.; Andrade, J.D.L.; Piai, J.F.; Muniz, E.C.; Companhoni, M.V.; Nakamura, T.U.; Lima, S.M.; Andrade, L.H.D.C.; Bittencourt, P.R.S.; et al., *Appl. Surf. Sci.*, 385, 257 (2016)
[5] Di Mauro, A.; Cantarella, M.; Nicotra, G.; Pellegrino, G.; Gulino, A.; Brundo, M.V.; Privitera, V.; Impellizzeri, *GSci. Rep.*, 7, 40895 (2017)
[6] Manouras, T.; Argitis P., *Nanomaterials*, 10, 1593 (2020)
[7] Botsi, S.; Tsamis, C.; Chatzichristidi, M.; Papageorgiou, G.; Makarona, E., *Nano-Struct. Nano-Objects*, 17, 7 (2019)
[8] Constantoudis, V.; Ioannou-Sougleridis I.; Dimou, A.; Ninou, A.; Chatzichristidi, M.; Makarona, E.; *MNE* 16, 100148 (2022)

New fluoropolymer for surface modification via UV exposure

Christina Kasoutsa[1], Theodore Manouras[2], Maria Vamvakaki[2,3], Panagiota Petrou[4]and Margarita Chatzichristidi[1,*]

[1] National and Kapodistrian University of Athens, Department of Chemistry, Industrial Chemistry Lab, Athens, Greece

[2] Foundation for Research and Technology-Hellas, Institute of Electronic Structure and Laser, Heraklion, Crete, Greece

[3] University of Crete, Department of Materials Science and Technology, Heraklion, Crete, Greece

[4] NCSR Demokritos, INRASTES, Immunoassay/Immunosensors Lab, AghiaParaskevi, Greece

*mchatzi@chem.uoa.gr

Polymers are widely used as biomaterials in bio-applications. The ability to modify the polymeric surface is of hight importance because in this way the bulk of the polymer can have different properties from its surface. Surface modification of polymers can be achieved via physico-chemical, mechanical or biological methods [1]. Among them, radiation, a physico-chemical method, is widely used and includes treatment by laser, e-beam, plasma, or UV irradiation, etc. [2,3]. UV irradiation is an easy applicable and rather inexpensive method. A UV lamp can be found in most labs and optical lithography is a quite popular and straight-forward to apply technique [4]. From the vast pool of polymers with different properties existing there is a class of polymers with very interest properties: the fluoropolymers. Fluoropolymers have excellent bulk properties, i.e., high chemical resistivity, thermal stability, low electrical conductivity and low friction coefficients, and in addition they have the ability to controllably change their physicochemical properties upon treatment with light, temperature, pH, etc. [5]. Fluoropolymers are already used in bio-applications like controlled drug delivery, tissue engineering, microfluidic, artificial muscle actuators, etc [6].

In this study fluoropolymers surfaces are modified via UV light for bio-applications. The polymers, a homopolymer and two copolymers, were synthesized via ATRP and evaluated as potential materials for surface modification through optical lithography. The monomer has on its side chain a fluorinated carbon which can be cleaved from the polymer in the presence of acid and heat. Consequently, by adding a photoacid generator in these materials, it is possible to change the chemistry of the surface in specific areas by UV irradiation using a binary mask (UV light produces acid only in the exposed areas of the films). In order to improve the film properties (e.g., better surface adhesion), two random copolymers containing different monomers were synthesized. The characterization of the fluorinated homopolymer and copolymers films in terms of solubility, wettability, refractive index and biomolecule

physisorption properties before and after exposure to UV radiation were investigated. It was found that the homopolymer provided the highest difference in wettability, refractive index and biomolecule physisorption between the exposed and unexposed film areas. Thus, this polymer will be further evaluated for biological applications requiring site-directed immobilization of biomolecules.

a) b)

Fig. 1: Photograph of the contrast patterns of the homopolymer a) before and b) after exposure at 254nm and thermal treatment

[1]S. K.Jaganathan, A. Balaji, M. V.Vellayappan, A. P. Subramanian, A. A.John, M.K.Asokan, E.Supriyanto, *J. Mater. Sci.* 50, 2007(2015)
[2]O.Nedela, P.Slepicka and V.Švorcík, *Materials*, 10, 1115, (2017)
[3]I.U. Ahad, A.Bartnik, H.Fiedorowicz, J.Kostecki, B.Korczyc, T.Ciach, D.Brabazon, J. Biomed. *Mater. Res. A*, 9, 102A (2014)
[4]P. Pavli, P.S. Petrou, D. Niakoula, A.M. Douvas, M. Chatzichristidi, S.E. Kakabakos, D. Dimotikali, P. Argitis, *Microelectron. Eng.*,86, 1473(2009)
[5]E. T. Kang and Y. Zhang, *Adv. Mater*., 20,12, (2000)
[6]V. F. Cardoso, D. M. Correia, C. Ribeiro, M. M. Fernandes and S.Lanceros-Méndez, *Polymers*, 10, 161, (2018)

Structural properties and behavior of threading dislocations in high mobility InN epilayers

P. Chatzopoulou[1], A. Adikimenakis[3], Th. Kehagias[1], Ph. Komninou[1], A. Georgakilas[2,3], and G. P. Dimitrakopulos[1,*]

[1]Electron Microscopy Laboratory, Physics Department, Aristotle University of Thessaloniki, Greece

[2] Microelectronics Research Group (MRG), IESL, FORTH, 71110 Heraklion Crete, Greece

[3] Department of Physics, University of Crete, Heraklion, Greece

*gdim@auth.gr

InN provides an excellent candidate to use as n-type MOSFET transistor channel in THz microwave sources due to its supreme low-field electron mobility at room temperature, estimated at 8,700 cm^2/Vs. For comparison, the respective mobilities of equally doped ($N\sim10^{17}$ cm^{-3}) GaN and AlN were calculated at 850 cm^2/Vs and 130 cm^2/Vs respectively[1]. However, InN device technology is still hampered by difficulties in preparing high-quality films, owing to the lack of suitable native substrates and low dissociation temperature. The degradation of electron transport properties is mainly attributed to high densities of threading dislocations (TDs) in the order of 10^9-10^{10} cm^{-2} that act as unintentional donors and charged scattering centres. Reducing TD density to 10^8 cm^{-2} is presumed to be sufficient for attaining the theoretical values of electron mobility[2].

TDs in InN evolve from the coalescence of misoriented grains and from strain relaxation, accompanying the formation of misfit dislocations (MDs). So far, the mechanisms involved in strain relaxation and TD density reduction in InN epilayers have not been fully elucidated. Herein, we investigate TD properties in (0001) InN/GaN state-of-the-art epilayers, including the mechanisms of strain relief, the formation of TDs and their reduction rate in connection to the growth conditions, and their role in the film surface morphologies. We have considered samples grown under stoichiometric In/N flux ratio, at varying growth temperatures (T_{gr}) and rates (R_{gr}), which provide sufficient adatom diffusion lengths and step-flow growth[3]. TEM and high-resolution TEM (HRTEM) observations were performed and were combined with conductivity and Hall-effect measurements. Structural and surface properties were also investigated by high-resolution XRD, SEM and AFM.

The InN films relaxed fully after 600 nm of growth by the introduction of MD arrays. In the 40 - 600 nm thickness range, the MD density increased gradually without appearance of extra TD arms, indicating introduction of MDs by basal slip or by atomic rearrangements, instead of the classical Matthews-Blakeslee glide mechanism. Combined plan-view and cross-sectional TEM observations revealed that **a**-type TDs presented a density in the range of 10^{10} cm^{-2} and were introduced at coalescence sites of mosaic columns. Increasing the adatom diffusion length by the increase of T_{gr} and/or decrease of R_{gr}, was found to lead to a reduction in TD density due to

the increase of the width of the mosaic columns. Low T_{gr} promoted stacking irregularities near the interface, as shown in Fig. 1c, which can provide new TD nucleation sites (Fig. 1b). TD densities were measured at different heights inside the epilayers and presented an exponential decay behaviour. The TD density fall-off was driven by reactions between edge-type TDs including mutual TD annihilation and fusion of two TDs to one. It was also found that the rate of TD density reduction increased with surface roughness which promotes TD inclination.

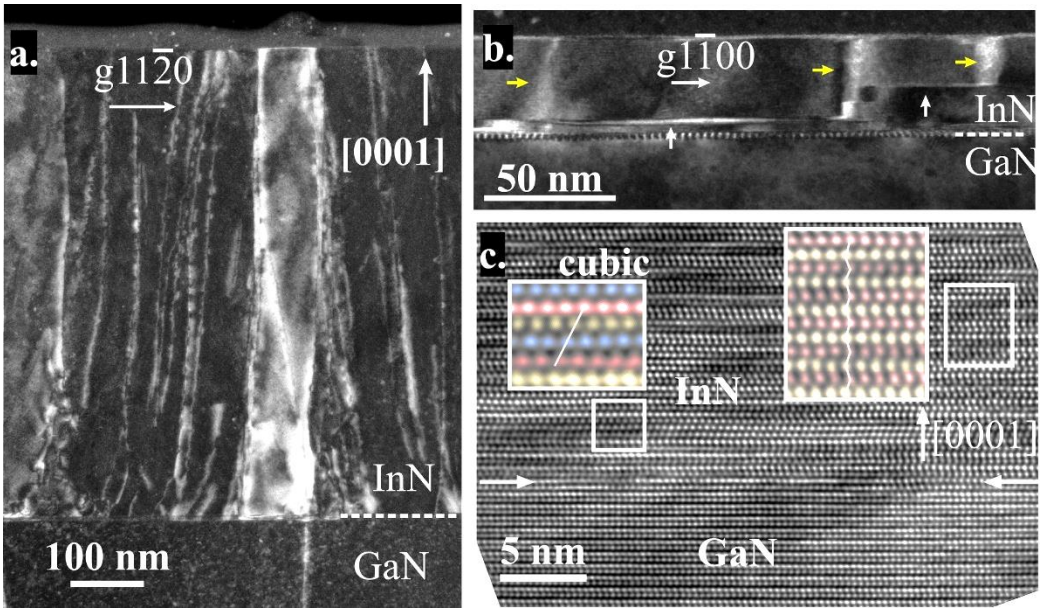

Fig. 1. **a.** Cross sectional weak beam dark field TEM image taken near the [1$\bar{1}$00] zone axis under *g*/3*g* conditions using *g*11$\bar{2}$0, showing the TDs inside the epilayer **b.** Cross sectional weak beam dark field TEM image taken near the [11$\bar{2}$0] zone axis using *g*1$\bar{1}$00, showing the emanation of a-type TDs (yellow arrows) from basal stacking faults (white arrows) **c.** HRTEM image along the [11$\bar{2}$0] zone axis, from a sample grown at low T_{gr} showing the hexagonal (ABABAB) and cubic (ABCABC) stacking sequencies observed near the interface.

ACKNOWLEDGEMENTS

Work partially supported by EU's H2020 European Research Infrastructure NFFA-Europe (grant n. 654360). Work continued by partial support from IESL/FORTH, including the projects "AENAO" (MIS 5002556) and "INNOVATION-EL" (MIS 5002772).

[1] P. Siddiqua, W. A. Hadi, M. S. Shur, S. K. O'Leary, J. Mater. Sci: Mater. Electron., 26, 4475 (2015)
[2] N. Miller E. E. Haller, G. Koblmuller, C. Gallinat, J. S. Speck, W. J. Schaff, M. E. Hawkridge, K. M. Yu, J. W. Ager, Phys. Rev. B, 84, 075315 (2011)
[3] A. Adikimenakis, P. Chatzopoulou, G. P. Dimitrakopulos, Th. Kehagias, K. Tsagaraki, M. Androulaki, G. Doundoulakis, J. Kuzmik, A. Georgakilas, ECS J. Solid State Sci. Technol. 9, 015006 (2020)

Temperature characterization and modeling of FORTH GaN HEMT using Y-Function methodology

Nikolaos Makris[1,2], Loukas Chevas[1], Maria Kayambaki[2], Athanasios Kostopoulos[2,*], Antonios Stavrinidis[2], George Konstantinidis[2] and Matthias Bucher[1]

[1]Technical University of Crete, School of Electrical & Computer Engineering, Chania, Greece

[2]Foundation for Research and Technology-Hellas, Institute of Electronic Structure and Laser, Heraklion, Greece

[*]Hellenic Mediterranean University, Department of Electrical & Computer Engineering, Heraklion,Greece

nmakris@iesl.forth.gr / bucher@tuc.gr

GaN High Electron Mobility transistors (HEMTs) are becoming popular for analog and RF applications especially in harsh environments due to their high thermal conductivity, high electron mobility and robustness. Device characterization and extraction of important device parameters such as threshold voltage or effective mobility is significant for technology optimization and device modeling. In this work, we use the Y-function technique in order to determine FORTH GaN HEMT's threshold voltage, low field mobility and mobility degradation factor for temperatures between -30 and 110ºC.

The device under test is a wide-long (W=250um , L=3um) AlGaN/GaN HEMT fabricated by IESL-FORTH utilizing optical lithography with Ti/Al/Ni/Au ohmic drain/source contacts, Ni/Au Schottky gate and SiN passivation. On-wafer measurements were carried out at the Electronics Laboratory of TUC using a HP 4142B Modular DC Source/Monitor for the DC measurements and a Temptronic TPO3000 for the temperature control. Keysight's ICCAP and Python programming language were used for the measurement setup and analysis respectively.

Y-function methodology[1] has been used widely in different types of MOSFETs. Recent contributions demonstrate extracted mobility and threshold voltage utilizing Y-function in HEMTs [2] [3] .

Considering that the device operates in linear region and above threshold voltage, the current is calculated as[1], $I_{DS} = \frac{\beta(V_{GS}-V_T)}{(1+\theta\ (V_{GS}-V_T))}$ where $\beta = \frac{\mu C_b W}{L}$,μ is low field mobility, Cb is the capacitance per area due to the AlGaN layer, V_T is the threshold voltage and θ the mobility degradation factor. So, $Y = {I_{DS}}/{\sqrt{g_m}} = \sqrt{\frac{\mu C_b W V_{DS}}{L}}\ (V_{GS} - V_T)$. From the application of Y function in transfer characteristics for V_{DS}=20mV, we determine mobility and threshold voltage from their linear section (Fig. 1(a)). θ is extracted from the saturated values of [2] $\theta_y = \frac{\beta V_{DS}}{I_{DS}} - \frac{\sqrt{\beta V_{DS}}}{Y}$. From this factor, considering that there is no degradation of mobility due to vertical field, we would be able to determine device series resistance (Fig. 1(b)).

The results are depicted in Fig.2. Mobility and θ decrease monotonically with temperature. Threshold voltage rises ~200mV from -30º to 100 ºC. The mobility and V_{TH} are in good agreement with results extracted using a charge-based approach [4]. To evaluate the extracted parameters, we applied them to the current equation. The model is in good agreement with measurements.

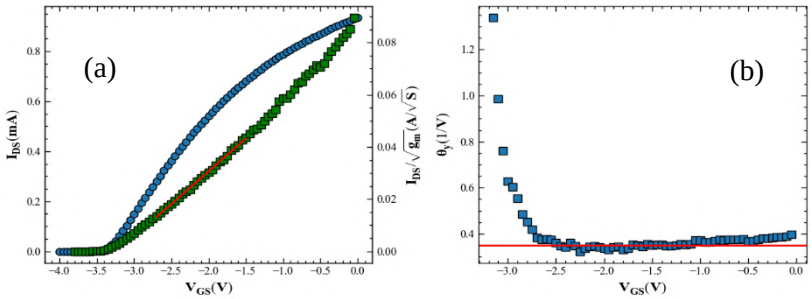

Fig. 1 (a) Transfer characteristic(circles) and Y function(squares) (b) θ_y extraction vs V_{GS}(V) @ V_{DS}=20mV and T=30ºC. Red lines denote the extraction areas/values.

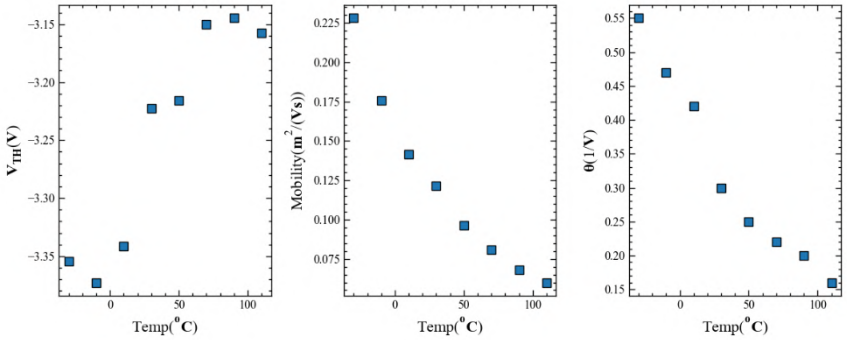

Fig. 2 from left to right, extracted threshold voltage, low field mobility and mobility degradation factor.

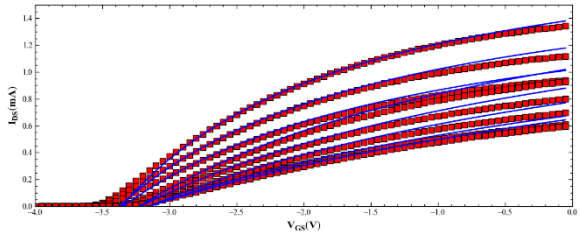

Fig. 3 Measured transfer characteristics (red) vs model (blue). @ V_{DS}=20mV

We acknowledge support of this work by the project "National Infrastructure in Nanotechnology, Advanced Materials and Micro-/Nanoelectronics (INNOVATION-EL)" (MIS 5002772) which is implemented under the Action "Reinforcement of the Research and Innovation Infrastructure" of the Operational Programme "Competitiveness, Entrepreneurship and Innovation" (NSRF 2014-2020), co-financed by Greece and the European Union (European Regional Development Fund).
This research has been co-financed by the European Regional Development Fund of the European Union and Greek national funds through the Operational Program Competitiveness, Entrepreneurship and Innovation, under the call RESEARCH – CREATE – INNOVATE (project code: T2EDK-00340).

[1] G. Ghibaudo, Electron. Lett., 24, 1988(543-545)
[2] R. K. Kammeugne et al., EUROSOI-ULIS, 2020(1-4)
[3] D. Kim et. al, Solid-State Electron., 197, 2022(108448)
[4] L. Chevas et.al, LAEDC, 2022

Overview of Total Ionizing Dose Degradation Mechanisms as Observed in 65nm Bulk-CMOS MOSTs

Loukas Chevas, Nikolaos Makris and Matthias Bucher

Technical University of Crete, School of Electrical & Computer Engineering, Chania, Greece

lchevas@tuc.gr / mbucher@tuc.gr

Semiconductors have long been known to suffer degradation of their operation when subjected to ionizing radiation. Their functionality is affected mainly in two ways, Single Event Upsets, such as bit flips in memories and accumulated damages due to a large dose absorbed over time, often called Total Ionizing Dose damage. This work focuses on the latter. While ionizing radiation can imply both particles and photons, in this work we will analyze the effects of ultrahigh doses (up to $1Grad_{SiO2}$) of high energy (50keV) X-rays on a commercially available 65nm bulk CMOS technology. Irradiated device data were provided to TUC by CERN as part of the High Luminosity LHC upgrade efforts for the purpose of characterization and compact model parameter extraction.

At the X-ray energy levels used in these experiments, the photoelectric effect is the main mechanism through which photons interact with Si and O atoms of the semiconductor's oxides. An electron is kicked off from the innermost (K) shell, with an L shell one dropping to fill the vacancy (initial e^--h^+ production). Electrons have higher relative mobilities than holes in the oxides, especially under external biasing fields, and thus are quickly removed from the oxide. Holes on the other hand move much more slowly and can migrate by polaron hopping towards the channel-oxide interface where they can become trapped (as fixed trapped positive charge) or, during this process, dislodge H atoms trapped in the SiO_2 or depassivate Si-H bonds in the channel-oxide interface, where the Hydrogen is a by-product of the manufacturing process. Thus even larger and slower (H^+/protons) charges are generated and slowly migrate towards the oxide interface, where by the depassivation of Si-H border traps are created (the free H^+ liberates the H from the Si atom and leaves as neutral H_2). Band structure and external biasing determine the trap's charge, in NMOS the majority being negative and in PMOS positive. The result is a net positive trapped charge accumulation in PMOS and an interplay between negative and positive charges in NMOS. Positive charge is slower to appear but eventually dominates. Depending on the affected oxide, the effects can be broadly categorized under two axes, **R**adiation **I**nduced **S**hort or **N**arrow **C**hannel **E**ffects (RINCE, RISCE), both becoming more prevalent with the scaling-down of device dimensions[1].

The RISCE[2] involves charges accumulated in the gate spacer oxides, overlapping the **L**ightly **D**oped **D**rain (LDD) extensions (Fig 1). In PMOS devices, the positive charge depletes the LDD of carriers, thus decreasing the device's current capability.

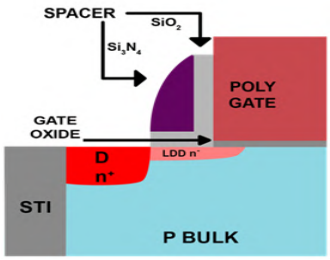

Fig.1 Side view (half) NMOS. Gate spacers, oxides and LDD extension responsible for RISCE shown

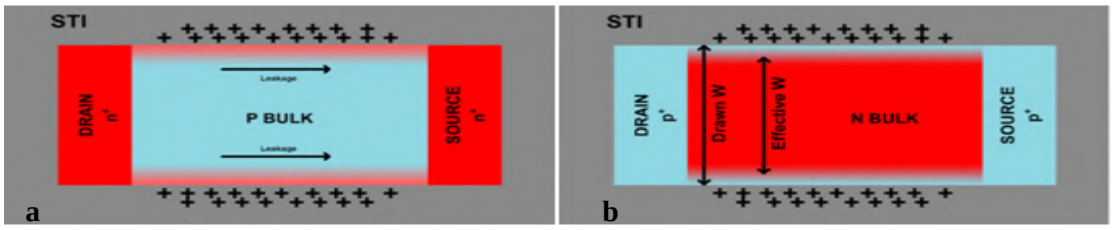

Fig.2 Top view NMOS (a), PMOS (b). STI oxides responsible for RINCE shown

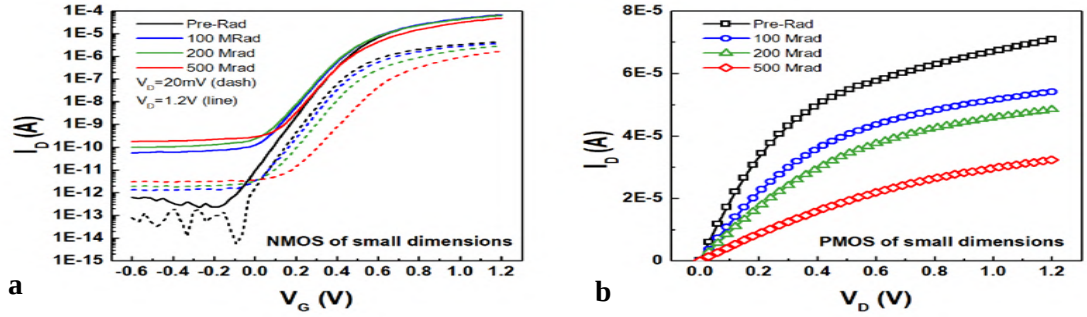

Fig.3 Degradation in NMOS transfer (a) and PMOS output (b) curves. Small geometries.

This can be macroscopically modelled as either a decrease in effective mobility[3] or as an increase in series resistance. In NMOS the positive charge destabilizes the effective LDD dopant concentration, which leads to pronounced **H**ot **C**arrier **I**njection (HCI) damage, that the LDD extensions were originally designed to mitigate. The slight inversion of the LDD caused by the positive charge is negligible due to the lower overall LDD conductivity with regards to the rest of the channel. In both cases (N- and P-MOSTs) $|V_{TH}|$ increase is recorded. Increasing temperature and bias exacerbate the effect.

The RINCE[4] involves charge accumulation in the sidewall **S**hallow **T**rench **I**solation (STI) oxides (Fig 2). NMOS devices develop parasitic side-channels (Fig.2a) leading to increased leakage currents. On the other hand, PMOS devices' channel sides become harder to invert, effectively decreasing the channel width, thus total current capability. At very narrow widths and high TID, N-devices never truly turn off and P-devices behave as high value resistors.

The above phenomena have been recorded and analysed in 65nm bulk CMOS devices and their dependence on device dimensions as well as temperature characterised[3,5]. In Fig.3 an overview of the devices' degradation with dose accumulation is given. In Fig.3a the V_{TH} shifts in NMOS can be observed, along with greatly increased leakage currents and decreased conduction currents. A strong TID-dependent **D**rain **I**nduced **B**arrier **L**owering (DIBL) effect is implied. In Fig.3b the pronounced decrease of PMOS current (attributed to both $|V_{TH}|$ increase as well as effective width decrease) is obvious. The loss of channel control (loss of defined triode-saturation transition, resistive behavior) can be seen at higher doses.

This work was partly financed under contracts PO CA6985699, CA7470539 from CERN, Geneva, Switzerland.

[1] G. Borghello, PhD thesis, cds.cern.ch/record/2680840
[2] F. Faccio et al., IEEE Trans Nucl Sci 65.1, 164–174, 2018, doi.org/10.1109/TNS.2017.2760629
[3] L. Chevas et al., IEEE MIXDES, Gdynia, 2018, doi.org/10.23919/MIXDES.2018.8436809
[4] F. Faccio et al., IEEE Trans Nucl Sci 52.6, 2933-2940, 2005, doi.org/10.1109/TNS.2005.860698
[5] L. Chevas, MSc thesis, doi.org/10.26233/heallink.tuc.89855

Role of stacking faults in defect introduction and radiation-enhanced dislocation glide in III-Nitride epilayers

G. P. Dimitrakopulos[1]*, J. Smalc-Koziorowska[2], I. Belabbas[3], I. Vasileiadis[1], J. Moneta[2], P. Chatzopoulou[1], and Ph. Komninou[1]

[1] Physics Department, Aristotle University of Thessaloniki, Thessaloniki, Greece

[2] Institute of High-Pressure Physics, Polish Academy of Sciences, Warsaw, Poland

[3] Chemistry Department, Abderahmane Mira University, Bejaia, Algeria

*gdim@auth.gr

III-nitride compound semiconductors offer a wide range of electronic and optoelectronic device applications including light emitters like LEDs and lasers, and high frequency, high-power transistors. However, the high density of dislocations (in the order of 10^8 - 10^{10} cm^{-2}) in their epilayers has a considerable impact on device properties such as degradation behavior and internal quantum efficiency. Classical mechanisms of threading dislocation (TD) introduction do not suffice to explain their high densities. We propose that the double positioning of adatoms during growth, which introduces intrinsic stacking faults (SFs), contributes significantly to the nucleation of TDs. Such phenomena usually take place close to the heteroepitaxial interface.

In particular, due to symmetry compensation, SF steps of height equal to an odd number of atomic layers acquire partial dislocation character. Then nucleation of TDs is geometrically necessary at the junctions of crystallographically equivalent steps, as proven by high resolution transmission electron microscopy observations (HRTEM) and shown in Fig. 1.[1] Furthermore, the overlapping of I_1-type intrinsic SFs is promoted by the elimination of the strain they induce along the growth direction. When the overlapping SFs are separated by an odd number of atomic layers their domains, again, are surrounded by sessile partial dislocations. Our concise crystallographic model explains the emanation of TDs from the facet junctions of such domains also as a geometrical necessity. All admissible configurations can be predicted *a priori* as was confirmed by the TEM/HRTEM observations.[2]

Regarding glissile partial dislocations delimiting I_2 intrinsic SFs, their motion under electron beam irradiation has been observed *in situ* by aberration-corrected HRTEM. Elucidating such phenomena is important for appreciating their influence on device degradation. We have observed that the stress-induced dissociation of screw lattice dislocations into two 30° Shockley partials can be reversed by the e-beam irradiation, causing reformation of the original dislocation and elimination of the SF.[3] This observation can be attributed to the phenomenon of Radiation Enhanced Dislocation Glide (REDG). In order to explain the phenomenon, the core structures of the partials were determined by DFT calculations. These core structures were then imaged directly by HRTEM under optimized imaging conditions determined through extensive image simulations. Sequentially-recorded HRTEM images were subjected to

geometrical phase analysis, and the mobile partial dislocation was identified to exhibit nitrogen-polarity core (Fig. 2). Based on the DFT calculations, the REDG effect was ascribed to the segregation of nitrogen vacancies at such dislocation cores. The elimination of SFs under minority carrier injection indicates that the REDG effect may have a less harmful impact on III-nitride devices compared to devices comprising other compound semiconductors.

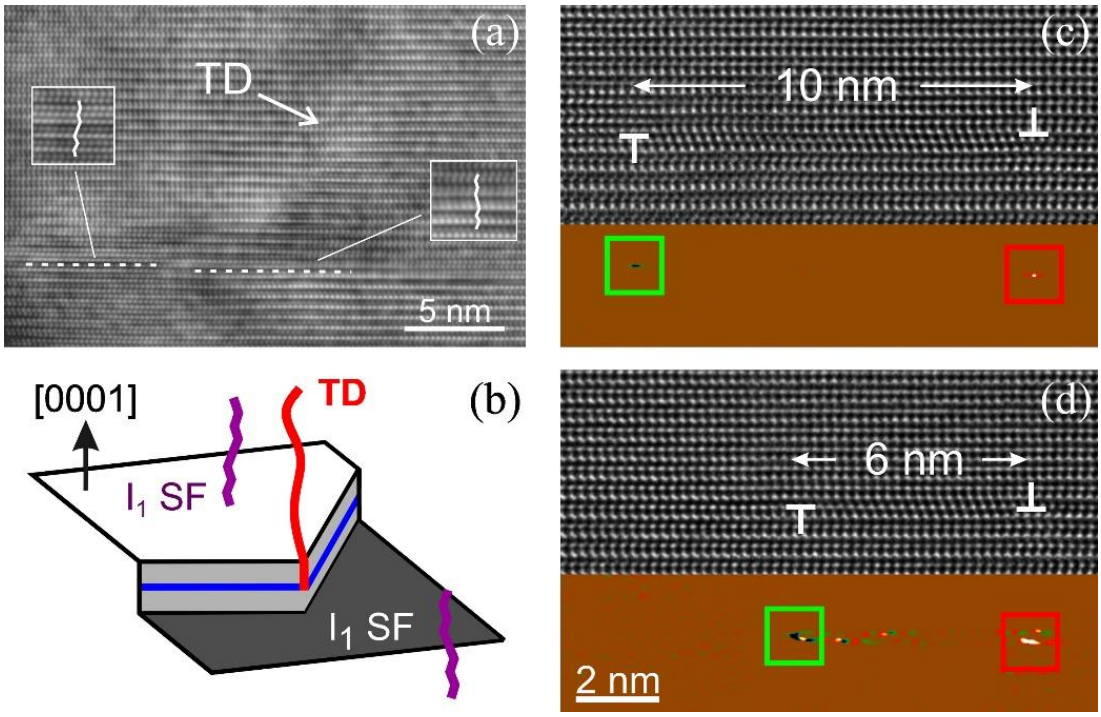

Fig. 1. (a) HRTEM image revealing a TD emanation from a region of a step formed by mirror related variants of I_1 SF. (b) Schematic illustration showing the emanation of a TD from the interaction of two crystallographically equivalent partial dislocations at SF steps. (c, d) Sequentially-recorded atomic-resolution images, with respective dislocation density tensor maps as insets, revealing the mobile nitrogen-polarity partial dislocation (green square) in the shrinking reaction.

Acknowledgements: Supported by project HARMONIA UMO-2016/22/M/ST5/00298. I.G.V. acknowledges support by the IKY project "Strengthening Human Resources Research Potential via Doctorate Research" (MIS-5000432). P.Ch./Ph.K./G.P.D. acknowledge support by project "INNOVATION-EL" (MIS-5002772).

[1] I. G. Vasileiadis, I. Belabbas, C. Bazioti, J. Smalc-Koziorowska, Ph. Komninou, and G. P. Dimitrakopulos, Physica Status Solidi B **258**, 2100190 (2021)
[2] J. Smalc-Koziorowska, J. Moneta, P. Chatzopoulou, I. G. Vasileiadis, C. Bazioti, O. Prytz, I. Belabbas, P. Komninou, G. P. Dimitrakopulos, Scientific Reports **10**, 17371, (2020)
[3] I. Belabbas, I. G. Vasileiadis, J. Moneta, J. Smalc-Koziorowska, and G. P. Dimitrakopulos, J. Appl. Phys. **126**, 165702 (2019)

ETHANOL EFFECT ON GRAPHENE DROP CASTING FOR ACETONE VAPOR SENSORS OPERATING AT ROOM TEMPERATURE

Michael Georgas, George Zardalidis, and Filippos Farmakis

Micro- and Nano-Technology Lab, Electrical Engineering and Computer Engineering dept., Democritus University of Thrace, Vas. Sofias 12, 67100, Xanthi, Greece.

mgeorgas@ee.duth.gr

Background

Acetone vapor sensors find great use in many areas as they are being used for non-invasive diabetes detection and monitoring [1], fat burning rate monitoring, general industrial applications or even detection of explosive environments [2]. Even though several sensors have been proposed, there is a continuous need for low power and low-cost ones, ideally implemented on flexible substrates. Thus, 2D nanomaterials such as graphene, due to their large specific surface area and exceptional electrical properties, have attracted broad attention for their gas sensing potential even at low temperature range of operation. As an example, recently, an acetone sensor was shown using graphene nanoplatelets combined with Zinc ferrite ($ZnFe_2O_4$) and achieved a sensitivity of 7% at 200 ppm acetone vapor while operating at 275°C [3].

Description of the Fabrication and Measurements

In this work, we compare various graphene-based gas sensors, capable of detecting acetone vapours, that are implemented on glass substrates and operate at room temperature. We demonstrate that such sensors exhibit good repeatability and sensitivity at 200 ppm of acetone vapour. All acetone sensing measurements were conducted by exposing the sensors in repeating cycles of several acetone concentrations diluted in nitrogen gas. To test the repeatability of the sensors, they were exposed to three cycles of 200 ppm acetone vapours followed by nitrogen gas during recovery. The sensors were tested in room temperature.

Experimental Results

It can be observed that the ethanol concentration has a clear effect on the final graphene deposition (Figure 1). In lower concentrations, 0% to 20%, the graphene sheet appears thicker than in higher concentrations, >30%. This effect is confirmed by optical transmittance measurements.

The best sensing performance was observed on the 10% and 20% batches. Graphene was more uniformly dispersed onto the glass, and the devices exhibited higher conductivity. When exposed in 200 ppm acetone these sensors exhibited a sensitivity ranging from 0.38% to 0.49%. For the pure DI water devices (0% ethanol) the deposition was comprised of multiple separated agglomerates and the sensitivity varied a lot between sensors of the same batch. For higher concentrations of ethanol, 30% and 70% devices did not provide operational sensors, while 40% and above demonstrated improved optical transmittance but had a vast range of

sensitivities, from failed devices up to 0.8%. The various sensors and their sensing performance is shown in Figure 2.

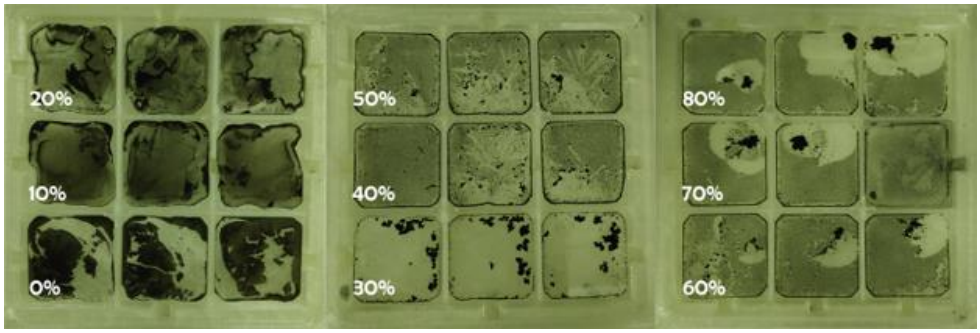

Figure 1. The graphene deposition for the various ethanol concentrations

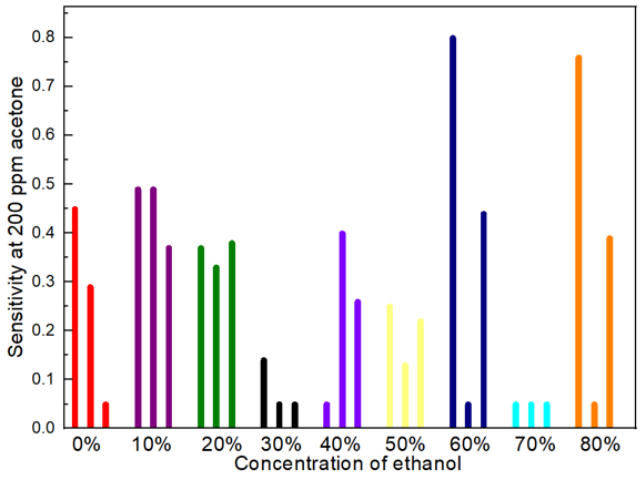

Figure 2. Sensitivity at 200 ppm acetone for 3 sample of each ethanol concentration batch. Failed sensors are depicted with 0.05% sensitivity and are devices that were either not electrically conductive or had no reaction to acetone.

References:

[1] Teng Xiao, Xiu-Yue Wang, Zhi-Hua Zhao, Liu Li, Lin Zhang, Hong-Chang Yao,Jian-She Wang, Zhong-Jun Li, College of Chemistry and Molecular Engineering, Zhengzhou University, Zhengzhou 450001, PR Chinaa, Sensors and Actuators B 199 (2014) 210–219

[2] López-Moreno, C., Palanco, S., Javier Laserna, J., DeLucia Jr, F., Miziolek, A. W., Rose, J.Whitehouse, A. I. (2006). J. Anal. At. Spectrom., 21(1), 55–60. doi:10.1039/b508055j

[3] Liu, F., Chu, X., Dong, Y., Zhang, W., Sun, W., & Shen, L. (2013). Sensors and Actuators B: Chemical,188,469–474. doi:10.1016/j.snb.2013.06.065

Acknowledgments

We acknowledge support of this work by the project “ASPiDA” (MIS 5047294) which is implemented under the Action “Support for Regional Excellence”, funded by the Operational Programme "Competitiveness, Entrepreneurship and Innovation" (NSRF 2014-2020) and co-financed by Greece and the European Union (European Regional Development Fund).

Electron Microscopy Characterization of InGaN/GaN Quantum Wells Grown onto GaN on Sapphire Templates

A. Gkanatsiou[1], Ch. B. Lioutas[1,*], E. Grzanka[2,3], M. Leszczynski[2,3]

[1]Department of Physics, Aristotle University of Thessaloniki,

GR-54124 Thessaloniki, Greece

[2]Institute of High Pressure Physics "Unipress", Polish Academy of Sciences

Sokolowska 29/37, 01-142 Warsaw, Poland

[3] TopGaN Ltd Sokolowska 29/37, 01-142 Warsaw, Poland

*lioutas@physics.auth.gr

InGaN is the key material in III-Nitride optoelectronic devices, such as light emitting diodes (LEDs) and laser diodes, operating in the blue and green ranges of the electromagnetic spectrum. Single and multiple quantum wells (MQWs) based on GaN/$In_xGa_{1-x}N$ serve as the active region in such devices, in which photons are generated by recombination of holes and electrons[1,2]. InGaN QWs are typically grown on GaN substrates (bulk or templates grown on sapphire). However, it is difficult to grown high-quality InGaN on GaN, because it shows a large lattice mismatch to GaN (11%)[3]. Moreover, another problematic issue is the low growth temperature needed for InGaN (700–800^{o}C) as compared to the higher (950–1050^{o}C) for GaN. Higher temperatures are also used for the overgrowth of the p-type layers on the QWs, resulting to the thermal instability of the QWs. These factors induce a number of crystallographic defects, such as non-uniform indium distribution (indium concentration fluctuations)[4] and a large concentration of point defects, deteriorating the optical properties of devices[1]. Hence, the growth of blue and green emitters still requires trade-offs between the p-type layer quality and the thermal stability of the QW[5].

In this work, InGaN/GaN QWs were grown onto GaN on sapphire templates. We investigated three MOVPE structures, labeled A, B, and C, respectively. Sample A, the as-grown sample, consists of two 10nm~ $In_{0.2}Ga_{0.8}N$ QWs/GaN barriers capped with a 20 nm GaN layer (see Fig. 1 for the nominal structure and thicknesses). This structure was overgrown on an $Al_{0.05}Ga_{0.95}N$ layer, with nominal thickness 20nm and a nominally undoped buffer GaN layer. To study the consecutive stages of thermal degradation, we have performed post-growth annealing experiments at temperatures of 800 (Sample B) and 900 °C (Sample C) in a protective atmosphere of ammonia and hydrogen for 30 minutes (in order to mimic the conditions expected during p-type layers growth of LED/laser structures). All QWs/barriers were grown under identical growth conditions and contain the same In content (almost 18%).

The structural quality of the samples was examined using Transmission Electron Microscopy (TEM) and Scanning TEM (STEM). The indium content of the $In_{0.2}Ga_{0.8}N$ layers was determined by TEM EDS (Energy-Dispersive X-ray Spectroscopy) analysis.

QB – GaN – 20nm
QW – InGaN – 10nm – 17.8%In
QB – GaN – 10nm
QW – InGaN – 10nm – 17.8%In
QB – GaN – 10nm
AlGaN – 20nm – 5% Al
GaN – 1,5mm
Sapphire

Fig. No 1. Sketch of the studied structure.

A series of TEM and STEM-images from the as-grown Sample (A), show that the MQWs exhibit a very good structural quality with sharp interfaces between the QWs and the GaN barriers. Moreover, the same situation is observed in Sample-B (annealed at 800^{o}C), where sharp interfaces with good quality epitaxial layers have also been captured.

However, in Sample-C, annealed at 900^{o}C, STEM studies show signs of thermal degradation. More specifically, STEM study reveals brighter regions of few nanometres (voids) in the first QW, located at the bottom of the QW/GaN interface, with lateral dimensions of ~8 nm. The preferential degradation of the first grown QW, with no subsequent QWs degrade can be explained by the proximity of the thick nominally undoped GaN layer, being a big reservoir of metal vacancies[5]. High-resolution images of such voids reveal their hexagonal shapes with edges aligned along $\{11\bar{2}0\}$ planes. The bright regions surrounding the voids, as observed in STEM images, are not related to a change in composition but to strain caused by the local deformation of the lattice.

ACKNOWLEDGMENTS

This research is co-financed by Greece and the European Union (European Social Fund- ESF) through the Operational Programme «Human Resources Development, Education and Lifelong Learning» in the context of the project “Reinforcement of Postdoctoral Researchers - 2nd Cycle” (MIS-5033021), implemented by the State Scholarships Foundation (IKY).

[1] M. Sarzyński, E. Grzanka, S. Grzanka, G. Targowski, R. Czernecki, A. Reszka, V. Holy, S. Nitta, Z. Liu, H. Amano, and M. Leszczyński, Materials (Basel). 12, 1 (2019).
[2] C.C. Chuo, C.M. Lee, and J.I. Chyi, Appl. Phys. Lett. 78, 314 (2001).
[3] M. Leszczynski, H. Teisseyre, T. Suski, I. Grzegory, M. Bockowski, J. Jun, S. Porowski, K. Pakula, J.M. Baranowski, C.T. Foxon, and T.S. Cheng, Appl. Phys. Lett. 69, 73 (1996).
[4] S. Nakamura, Science (80-.). 281, 956 (1998).
[5] J. Smalc-Koziorowska, E. Grzanka, A. Lachowski, R. Hrytsak, M. Grabowski, S. Grzanka, S. Kret, R. Czernecki, H. Turski, L. Marona, T. Markurt, T. Schulz, M. Albrecht, and M. Leszczynski, ACS Appl. Mater. Interfaces 13, 7476 (2021).

Carbyne films on nanostructured surfaces: A new class of hard carbon materials for sensing and antibacterial action

D. Ioannou[1,2], D. Nioras[1,3], D. Kefallinou[1,3], G. Tasios[1,3], D. Papadopoulou[1,3], A. Lukin[4], A. Brigadin[5], A. Tserepi[1], Evangelos Gogolides[*1]

[1]Institute of Nanoscience and Nanotechnology, NCSR "Demokritos" Aghia Paraskevi, Greece 15231

[2]School of Mechanical Engineering, National Technical University of Athens, Zografou, 15780, Attica, Greece

[3]Physics Department, National Technical University of Athens, Zografou Campus, Athens, Greece 15780

[4]Western-Caucasus Research Center Bldg. 9, Tupik Zvezdniy, Tuapse, Krasnodar Territory, RU 352808

[5]Swissimpianti Sagl, 6828 Balerna, Switzerland

e.gogolides@inn.demokritos.gr

Following the science and engineering revolution of Graphene (Nobel prize in 2010) several new two-dimensional materials have emerged, and their use is expected to have high impact in our daily life in the near future. Their palette of functionalities ranges from mainstream microelectronics to antibacterial micro-fluidic devices. In this work we focus on the allotropes of carbon called Carbyne, which contain alternating single and triple carbon bonds, including linear molecules such as polyene (alternating single and triple bonds i.e. acetylenic carbon), and cumulene (consecutive double bonds). Carbynes are reported to have a huge Young modulus of 32.7 TPa, which is 40X that of diamond [1]. Carbynes are thus emerging as a new class of very strong, very tough, and very light material that could be the next big thing in carbon-based material science, fabrics, sensors, electronics and many more fields.

We aim to investigate the antibacterial properties of micro and nano-structured polymeric surfaces that we develop using our dry plasma technology [2] after they have been deposited with Carbyne. These polymeric surfaces include: Poly(methyl methacrylate) (PMMA), Polyether ether ketone (PEEK) and Cyclo olefin polymer (COP) and we create micro and nano-structures on their surfaces by means of oxygen plasma (figure 1a). The next step includes the deposition of a thin Carbyne film, approximately 30-40 nm thick (figure 1c). Additionally we have managed to manipulate the wetting properties of these Carbyne coated surfaces by altering the conditions of plasma processing. Indeed 5 minutes of O_2 plasma can result in hydrophilic (contact angle 30-40 °) or hydrophobic (contact angle 110 °) surfaces. The antibacterial properties of our plasma treated surfaces have already been reported [3] against E.Coli with bactericidal efficacy 100%. Thus we envision a new class of bacteria detection devices [4] which will be designed based on nanowire coated microfluidics

containing coated carbyne films, one of the hardest materials on Earth. This will be extremely important for public health, safety, early prognosis and prevention of outbreaks.

This work has been funded by the T12EPA5-00067 Project ‘Carbyne Films: Synthesis of a New Class of Carbon Allotrope and Novel Applications in Sensors and Biosensors (CarbyneSense). We thank N. Papanikolaou and Sp. Gardeli for their help with various experiments.

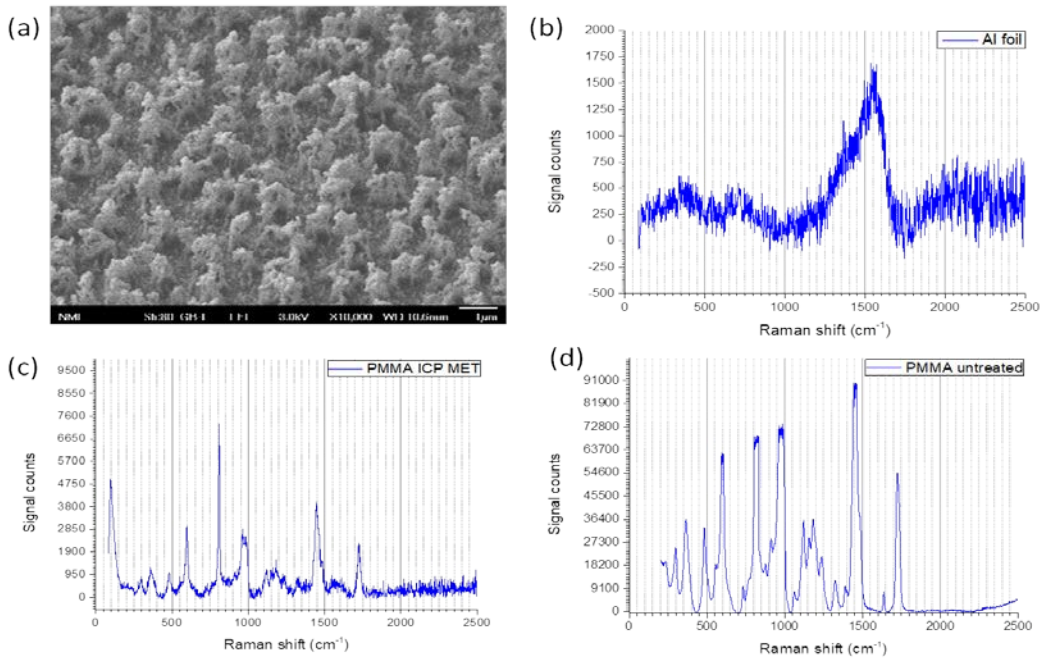

Fig 1 (a) SEM image of PMMA surface nanotextured for 5 minutes in O_2 plasma, (b) Raman spectrum of Carbyne film deposited on Aluminum foil, (c) Raman spectrum of plasma nanotextured PMMA surface featuring Carbyne film and (d) Raman spectrum of untreated PMMA surface for reference.

[1] S. S. Sohn and J. W. Bode, “N-heterocyclic carbene catalyzed C-C bond cleavage in redox esterifications of chiral formylcyclopropanes,” *Angew. Chemie - Int. Ed.*, vol. 45, no. 36, pp. 6021–6024, 2006.

[2] K. Tsougeni *et al.*, “Mechanisms of Oxygen Plasma Nanotexturing of Organic Polymer Surfaces : From Stable Super Hydrophilic to Super Hydrophobic Surfaces,” vol. 25, no. 19, pp. 11748–11759, 2009.

[3] P. Dimitrakellis, K. Ellinas, G. D. Kaprou, D. C. Mastellos, A. Tserepi, and E. Gogolides, “Bactericidal Action of Smooth and Plasma Micro-Nanotextured Polymeric Surfaces with Varying Wettability, Enhanced by Incorporation of a Biocidal Agent,” *Macromol. Mater. Eng.*, vol. n/a, no. n/a, p. 2000694, Feb. 2021.

[4] G. Papadakis *et al.*, “Micro-nano-bio acoustic system for the detection of foodborne pathogens in real samples,” *Biosens. Bioelectron.*, vol. 111, pp. 52–58, 2018.

Ευρωπαϊκή Ένωση
ΕΠΑνΕΚ 2014-2020 ΕΠΙΧΕΙΡΗΣΙΑΚΟ ΠΡΟΓΡΑΜΜΑ ΑΝΤΑΓΩΝΙΣΤΙΚΟΤΗΤΑ ΕΠΙΧΕΙΡΗΜΑΤΙΚΟΤΗΤΑ ΚΑΙΝΟΤΟΜΙΑ
ΕΛΛΗΝΙΚΗ ΔΗΜΟΚΡΑΤΙΑ ΥΠΟΥΡΓΕΙΟ ΑΝΑΠΤΥΞΗΣ ΚΑΙ ΕΠΕΝΔΥΣΕΩΝ
ΓΓΕΤ ΓΕΝΙΚΗ ΓΡΑΜΜΑΤΕΙΑ ΕΡΕΥΝΑΣ ΚΑΙ ΤΕΧΝΟΛΟΓΙΑΣ
ΕΣΠΑ 2014-2020
Με τη συγχρηματοδότηση της Ελλάδας και της Ευρωπαϊκής Ένωσης

Strain Engineering in 2D material based transistors

J. Parthenios[1,*]

[1]Institute of Chemical Engineering Sciences, Foundation for Research and Technology Hellas (FORTH-ICEHT), Patras, Greece

*jparthen@iceht.forth.gr

Semiconducting two-dimensional Transition Metal Dichalcogenides (2D - TMDCs) can sustain very large deformations before failure (up to 8%) while presenting large (1.5 to 2.0 eV) and extremely strain-sensitive (50-130 meV/%) direct bandgaps. Thus, this class of materials holds great promise in strain engineering applications. Over the decade, in the bulk of the published works, 2D – TMDC crystals have been tested under various types of strain[1,2]. However, with respect to flexible electronics, where a large number of interfaces is involved, the extent to which mechanical strains can be efficiently transferred to the 2D crystal requires further attention.

In this work it is shown that despite the larger number of interfaces occurring in a 2D material transistor, biaxial strain can be efficiently imposed on the devices in a controllable manner. In particular, WSe_2 and MoS_2 field effect transistors, fabricated on flexible polyethylene napthalate (PEN) substrates are subjected to biaxial strain. The efficient strain transfer is verified using in-situ Raman mapping over the whole channel of several devices. Additionally, it is shown that in the spectroscopically difficult case of WSe_2, where the strain sensitive E' mode is accidentally degenerate with the more intense and strain insensitive A' mode, the second order Raman active modes around 350 - 400 cm^{-1} can be used as efficient strain indicators.

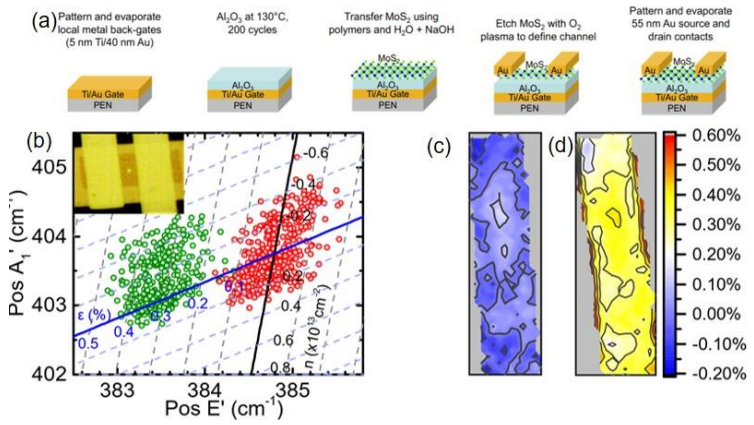

Fig. 1 (a) The 2D material device fabrication steps, (b) Optical microscope image of the strained device and (c), (d) mechanical strain maps on the transistor channel at zero and 0.5% applied biaxial strains, respectively (channel width = 10 μm).

[1]A. Michail, D. Anestopoulos, N. Delikoukos, J. Parthenios, S. Grammatikopoulos, S. A. Tsirkas, N. N. Lathiotakis, O. Frank, K. Filintoglou and K. Papagelis, 2D Materials 8, 015023 (2020).
[2]D. Lloyd, X. Liu, J. W. Christopher, L. Cantley, A. Wadehra, B. L. Kim, B.B. Goldberg, A. K. Swan and J. S. Bunch Nano Letters 16, 5836–41(2016).

Flexible graphene field effect transistors as strain sensors

Georgios A. Katirtsidis[1,*], Filippos Farmakis[2]

[1]Democritus University of Thrace, Micro and Nano-Technology Laboratory, Department of Electrical and Computer Engineering, Xanthi, Greece

*alexkatir@gmail.com, farmakis@ee.duth.gr

Recently, graphene field-effect transistors (GFETs) on various flexible substrates, such as polyethylene (PET[1]), polyethylene naphthalate (PEN[2]) and polyimide (Kapton[3,4]), have been reported. Although it has been shown, through bending tests during DC and RF characterization, that these GFETs were sensitive to strain, **there are no reports of testing the GFETs' behaviour both when increasing and decreasing the bending radius**. In this work, we developed bottom gated GFETs fabricated on Kapton substrate and studied their electrical behaviour for decreasing and then successively increasing bending radius. It was shown that $\mathbf{I_{OFF}}$, which is the minimum drain current at the Dirac point, can be used to detect different strain percentages and hence giving rise to our hopes that our devices can be potentially work as strain sensors.

A schematic of our device is shown in Fig. 1 (a). As flexible substrate, a 75 μm thick Kapton film was used so as to be compatible with the graphene transfer process temperature. Then, in order to reduce Kapton's surface roughness, we deposited SiN_x (~250 nm) and aluminum (~150 nm) on top, for the bottom gate metal, via DC magnetron reactive sputtering. As gate dielectric, a SiN_x (~200 nm) thin film was grown via DC magnetron reactive sputtering. The monolayer graphene that we used was the Graphenea's "Easy Transfer: Monolayer Graphene on Polymer Film". We annealed our samples at 300 °C in N_2 atmosphere for 2.5 hours in order to reduce the residues of the sacrificial layer that supported graphene during the transfer. Following the graphene transfer, for the source and drain pads, we deposited aluminum (~150 nm) via thermal evaporation. The patterning of the contact pads took place at the step of thermal evaporation where a mechanical mask was placed right on top off the samples prior to the aluminum deposition. The resulting length and width of the graphene channels were 600 μm and 900 μm respectively. Finally, the samples were annealed again at 150 °C for 1.5 hours in a glove box with Argon atmosphere and ultra-low humidity levels.

Fig. 1 (b) and (c) exhibits the drain current I_{DS} versus the gate voltage V_{GS} characteristics at drain voltage V_{DS}= 2 V for decreasing bending radius from ∞ mm (no bending) down to 8 mm and for increasing bending radius from 8 mm up to 14.78 mm respectively. It has to be noted that the monolayer graphene that we used is intrinsically n doped and the regions below the contact pads are heavily n doped due to the use of aluminum. For decreasing bending radius in Fig. 1 (b), the graphene in the channel region is getting less and less n doped. The same applies for the graphene below the contact pads, with the only difference being that the effect of bending is more pronounced. Therefore, as the bending radius decreases the total resistance between source and drain pads decreases as well and thus the minimum drain current at the Dirac point I_{OFF} increases from 3.73 μA up to 3.83 μA. Furthermore, the more intense effect of bending in the electron conduction region, is attributed to the different change rate of the doping state (towards less n doped graphene) between the graphene in the contacts' and the channel regions. In addition, the slight shift of Dirac point V_{Dirac} towards lower gate voltages, is attributed to the increase of the electron current. For

increasing bending radius (Fig. 1 (c)), the effect of bending on our device becomes less and less severe for the graphene-metal contact regions but not for the graphene channel region. It is suggested that this behaviour can be explained by the permanent deformation of the Kapton substrate. Thus, for increasing bending radius, the different change rate of the doping state (towards higher electron concetration of the graphene) between the graphene in the contact regions and the channel region results in a larger total resistance between source and drain, and consequently the off current I_{OFF} decreases from 3.83 μA down to 3.7 μA. In addition, due to the fact that the graphene channel region is not so sensitive to strain, the effect of the decrement of the bending radius is more intense in the hole conduction region where the resistance is generally larger than the one in the electron conduction region. As a result, the maximum drain current in the hole conduction region decreases and the V_{Dirac} shift, is attributed to the decrease of the hole current similarly to the case for decreasing bending radius.

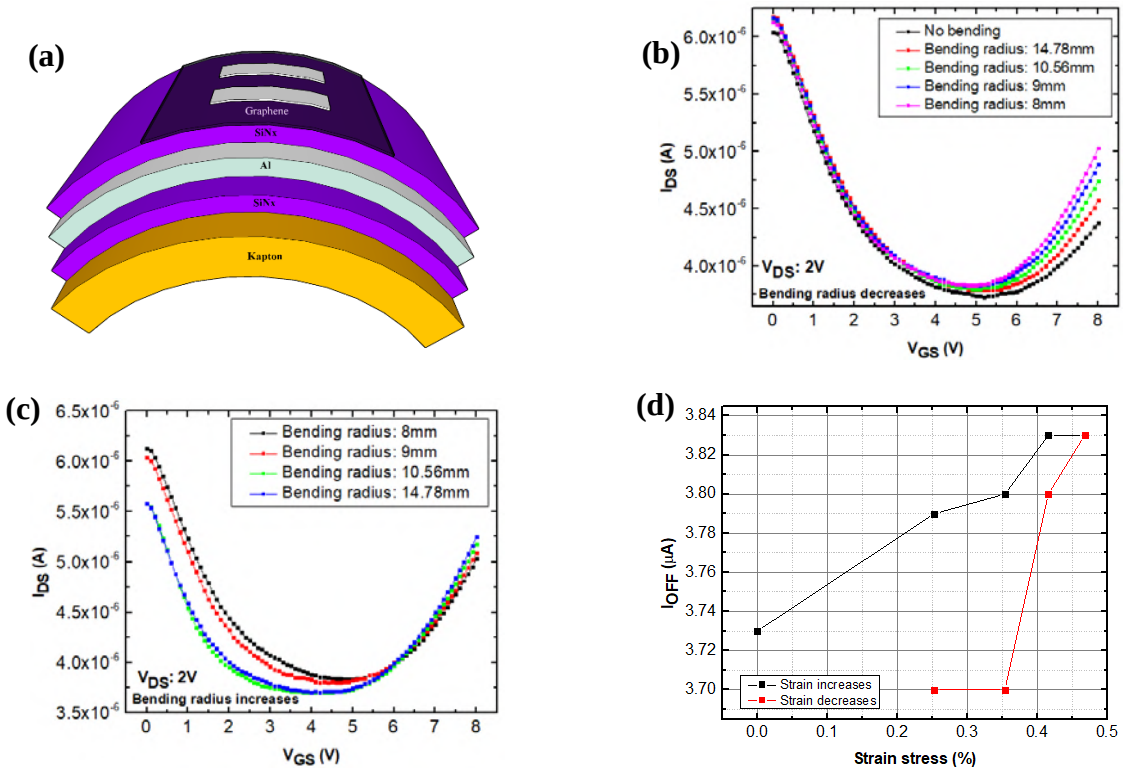

Fig. 1: (a) Schematic of the prepared devices (not to scale), (b) and (c) are the drain current I_{DS} versus the gate voltage V_{GS} characteristics at drain voltage V_{DS}= 2 V for decreasing bending radius from ∞ mm down to 8 mm and increasing bending radius from 8 mm up to 14.78 mm respectively and (d) the minimum drain current I_{OFF} versus the strain percentage.

1. Lan Y, Xu Y, Wu Y, et al. Flexible graphene field-effect transistors with extrinsic fmax of 28 GHz. *IEEE Electron Device Lett.* 2018;39(12):1944-1947. doi:10.1109/LED.2018.2876010

2. Petrone N, Meric I, Hone J, Shepard KL. Graphene field-effect transistors with gigahertz-frequency power gain on flexible substrates. *Nano Lett*. 2013;13(1):121-125. doi:10.1021/nl303666m

3. Kim K, Park S, Kim O. Comprehensive analysis of the effects of bending strain on GFET on ultra-flat flexible PI substrate using varnish PI. *Micro Nano Lett*. 2019;14(3):249-253. doi:10.1049/mnl.2018.5448

4. Wei W, Pallecchi E, Haque S, et al. Mechanically robust 39 GHz cut-off frequency graphene field effect transistors on flexible substrates. *Nanoscale*. 2016;8(29):14097-14103. doi:10.1039/c6nr01521b

Status and perspective of alternative manufacturing methods for nano-enabled components and surfaces.

Nikos Kehagias

NCSR “Demokritos",

Institute of Nanoscience and Nanotechnology,

P. Grigoriou 27 & Neapoleos Str., 15341 Ag. Paraskevi, Greece

*n.kehagias@inn.demokritos.gr

Developing novel alternative nanomanufacturing methods which conform with the needs and requirements of industry, is of great importance. The prerequisite for personalised, light-weight, thin and sustainable components and products has emerged the need for fabrication paths which meet low-cost and high-throughput constrains. In this perspective nanoscale patterning of large area surfaces with tailored functionality is of high demand, addressing different market trends and applications.

In this talk we will overview the current requirements and fabrication methods used to realise nano scale photonic components and smart surfaces and project these demands to the future needs. Moreover, we will discuss how we exploit conventional and non-conventional lithography approaches to meet the rising demand for nanopatterning of complex shape surfaces.

Advanced inline nano-metrology techniques for roll to roll nanoimprint lithography manufacturing processes

N. Kehagias[1]*, E. Svinterikos[2], K. Tourlouki[2], T. Tachtsidis[2], C. Katsogridakis[1], V. Constantoudis[1], N. Papanikolaou[1], D. Goustouridis[3], I. Raptis[1], P. Argitis[1]

1. NCSR Demokritos, Institute of Nanoscience and Nanotechnology, P. Grigoriou 27 & Neapoleos Str., 15341 Ag. Paraskevi, Greece

2. Nanotypos, ICT Business Park, Technopoli Thessaloniki, 55535 Pylea, Greece

3. ThetaMetrisis, Christou Lada 40, Athens, 12132, Greece

*n.kehagias@inn.demokritos.gr

The role of functional films that are coated with continuous manufacturing processes (exp. Roll-2-Roll Nano Imprint Lithography) has been growing rapidly in recent years, a trend that is expected to intensify in the short to medium term. In this area, precise control of dimensional structures and objects is a key issue with an important role in the cost of production and the properties of the finished product. Thus, there is an increasing need for a fast, non-invasive method of performing in-situ and real-time monitoring of chemical changes and metrology of the coatings that are essential elements for quality control of processes and optimization of the production process.

The aim of NanoMet project is to develop a dimensional metrological system that will be non-destructive, cost-effective and capable of recording data in real time. The metrology system will be based on optical non-destructive measurements that will provide real-time information on the critical dimensions and the evolution of the characteristics of the manufactured nanostructured materials. In particular, information on the thickness of the depositing and stamping material as well as the dimensions of the printed structures will be measured in real time. An important element for all the above measurements and for the evaluation of the metrology method is the control of the polymeric imprinting material. For that reason, polymeric materials with certain optical and chemical properties will be designed and developed and will create a database of features that will help in the comprehensive understanding and evaluation of the dimensional metrology platform. In this paper will present the developments performed within the NanoMet project and discuss the metrological and material challenges needed to achieve our objectives.

Acknowledgments:

This work has been funded under the national research programme of General Secretariat for Research and Innovation, Project acronym: NanoMet, Project grant number: Т6УВП-00253.

A chaos-based approach to the characterization of the complexity of micro- and nanostructured surfaces

A. Kondi[a,b,*] , V. Constantoudis[a,d], P. Sarkiris[a] , K. Ellinas[c] and E. Gogolides[a,d]

[a]Institute of Nanoscience and Nanotechnology, N.C.S.R. Demokritos, Agia Paraskevi, 15310, Greece

[b]Department of Physics, School of Science, University of Athens, 15784 Athens, Greece

[c]Department of Food Science and nutrition, School of the Environment, University of the Aegean, 81400 Myrina, Greece

[d]Nanometrisis p.c., Agia Paraskevi, 15341, Greece

*alkondi@phys.uoa.gr

Abstract: In many areas of research and industry, the use of materials having rough surfaces made up of micro- and nanostructures is crucial[1,2]. The morphology of these micro- and nano-structured surfaces is usually complex challenging the conventional mathematical tools used for their quantitative characterization and evaluation[4]. The main aim of this work is to propose an alternative approach and characterize the spatial complexity of micro and nanostructured surfaces by applying models from nonlinear discrete dynamical systems (maps) which exhibit strong chaotic behavior. In particular, we characterize the complexity of microscope images of rough surfaces using the fundamental components of chaotic dynamics, i.e. the stretching and folding of phase space points. The key concept is to follow the alterations of an image during the first iterations of a chaotic discrete dynamical system, such as the Arnold cat map[3]. The use of the map results in an enhancement of the high frequency content of images coupled with an increase of image discontinuities since the primary effects of the Arnold map are the stretching and folding of the pixels (phase space points). Since the first effect (the enhancement of high frequencies) can be used to quantify the distance of texture from randomness and noise and the second effect (the proliferation of discontinuities) can be used to quantify the distance from order and homogeneity, we exploit these effects to quantify the complexity of S-type[5] (lying between homogeneity and randomness) of the image texture. The method is validated in synthetic images produced from computer-generated surfaces with regulated correlation length and fractal dimension and is then applied to real images of nanostructured polymer and metal surfaces obtained from a Scanning Electron Microscope with highly intriguing results.

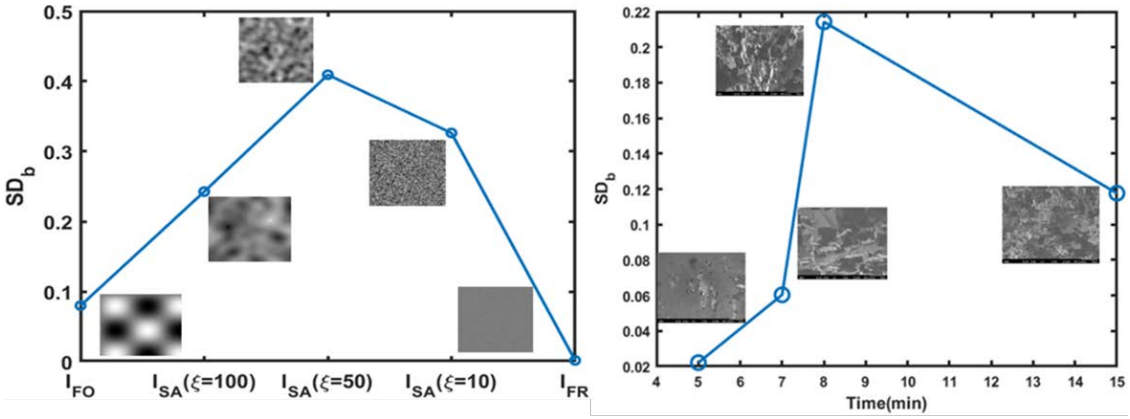

(a) **(b)**

Fig. 1 a) The value of SD_b (y-axis) quantifying the chaos-based complexity of the simulated surfaces shown in the insets going from full order (I_{FO}) to full noise (I_{FR}), with I_{FO} being the 2D sinusoidal surface and I_{SA} being the self-affine rough surfaces with correlation lengths ξ= 100, 50 and 5 pixels and roughness exponent α= 1 respectively. One can notice the maximum of complexity in the middle correlation lengths lying between the extremes of full order and full noise, b) SD_b versus etching time for the SEM images of experimental surfaces of Al film during its wet etching with HCl

This work has been funded by the T12EPA5-00067 Project 'Carbyne Films: Synthesis of a New Class of Carbon Allotrope and Novel Applications in Sensors and Biosensors (CarbyneSense)'

Ευρωπαϊκή Ένωση
ΕΠΑνΕΚ 2014-2020 ΕΠΙΧΕΙΡΗΣΙΑΚΟ ΠΡΟΓΡΑΜΜΑ ΑΝΤΑΓΩΝΙΣΤΙΚΟΤΗΤΑ ΕΠΙΧΕΙΡΗΜΑΤΙΚΟΤΗΤΑ ΚΑΙΝΟΤΟΜΙΑ
ΕΛΛΗΝΙΚΗ ΔΗΜΟΚΡΑΤΙΑ ΥΠΟΥΡΓΕΙΟ ΑΝΑΠΤΥΞΗΣ ΚΑΙ ΕΠΕΝΔΥΣΕΩΝ
ΓΓΕΤ ΓΕΝΙΚΗ ΓΡΑΜΜΑΤΕΙΑ ΕΡΕΥΝΑΣ ΚΑΙ ΤΕΧΝΟΛΟΓΙΑΣ
ΕΣΠΑ 2014-2020
Με τη συγχρηματοδότηση της Ελλάδας και της Ευρωπαϊκής Ένωσης

References

1. Y. Zhao, G.C. Wang, T.M. Lu, Characterization of Amorphous and Crystalline Rough Surface: Principles and Applications, first ed., San Diego, CA: Academic Press, 2001
2. Almqvist, On the Effects of Surface Roughness in Lubrication, LAP Lambert Academic Publishing, 2009
3. Dyson, Freeman J., and Harold Falk. "Period of a Discrete Cat Mapping." The American Mathematical Monthly, vol. 99, no. 7, Mathematical Association of America, (1992), pp. 603–14, https://doi.org/10.2307/2324989
4. Arapis, V. Constantoudis, D. Kontziampasis, A. Milionis, C.W.E. Lam, A. Tripathy, D. Poulikakos, E. Gogolides, Measuring the complexity of micro and nanostructured surfaces, Materials Today: Proceedings, (2022), https://doi.org/10.1016/j.matpr.2021.10.120.
5. R. Alamino, Measuring Complexity through Average Symmetry, Journal of Physics A: Mathematical and Theoretical, Volume 48, Number 27, (2015), https://doi.org/10.1088/1751-8113/48/27/275101

Linking surface roughness to functionality parameters: A machine learning approach based on symbolic regression

A. Kondi[a,b,*], A. Stellas[c], V. Constantoudis[a,c]

[a]Institute of Nanoscience and Nanotechnology, N.C.S.R. Demokritos, Agia Paraskevi, 15310, Greece

[b]Department of Physics, School of Science, University of Athens, 15784 Athens, Greece

[c]Nanometrisis p.c., Agia Paraskevi, 15341, Greece

*alkondi@phys.uoa.gr

Abstract: One of the key features of modern technology is the extensive use of heterogeneous materials due to the wide range of multiple properties they have in imitation of many similar materials in nature. The majority of heterogeneous materials on micro- and nanoscale often exhibit randomness in their surface morphology which can take various diverse appearances and usually is called surface roughness [1]. The surface roughness, though extremely critical in determining the properties and functionality of materials, is one of the main obstacles against our efforts to understand the link of the material processing with the structure and then with their properties (Process-Structure-Property relationship).

In this work we focus on the Structure-Property relationship. More specifically, we consider the functional parameter of the active surface area (S_a) which affects multiple physicochemical properties of surfaces. Concerning structure, we take into account the main parameters characterizing the surface roughness of nanostructured materials, i.e. rms(r), skewness(s), kurtosis(k), correlation lengths(ξ) and roughness exponent(α) since it is very critical to link them with the property parameter S_a. Previous works have already been conducted [2] to link the roughness ratio r ($\frac{\text{active surface area}}{\text{projected surface area}}$) with the aforementioned parameter S_a, by using Artificial Neural Networks. However, a closed formula connecting structural with functional parameters is still missing. In this work, we aim to predict such closed formula using Symbolic Regression (SR), one of the recent machine learning techniques, that is gaining popularity as a potent grey-box strategy for identifying functional forms from input data [3]. Symbolic regression identifies a symbolic expression that corresponds to data from an unidentified function. In other words, it is a tool that can determine the underlying mathematical formula that best captures the relationship between a number of variables. To forecast the targets of the dependent variables, it constructs a series of random formulas to describe the link between known independent variables. Then, by choosing the fittest individuals from the data (population) to undertake further genetic operations, each succeeding generation of programs transforms from the one that came before it.

The developed SR model is trained with a large set of synthetic rough surfaces (both Gaussian and non-Gaussian) generated using an algorithm based on the stochastic inverse Fourier Transform[1,2]. Each individual surface is characterized by the five aforementioned roughness

parameters (rms, skewness, kurtosis, correlation length, roughness exponent) while the functional parameter of active surface area S_a is also estimated using well designed algorithms thus generate a sufficiently big dataset of parameters. We will then use this dataset in order to train a symbolic regression model to predict the underlying relationship of those parameters in a closed form. A schematic of the methodology can be seen in Figure 1.

Since SR analysis framework has been developed, the methodology will be applied in the SEM images of the rough surfaces of novel carbyne films to aid the understanding of their structure-property relationship and their applications in biosensors and radical chemical sensors.

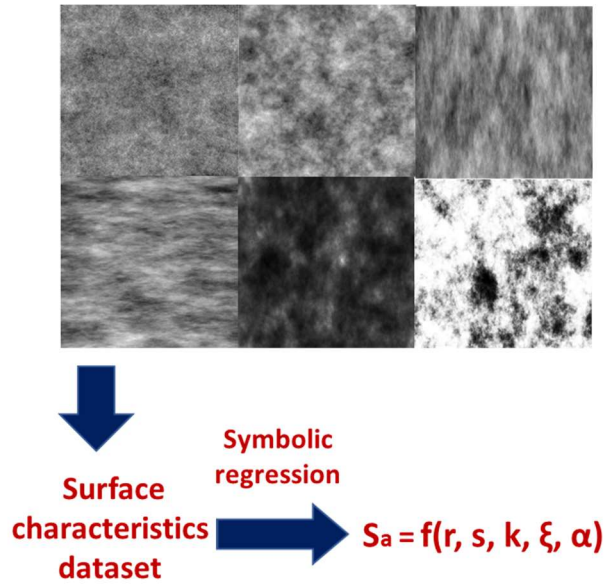

Fig. 1. Rough surfaces generated with combinations of the rms(r), skewness(s), kurtosis(k), correlation lengths(ξ), roughness exponent(α) and active surface area(S_a) from which we will calculate the aforementioned parameters and create the dataset of training data of our SR model

This work has been funded by the T12EPA5-00067 Project 'Carbyne Films: Synthesis of a New Class of Carbon Allotrope and Novel Applications in Sensors and Biosensors (CarbyneSense)'

Με τη συγχρηματοδότηση της Ελλάδας και της Ευρωπαϊκής Ένωσης

References

1. Y. Zhao, G.C. Wang, T.M. Lu, Characterization of Amorphous and Crystalline Rough Surface: Principles and Applications, first ed., San Diego, CA: Academic Press, 2001
2. A. Stellas, G. Giannakopoulos, V. Constantoudis. "Hybridizing AI and Domain Knowledge in Nanotechnology: the Example of Surface Roughness Effects on Wetting Behavior." *SETN Workshops* (2020), https://dblp.org/rec/conf/setn/2020w
3. Y. Wang, N. Wagner, J. Rondinelli, Symbolic regression in materials science. MRS Communications, 9(3), 793-805. (2019), https://doi.org/10.1557/mrc.2019.140

Nanoelectronics pilot line in Greece: Myth or reality?

George Konstantinidis[1,2*], Loukas Michalas[1,2], Nikos Papadakis[1,2], Michalis Sfendourakis[1,2], Antonis Stavrinidis[1,2], George Stavrinidis[1,2], Thanasis Kostopoulos[1,2], Valia Kontomitrou[1,2], George Deligeorgis[1,2], Manolis Verikokidis[1,2], Manos Trichas[1,2], Alexandros Georgakilas[2,1], Maria Kayambaki[1,2], Katerina Tsagaraki[1,2], Nikos Makris [1,4], Adam Adikimenakis[1,2], Afshin Ziaei[5] and Spiros Anastasiadis[1,3]

[1]Institute of Electronic Structure and Laser, Foundation for Research and Technology – Hellas, Heraklion, Crete, Greece

[2]Department of Physics, University of Crete, Heraklion, Greece

[3]Department of Chemistry, University of Crete, Heraklion, Greece

[4]Technical University of Crete, School of Electrical & Computer Engineering, Chania, Greece

[5]Thales Research and Technology France, 91767 Palaiseau, France

aek@physics.uoc.gr

III nitride materials (AlN, GaN, InN, and their solid solutions) possess a unique combination of physical properties that guarantee demand for them in modern microelectronics and optoelectronics[1]. The Microelectronics Research Group (MRG)[2] of the Institute of Electronic Structure and Laser (IESL) of the Foundation for Research and Technology – Hellas (FORTH) has been intensely active in III-nitrides related research since 1996. Through this journey it has developed expertise in material epitaxial growth (by plasma assisted Molecular beam epitaxy RF-MBE), design, fabrication and assessment of nanoelectronics devices and integrated circuits, nanophotonic components as well as sensors. This effort has been supported financially by national but primarily European competitive funds. Through this "European path" a significant network of international collaborators was established with the French global industrial company Thales SA standing out. This strong partnership that started in 2009 laid down a roadmap for the development of a new generation of reconfigurable transceivers (TRXs) for future communication and radar applications. The technological platform envisaged entailed III-nitride based monolithic microwave circuits (MMICs) and radio frequency microelectromechanical switches (RF MEMS) with the final aim to integrate them all monolithically thus achieving not only beyond state-of-the-art performance but also with drastic size, weight and power (SWaP) advances. Figure 1 depicts the chronological progression of the technology and the supporting funding.

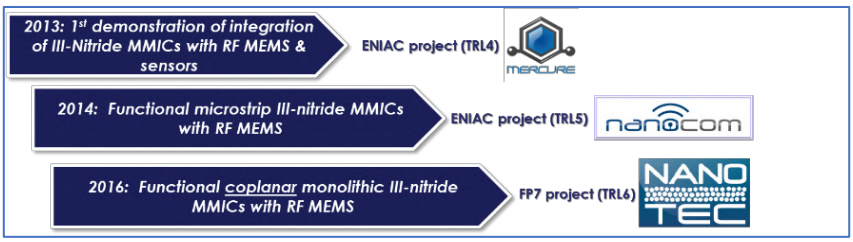

Figure 1: Temporal evolution of TRX technology and related funding

[1] https://doi.org/10.1016/B978-0-08-102096-8.00012-4

[2] https://www.iesl.forth.gr/en/research/research-divisions/materials-and-devices-division

Further post NANOTEC bilateral technological developments between THALES and MRG, forged the idea to seek additional backing for a pilot line at FORTH through the Fast Track to Innovation (FTI) funding instrument of the European Union to develop the First Commercially available high-power X-band miniaturised TRX based on monolithic integration of power RF MEMS and power GaN MMICs. The consortium to undertake the task comprises, in addition to THALES (RF MEMS) and FORTH (GaN MMICS), of 3 SMEs (RF Microtech from Italy, CIDETE from Spain and TAIPRO engineering from Belgium) that were selected very carefully based on their expertise (RF system design, Cooling for nanoelectronics and packaging respectively) in order to allow for the final SMARTEC packaged TRX module. The *Pilot line production of transceiver modules for the next generation of smart RF power applications* (SMARTEC) project started in September 2019[3]. The project entails from the creation of a new clean room (Figure 2) to the purchase of new scientific tools (Figure 3), from ISO quality system certification to elaborate business plans (Figure 4), from developing a process design kit (PDK) to advances in MMICs, RF MEMS packaging and cooling concepts (Figure 5).

Figure 2: SMARTEC clean room (from design to implementation)

Figure 3: New or upgraded scientific tools (Sputtering, PECVD, ICP, RF station)

Figure 4: ISO 9001 quality certificate, process validation, business planning

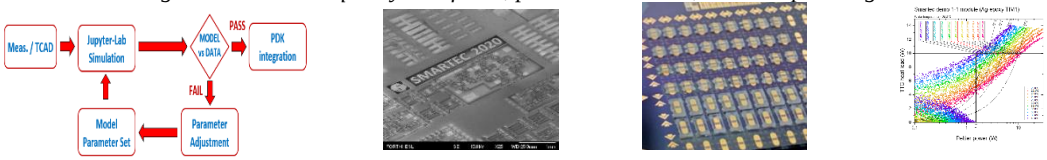

Figure 5: Design, fabrication, packaging cooling

SMARTEC will not only benefit FORTH but the country as a whole. The establishment of a qualified high-level infrastructure and the know-how coupled with the gained knowledge and the developed facilities will support high level training for the next generation of scientists. In addition, we aspire SMARTEC to support fabless Greek SMEs. The project phased serious delays due to the COVID pandemic but it is back on track and we expect that by the end of 2023 the pilot line will ship its first TRX prototypes.

[3] https://project-smartec.com/

AlN/GaN HEMT heterostructure grown on (111) HR Si substrate, with thin GaN/AlN buffer layer.

Kostopoulos A. [1, 2, 3, *], Adikimenakis A.[1, 2], Tsagaraki K.[1, 2], Kayambaki M.[1, 2], Kornilios N.[3], Konstantinidis G.[1,2] and Georgakilas A. [L]

[1] Foundation for Research and Technology-Hellas (FORTH), Institute of Electronic Structure and Laser (IESL), Heraklion, Greece

[2] Physics Department, University of Crete, Heraklion, Greece.

[3] Hellenic Mediterranean University (HMU), Department of Electrical & Computer Engineering, Heraklion, Greece

[L] Physics Department, University of Crete, Heraklion, Greece. and

Foundation for Research and Technology-Hellas (FORTH), Institute of Electronic Structure and Laser (IESL), Heraklion, Greece

*kosto@iesl.forth.gr

AlN/GaN heterostructure (HEMT) was grown on a high - resistivity (HR) Silicon (111) substrate by the plasma assisted molecular beam epitaxy (PAMBE) method. The HEMT structure was used for the fabrication of DC transistors achieved 2DEG density as 2 10^{13} cm^{-2}, mobility 660cm^2/Vs, maximum saturation current of 0.8 A/mm and maximum external transconductance of 160 mS/mm. Additionally the transistors exhibited 80 V source–drain breakdown voltage.

The wide energy band gap of AlN (Eg = 6,1eV), as well as its energy band discontinuity with GaN (ΔEc~ 1,9eV), render AlN/GaN HEMT heterostructures capable of producing transistors with very high current density for high power operation. The ability to develop high-quality crystalline AlN/GaN heterostructures on silicon (Si) substrates with the PAMBE method, as well as the need for only a thin buffer/isolation layer, that minimizes time in commercial-scale production, make these structures a financially attractive solution for industrial-level production of III-nitride HEMT structures on silicon substrates. A GaN/AlN/GaN/AlN heterostructure was grown on a HR Si (111) substrate by the PAMBE method. From bottom to top, the layers consisted of a 20 nm AlN buffer/back barrier, an 800 nm GaN channel layer, a 4nm AlN top barrier and a 1nm GaN as a cap layer. The GaN cap layer was used to avoid the oxidation effect of the AlN barrier surface as well as to ensure a higher charge density in the channel. The theoretical study of the energy bands diagram of the GaN/AlN/GaN/AlN heterostructure was carried out by solving the self-consistent[(1)] Schrödinger - Poisson equations. The energy diagram of the conduction band is shown in Figure 1 and the density of 2DEG was calculated to equal 1,5 $10^{13}cm^{-2}$.

An important point to mention is the small number of publications and scientific reports of nitride-based heterostructures on a Si substrate grown by the PAMBE method. Two problems make the development of GaN HEMT structures on Si by PAMBE an extremely difficult process. First point of reference is the difficulty of achieving epilayers with III - metal face polarity and second is the reaction of Ga droplets with the elements of substrates by the out-diffusion of Si atoms [(3)]. The above reasons are the main cause of the degradation of the

growing crystal. The growth conditions of the AlN/GaN HEMT structure using the PAMBE method are detailed in reference [(2)].

Unpassivated HEMTs, with gate width Wg = 125μm and gate length Lg ~ 1.5μm were fabricated using standard optical lithography techniques.

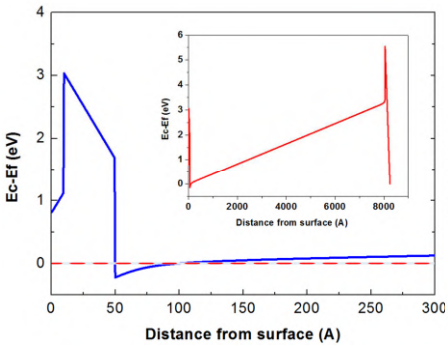

Fig 1: Simulated conduction band diagram (Ec) of the AlN/GaN double heterostructure for AlN top barrier thickness at 4nm.
The insert diagram presents the conduction band profile for the whole structure.

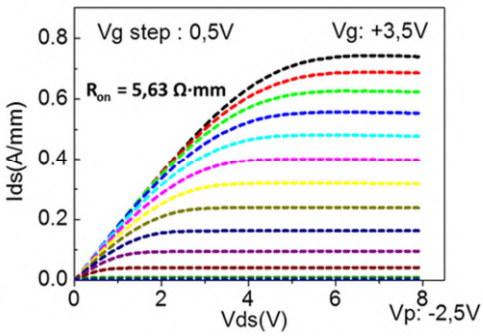

Fig.2: I–V characteristics of HEMT

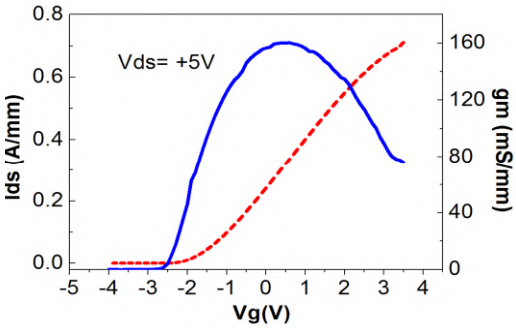

Fig. 3: Measurements of transconductance gm (Solid line) and saturation current I_{ds} (Dash line) as a function of applied gate voltage

The DC-voltage characteristics of the HEMT devices were measured with a tracer curve setup. Drain-source current densities of about 0.8 A/mm, at a positive applied gate voltage of Vg = +3.5V (Fig. 2) were obtained, as well as a low R_{on} of 5,63Ω·mm was measured. Despite the large applied positive voltage at the gate V_g = +3.5V, the leakage current was almost zero.. The extracted maximum external transcoductance was approximately 160 mS/mm at applied source-drain voltage of +5V (Fig. 3), while it was nearly constant over a large variation of the applied gate voltage.

The low threshold -2,5V voltage of the HEMT on Si makes it suitable for low-voltage device applications. Measurement of the drain–source breakdown voltage where the drain voltage is measured, while the gate voltage is swept and the drain current is kept at a constant 1mA.
Finally, the transistors exhibited a remarkably high breakdown voltage (V_{BR}) equal to 80V, for I_{ds}= 1mA (Fig. 4). The applied bias +80V V_{BR} in combination with the 1.75 μm gate - drain distance corespondes to a maximum electric field equal to 450KV/cm. The electricanl performance of the AlN/GaN HEMTs on HR Si (111) are considered particularly satisfactory given the thin 0.8 μm GaN buffer layer, compared to 4-5 μm thick structures, typical used in the literature as nitrides HEMT.

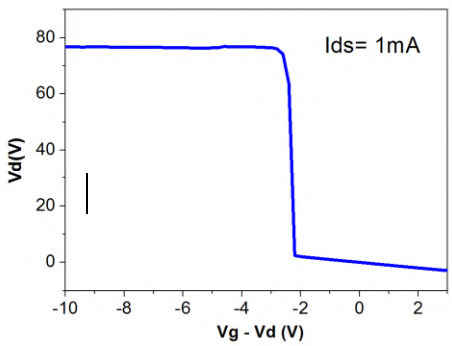

Fig. 4: Measurement of the breakdown voltage (V_{BR})

We acknowledge the financial support of this work by the project Hellenic Foundation for Research and Innovation (H.F.R.I.) under the "First Call for H.F.R.I. Research Projects to support Faculty members and Researchers and the procurement of high-cost research equipment grant" (Project Number: HFRI-FM17-3173 "EPINEET")

[1] H. Tan, G. L. Snider, L. D. Chang and E. L. Hu, JAP, 68, 4071 (1990)
[2] A. Georgakilas, EMRS 2022 Fall Meeting, Warsaw, Poland, September 19-22, 2022
[3] A. Adikimenakis, K. E. Aretouli, K. Tsagaraki, M.Kayambaki, and A. Georgakilas, Phys. Status Solidi C 10, No.1, 80–83, (2013)

Development of an Impedance Spectroscopy System for Biomedical Applications

A. Kallergis[1*], T. Koutsis[1], P. Tzani-Tzanopoulou[2], S. Taka[2], N. G. Papadopoulos[2], G. Kaltsas[1]

[1] microSENSES Laboratory, Department of Electrical and Electronics Engineering, University of West Attica, 122 43 Athens, Greece
[2] Second Pediatric Clinic, National and Kapodistrian University of Athens, Greece

*mscres-38@uniwa.gr

Impedance spectroscopy is a powerful technique that depicts the impedance of a system over a wide range of frequencies. In general, electrochemical impedance spectroscopy (EIS) uses electrical signals to extract the properties of an analyte. The analytes can be electrochemical cells, biological material, or even arrays of many analytes destined for quality control. Bio-impedance methods have gained attention due to their non-invasive and real-time nature [1,2]. Bio-impedance has proven valuable in cell barrier characterization, providing solutions to the determination of various biological parameters [3].

The main objective of this work is the development of a low-cost, accurate and versatile impedance spectroscopy system for biomedical applications (bio-ISS). More specifically, the developed system was built to be coupled with a specially designed microfluidic system (MS) that can continuously supply nutrients to epithelial cells cultured on Transwell inserts. The MS has embedded electrodes for direct connection to the presented device. The proposed device has the advantages of portability (operates as a stand-alone device with battery), wireless operation (presents the results in an android device via WIFI), and small size (PCB size 60x90mm). These features make it capable to operate inside a cell incubator, which is very important for biomedical applications.

The block diagram of the system is presented in fig. 1a and its operation consists of a few simple steps. First, the user switches on the bio-EIS, which communicates with a specially designed Android application (fig 1b). The bio-ISS sets up an ad-hoc Access Point with WPA2 security, to which the app's device connects automatically. A TCP server and client are started respectively in order to assure the communication of the device. In the next step the user selects the scanning parameters, including the upper and lower scanning frequency (min. 10Hz, max. 10KHz), scanning interval, etc. Instructions are then sent to the bio-EIS in JSON form by pressing a button (Fig. 1b). When the STOP button is pressed the procedure finishes and all the acquired data are saved with timestamps in .csv format.

The accuracy, stability, and repeatability were verified experimentally. In particular, accuracy was verified by taking the frequency response of known Randles equivalent circuits and using non-linear regression methods in MATLAB to extract the model parameters (fig. 2). The system is currently being evaluated using real cells with two approaches. The first approach is based on *in vitro* conditions utilizing a custom-made MS, and the second is implemented by 2D static conditions utilizing Transwell inserts and STX electrodes. Very promising results have been obtained so far, as depicted in fig. 3.

References

[1] G. Linz et al., Biosensors and Bioelectronics, Volume 165, 2020, 112345, ISSN 0956-5663; https://doi.org/10.1016/j.bios.2020.112345.
[2] D. Biswas et al., International Conference on Communications, Devices and Intelligent Systems (CODIS), Kolkata, 2012, pp. 508-511.
[3] D. A. Koutsouras, et al., Adv. Healthcare Mater. 2019, 8, 1901215; https://doi.org/10.1002/adhm.201901215.

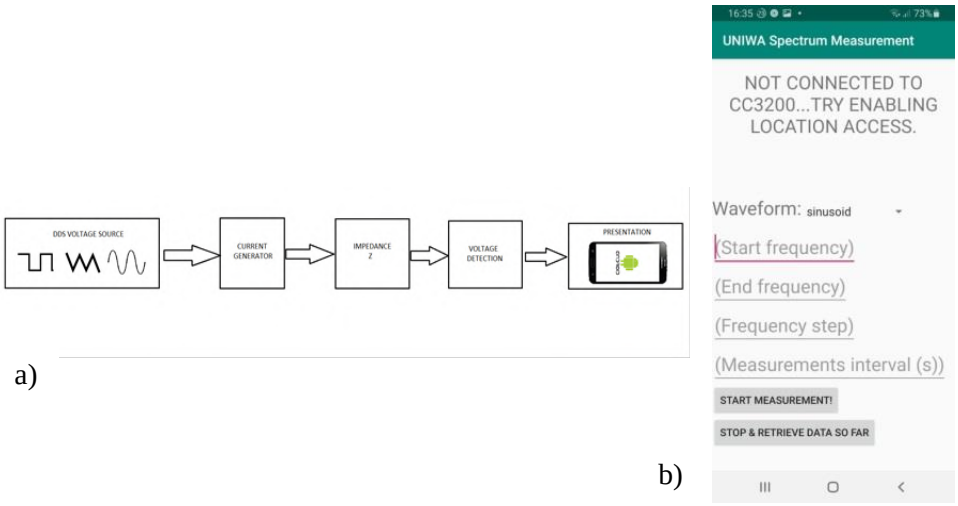

Fig.1. a) Block diagram of system's operation. b) Specially designed android application.

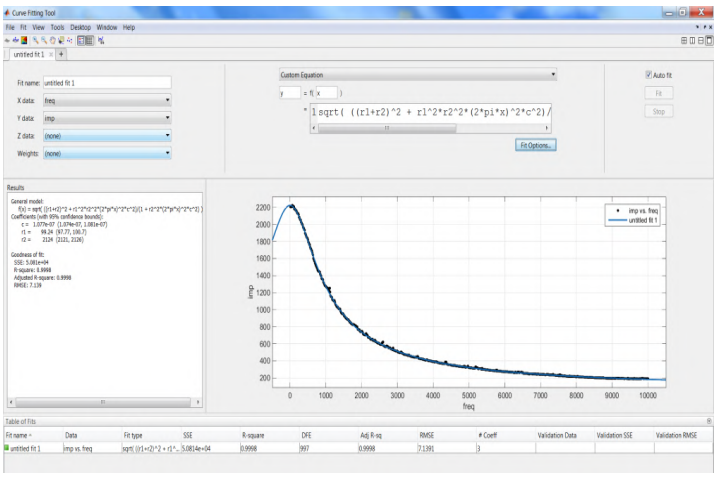

Fig.2. Porting a magnitude frequency response into MATLAB and using NLLSF to find the true parameters of the equivalent circuit. These 3 parameters in this case are found with errors of <1%, <1%, 3.5%.

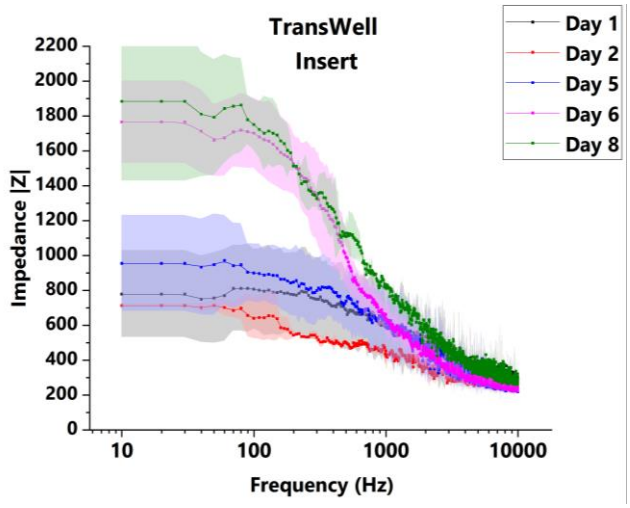

Fig.3. Impedance Measurements from a TransWell Insert with cells cultured for an 8-days period. The deviation represents three different measurements points on the TransWell Insert membrane.

A COMPARISON OF GRAPHENE AND CARBON NANOTUBES COMPOSITE ELECTRODES FOR SOLID AND LIQUID ELECTROLYTE SUPERCAPACITORS

Ioanna Lefa, George Zardalidis, and Filippos Farmakis

Micro- and Nano-Technology Lab, Electrical Engineering and Computer Engineering dept., Democritus University of Thrace, Vas. Sofias 12, 67100, Xanthi, Greece.

ilefa@ee.duth.gr

Background and Scope

Supercapacitors are energy storage devices with a considerable potential on power density and long cycle life. Especially, Electric Double Layer Capacitors (EDLCs) that electrostatically store charges on the interface of electrodes, offer a high specific capacitance (Fg^{-1}) depending on the active surface material of the electrode. Therefore, carbon-based materials, such as graphene, graphene oxide (GO) and carbon nanotubes (CNT) with a high surface-to-volume ratio are the most suitable. Further modification of these materials enhances their capacitive properties. GO/CNT hybrid films give rise to remarkable electrochemical performance with high specific capacitances as well as high retention rate of the initial capacitance after thousands of cycles (approximately 10,000 charge/discharge cycles). [1,2]

On the other hand, many applications require all solid-state energy storage supercapacitors in which the electrolyte is in solid phase. However, solid electrolytes suffer from low ionic conductivity, when compared to liquid electrolytes, and weak electrochemical properties.[3,4]

In this work, we manufacture and characterize supercapacitors with GO/CNT hybrid electrodes of various compositions and solid state supercapacitors. We investigate the analogy of GO and CNT with the best capacitive results and apply it to both liquid and solid electrolyte supercapacitors. We conclude on whether the manufactured all-solid-state supercapacitors are able to perform as well as conventional supercapacitors and what is their capacitive bottleneck.

Description of the Fabrication and Measurements

In this study, we investigated both conventional and all solid-state supercapacitors. Firstly, we fabricated and characterized conventional supercapacitors using GO, CNT and composite GO/CNT of various ratios as active materials and 1M H_2SO_4 liquid electrolyte. Then, for the most promising electrodes, we prepared solid-state supercapacitors with the aid of Polyvinyl Alcohol (PVA)/ H_2SO_4 solid electrolyte. It has to be noted that no binder was used for the electrode fabrication.

Experimental Results

It can be observed that when CNT participate in a greater percentage at the GO/CNT composite electrodes, the capacitance of the supercapacitor is increased (Figure 1). It was concluded that electrodes with GO/CNT ratio of 4:100 presented the most promising results in

terms of capacitance, hence, only a small amount of GO is needed in order to bind CNTs, which provide the higher surface-to-volume ratio.

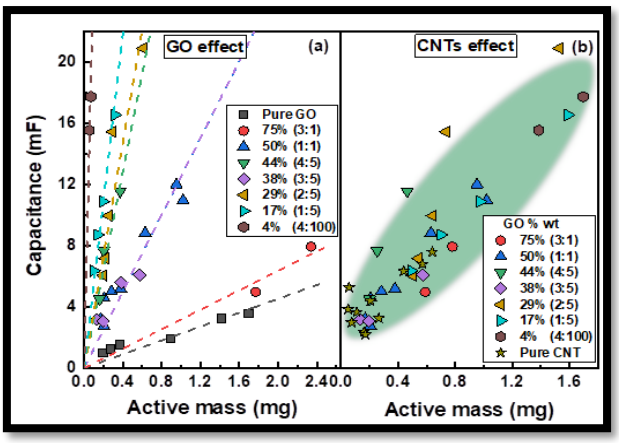

Figure 1: Comparison of the (a) GO and (b) CNT involvement in the cell capacitance

In a second phase, standard and solid-state supercapacitors with GO/CNT 4:100 electrodes of various mass loadings were compared in terms of specific capacitance as shown in Figure 2. Both types of devices exhibit similar specific capacitance achieving 43 Fg^{-1} at 0.22 mg of active material for solid-state supercapacitors and 45 Fg^{-1} at 0.25 mg of active material for conventional supercapacitors (Figure 2).

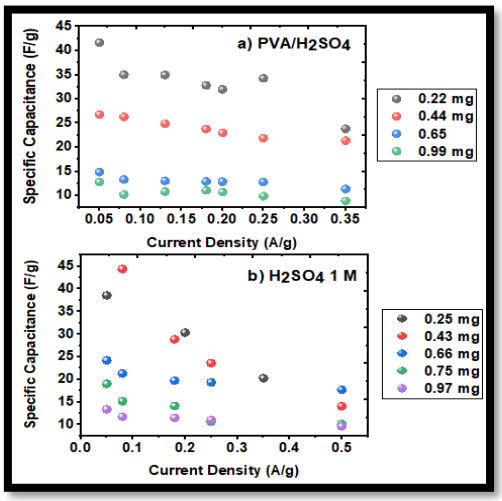

Figure 2: Specific Capacitance of GO/CNT 4:100 composite electrode supercapacitors in a) solid and b) liquid electrolyte at different current densities

REFERENCES:

[1] Zhang Hongxi, Cao Yudong , Chee Mason, Oliver Lam Dong Pei, Ye Mingxin, Shen Jianfeng, Nanoscale, 11, 5807-5821(2019)
[2] Portet, Taberna, Simon, Flahaut, Laberty-Robert, Electrochemica Acta, 50, 4174-4181(2005)
[3] Huang, Luo, Peng, Pu, Ger, Yang, Wu, Chang, Electrochemica Acta, 161, 371-377(2015)
[4] Alipoori, Mazinani, Aboutalebi, Sharif, Journal of Energy Storage, 27,101072(2020)

A platform of directly-immersible microfluidics-free silicon photonic probes as an enabling tool for the dairy industry

Konstantinos Misiakos[1], Michailia Angelopoulou[2], Dimitra Kourti[2], Panagiota Petrou[2], Sotirios Kakabakos[2], Ioannis Raptis[3], Dimitrios Goustouridis[3], Alexandros Salapatas[1] and Eleni Makarona[1,*]

[1]NCSR "Demokritos", Institute of Nanoscience and Nanotechnology, Athens, Greece

[2]NCSR "Demokritos", Institute of Nuclear & Radiological Sciences & Technology, Energy & Safety

[3]ThetaMetrisis S.A., Athens, Greece

*e.makarona@inn.demokritos.gr

Optical biosensors based on silicon photonic circuits are considered among the most promising candidates for the next generation of analytical systems especially for Point-of-Need/Point-of-Care (PoN/PoC) applications or situations that require accuracy and sensitivity in order for the users to make informed and/or expeditious and critical decisions. The main competitive advantages of silicon photonics that have rendered them so attractive are the on the one hand their ability to perform real-time label-free measurements of high detection sensitivity[1,2] and on the other hand the ability to be massively-produced at relatively low cost by an already established and maturity industry. Nonetheless, for truly viable analytical systems, most critical design factors are the simplicity of the measurement procedure (ideally, the user should only load the sample), the cost-effectiveness of instrumentation and consumables, the ability to work with complex matrices (e.g. blood, produce pulps and extracts, etc.), the portability, power autonomy and ease-of-use of the final system[3].

In this work, a novel optical biochemical sensing platform based on directly-immersible silicon photonic probes that are totally unburdened of the necessity for microfluidics or electrical interconnects (Fig. 1a), is presented. This novel platform takes advantage of an alternative and radical chip design containing only passive optical components and requiring a much simplified minimum-cost fabrication process suitable for mass production. The detection principle is based on Broad-band Mach-Zehnder Interferometry, which only requires the use of a white LED as the input source and which has already proven itself as a powerful analytical technique for dairy products[4,5]. The entire system is lightweight, portable and powered and controlled through a simple USB connection to a laptop (Fig. 1b). Signal recording and analysis is performed in real-time through a custom software via the same laptop used as the power source.

The system is currently explored as an enabling tool for the dairy industry and more specifically for the on-site determination of possible fraudulent activities of goat milk adulteration as well as the detection of Aflatoxin M1 (AFM1) in raw milk. So far, accurate detection of goat's milk adulteration with cow's milk, with a LOD of 0.14% (w/w) cow milk in goat milk was achieved in 12 min, while AFM1 can be detected in undiluted milk within 10min with a LOD of 5 pg/mL,

which is below the maximum allowable limit set by European Union (50 pg/mL).The excellent analytical characteristics of the assay developed make the proposed platform ideal for safety and quality assurance of raw milk on the spot.

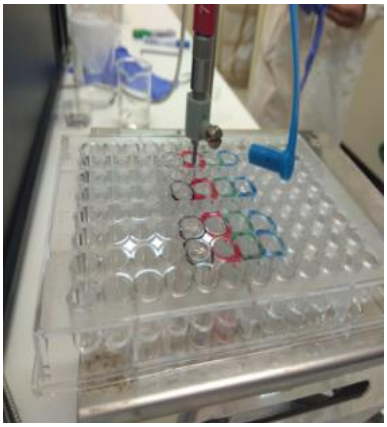

(a)

(b)

Fig.1 Photographs of (a) the immersible photonic probes during a measurement and (b) the biosensing platform in its carry-on case demonstrating its small size with respect to the laptop used for signal recording and powering.

Acknowledgments: This work has been funded by project "FOODSENS" co-financed by the ERDF of the EU and Greek national funds through the Operational Program Competitiveness, Entrepreneurship and Innovation, under the call RESEARCH – CREATE – INNOVATE; (project code: T2EΔK-01934)

[1] E. Luan, H. Shoman, D. M. Ratner, K. C. Cheung and L. Chrostowski, Sensors 18 (10), 1-38 (2018).
[2] A. Shakoor, J. Grant, M. Grande and D. R. S. Cumming, Sensors 19 (7), 57-59 (2018).
[3] F. Ligler and J. J. Gooding, Anal. Chem., 91, 8732−8738 (2019)
[4] M. Angelopoulou, P. S. Petrou, I. Raptis, K. Misiakos, E. Livaniou, E. Makarona and S. Kakabakos, Analyst, 146, 529-537 (2021).
[5] M. Angelopoulou, A. Botsialas, A. Salapatas, P. S. Petrou, W. Haasnoot, E. Makarona, G. Jobst, D. Goustouridis, A. Siafaka-Kapadai, I. Raptis, K. Misiakos and S. E. Kakabakos, Anal Bioanal Chem 407:3995–4004 (2015).

CuO/ZnO Heterojunction Devices on Silicon for Ultra-violet Optoelectronic Applications

Andreas Baltas[1,2], George P. Papageorgiou[1,3] and Eleni Makarona[1,*]

[1]NCSR "Demokritos", Institute of Nanoscience and Nanotechnology, Athens, Greece

[2]National Technical University of Athens, School of Applied Mathematical and Physical Sciences, Athens, Greece

[3]Department of Physics, University of Patras, Rio, Greece

*e.makarona@inn.demokritos.gr

The rapid development of the optoelectronics industry involves a variety of modern applications including thin-film transistor liquid crystal displays, organic light-emitting diodes, conventional and non-conventional light-emitting diodes (LEDs), solar cells, photodetectors (PDs) and more. Ultraviolet (UV) and visible (VIS) PDs and LEDs have been widely applied in chemical and biological analyses, space communication, air quality monitoring, flame monitoring, industrial quality control, optical imaging, missile warning systems, communications, security, astronomy and optoelectronic circuits. A semiconductor playing an important role in the new era of optoelectronic devices is ZnO with a wide bandgap (Eg = 3.37 eV) and a large exciton binding energy (60 meV) whose nanostructures attract increasing interest due to their variety of morphologies and availability of simple and low-cost processing[1]. As an alternative candidate to other costly materials, such III-Nitrides, SiC and II-VI semiconductors, ZnO has the great advantage that it can be produced with chemical methods that offer the potential of facile and cost-efficient scale-up, and of flexible processes that can produce tailor-made customizable morphologies. Hence, there is great value in fusing the mature, mainstream Si microfabrication techniques, pervasive to all electronic devices with production lines in place, with novel, cost-efficient chemically based techniques that produce ZnO and other metal oxide nanostructures and nanoarchitectures. Such a fusion is expected to lead to new approaches for the cost-efficient and versatile-in-design production of UV-VIS optoelectronic devices.

On the other hand, chemically-based approaches suffer from reduced repeatability, may result into nanostructure that are morphologically more complex and despite their apparent simplicity are hard to efficiently tune into the desirable structures[2]. To add to this complication, ZnO – rgardelss of production method- is inherently n-type and repeated attempts have been unsuccessful in producing stable, reproducible p-type conductivity with reasonably high carrier concentration, constraining the development of homojunction devices[3]. CuO has emerged as an alternative solution to this problem substituting for the p-type material and efforts are underway to produce CuO/ZnO heterojunctions for optoelectronic devices[4].

In light of all the above, this work is attempting at the same time a three-fold goal: (1) to effectively produce CuO/ZnO nanostructure heterojunctions via cost-efficient and facile

hydrothermal techniques (Fig. 1a), (2) merge them with mainstream Si-processes for the production of optoelectronic devices on Si-substrates (Figs. 1b,c), and (3) electrically characterize them in order to correlate the fabrication processes to the device performance and ultimately optimize the processing steps for specific applications (PDs, UV sensors, UV-VIS LEDs).

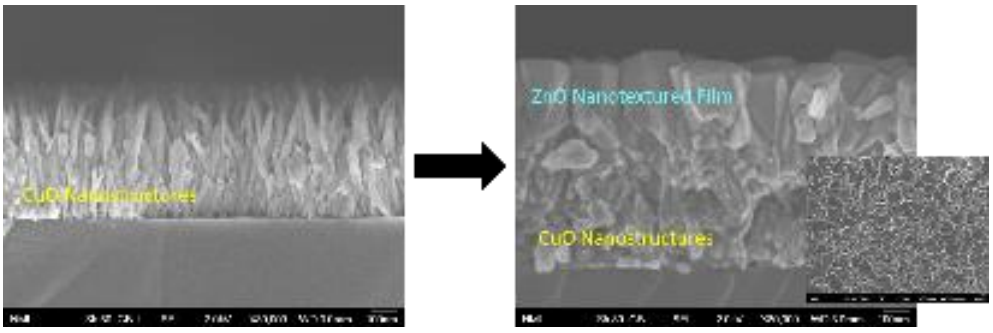

(a)

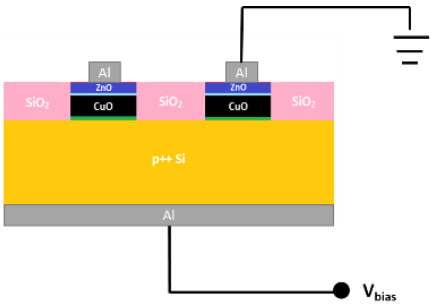

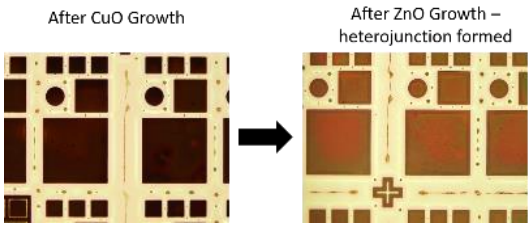

(b) (c)

Fig.1 (a) Cross-sectional SEM of hydrothermally grown CuO nanostructures on Si (100) (left) and the heterojunction formed on top of them with an over-layer of hydrothermally grown ZnO nanotextured film (right). Inset: top view of the ZnO film; (b) Schematic representation of the device architecture developed in this work; (c) Optical Microscope image of a device of CuO/ZnO on p^{++}-Si substrates prior to top contact formation.

[1] Handbook of Zinc Oxide and Related Materials, Vol. Two, Devices and Nanoengineering (ed. Zhe Chuan Feng), Taylor & Francis Group, LLC (2013).
[2] V. Constantoudis,I. Ioannou-Sougleridis, A. Dimou,, A. Ninou, M. Chatzichristidi,and E. Makarona, MNE 16, 100148 (2022).
[3] J. C Fan,.K.M. Sreekanth, Z. Xie, S. L.Chang and K. V.Rao, Prog. Mater Sci. 58, 874–985 (2013).
[4] P. Biswas, S.-D. Baek, S. H. Lee, J.-H. Park, S. J. Lee, T. I. Lee and J.-M. Myoung, Sci. Rep. 5:17961 (2015).

Experimental setup for magnetoresistance analysis of magnetic tunnel junctions and spin valves

O. Manos[a], A. Sigalos[a], E. Hourdakis[b], A. Kaidatzis[b], and D.Niarchos[a,b]

[a]*Amen New Technologies, Aghia Paraskevi, Attikis, 15310 Athens, Greece*

[b]*Institute of Nanoscience and Nanotechnology, NCSR Demokritos, Aghia Paraskevi, Attikis, 15310 Athens, Greece*

MagnetoResistance (MR) phenomena such as Giant MR (GMR)[1], Anisotropic MR (AMR)[2], and Tunneling MR (TMR)[3] effects refer to the variation of the electrical resistance of a material or a device with the application of an external magnetic field. Nowadays, GMR and TMR sensors have made possible the development of massive storage magnetic hard disks as well as solid state magnetic sensors. Low cost, compatibility with standard Complementary Metal Oxide Semiconductor technologies and high sensitivity are common advantages of these sensors.

The core element of a TMR/GMR sensor is a Magnetic Tunnel Junction (MTJ)/Spin Valve (SV), with one Non-magnetic (NM) insulating/metal layer sandwiched between two magnetic ones. The magnetization of the ferromagnetic layers can be either in the film plane or perpendicular to the film plane, which defines two kinds of MTJs: in-plane MTJs and perpendicular MTJs (p-MTJs), respectively. In these devices the tunneling/resistance probability depends on the relative orientation of the magnetization vectors of the two magnetic electrodes creating low or high resistance states. When the magnetizations of two magnetic layers are in parallel (P) or antiparallel (AP) configurations, the resistance of the device will be in low or high states, R_{low} and R_{high}, respectively, and the ratio of $(R_{high}-R_{low})/R_{low}$ is called the MR ratio of the device.

In this work, we designed and developed a measurement and automation equipment for measuring the TMR effect of a reference MTJ sample with the sequence of materials Sub/Ta/Pd/IrMn/CoFe/Ta/CoFeB/MgO/CoFeB/Ta/Pd[4] (see Fig. 1 (a)). The system is composed of a prober, a pA meter/DC voltage source, and an electromagnetic coil for the application of a variable magnetic field. We measured a series of I-V characteristics in the P and AP magnetic alignment of both electrodes. The TMR ratio was determined around 35% in consistency with previous measurements in the TMR setup of our collaborators[4]. The presented experimental setup allows the user to probe a series of magnetoransport phenomena (e.g., AMR, Spin Hall Magnetoresistance) with a simple modification of its components. Therefore, the capabilities of the setup underpin its significant contribution to the Greek scientific and industrial community.

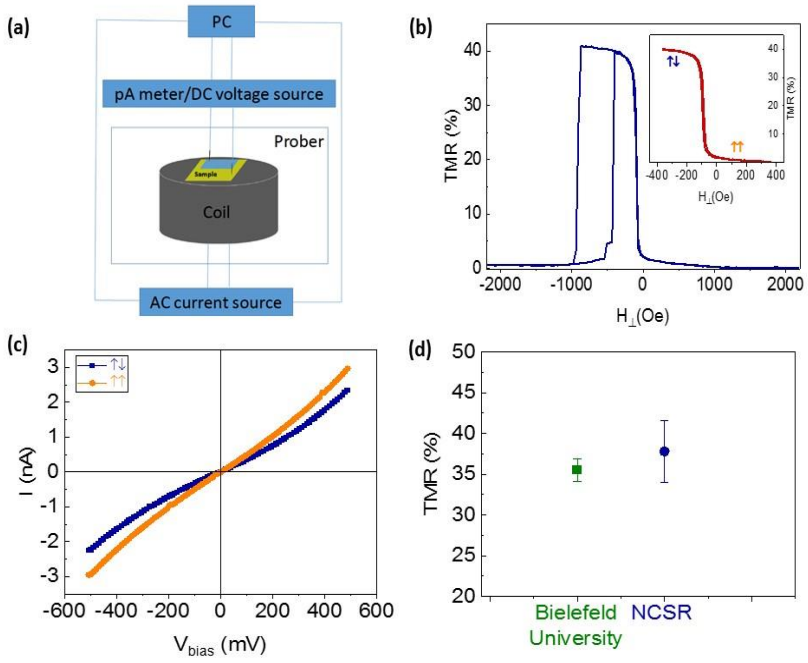

Figure 1. (a) Qualitative sketch of the TMR setup. (b) Major TMR hysteresis loop of the Sub/Ta/Pd/IrMn/CoFe/Ta/CoFeB/MgO/CoFeB/Ta/Pd sample. The inset shows the corresponding minor loop. With blue (orange) arrows are indicated the relative AP (P) orientations of the magnetizations of both electrodes. (c) I-V characteristics for the parallel (P-orange) and antiparallel (AP-blue) states of a p-MTJ. (d) Comparison between the TMR ratios measured at Bielefeld University and NCSR "Demokritos" for the same sample.

Acknowledgements

This work was supported by the NATO SPS programme in the framework of the Multi-Year Project "Spintronic Devices for Microwave Detection and Energy Harvesting Applications" (G5792), as well as by funding from Ministry of Education and Science of Ukraine (Project 0119U001483)

References

1. M. N. Baibich *et al.*, Phys. Rev. Lett. **61**, 2472 (1988); G. Binasch *et al.*, Phys. Rev. B **39**, 4828 (1989)
2. W. Thomson, "On the Electro-Dynamic Qualities of Metals:–Effects of Magnetization on the Electric Conductivity of Nickel and of Iron", Proc. R. Soc. Lond. 8, **546** (1856).
3. T. Miyazaki and N. Tezuka, "Giant magnetic tunneling effect in Fe/Al2O3 /Fe junction", J. Magn. Magn. Mater. **139**, L231 (1995)
4. O. Manos, P. Bougiatioti, D. Dyck, T. Hübner, J. Schmalhorst and G. Reiss, J. Appl. Phys. **125**, 023905 (2019).
5. O. Manos, A. Böhnke, P. Bougiatioti, R. Klett, K. Rott, A. Niesen, J. Schmalhorst and G. Reiss, J. Appl. Phys. **122**, 103904 (2017).

Effect of SOI substrate on MIS silicon nitride resistance switching structures

A.E. Mavropoulis[a*], N. Vasileiadis[a,b], C. Theodorou[c], L. Sygellou[d], P. Normand[a], G. Ch. Sirakoulis[b], P. Dimitrakis[a]

[a] *Institute of Nanoscience and Nanotechnology, NCSR "Demokritos", Ag. Paraskevi 15341, Greece*
[b] *Department of Electrical and Computer Engineering, Democritus University of Thrace, Xanthi 67100, Greece*
[c] *Univ. Grenoble Alpes, Univ. Savoie Mont Blanc, CNRS, Grenoble INP, IMEP-LAHC, 38000 Grenoble, France*
[d] *Institute of Chemical Engineering Sciences, FORTH/ ICE-HT, Patras 26504, Greece*

*a.mavropoulis@inn.demokritos.gr

Several resistive memory technologies (RRAMs) are prominent, but few are fulfilling the requirements for CMOS integration and meet the commercialization standards. SiN_X was found to exhibit competitive resistance switching (RS) properties and attractive SiN-based RRAM devices have been recently demonstrated [1-3]. In the majority of the publications, the RS SiN_X structures are metal-insulator-semiconductor (MIS), meaning that the bottom electrode was n^{++} Si. In this work, the fabrication and electrical characterization of a fully compatible CMOS process on SOI substrate of 1R SiN-based resistance switching MIS devices is presented. The RS characteristics are compared with the same devices previously fabricated on bulk silicon. The scope of this work is to benchmark the use of thin SOI film as bottom electrode compared to bulk Si substrates in single MIS 1R cells utilizing low-frequency noise, DC and AC measurements.

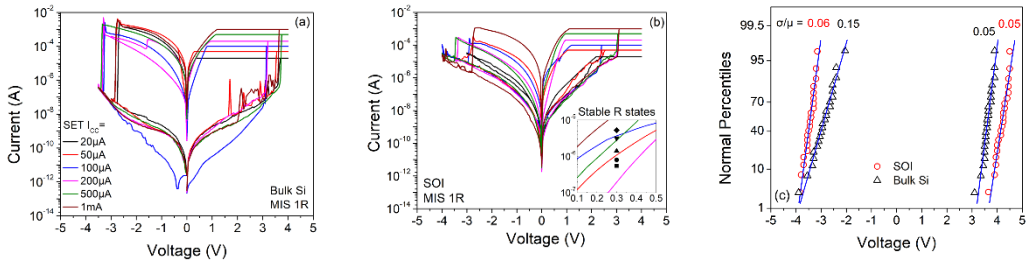

Figure 1: I-V switching characteristics at different I_{CC} for a) bulk Si substrate, b) SOI substrate 1R cells. c) SET/RESET voltage statistics.

Multiple sequential SET/RESET voltage sweep cycles at different current compliance levels (I_{cc}) for the bulk and SOI MIS 1R cells are shown in Fig. 1a and 1b, indicating their potential for resistance switching at multi-levels. A clear bipolar operation is observed for both bulk and SOI 1R cells with almost symmetrical V_{SET} / V_{RESET}. Nevertheless, the resistance window is significantly lower for SOI cells, which is related to their lower HRS value compared to cells on bulk Si. Evidently, the current overshoot after SET is more pronounced in the case of bulk Si cells, meaning that SOI devices exhibited self-compliance characteristics. This is mainly

attributed to the parasitic capacitance due to prober's chuck capacitance and the bulk Si substrate resistance. In addition, the SOI MIS 1R cells showed a significant improvement in endurance and retention characteristics, as shown in Fig 2a and 3b. More specifically, the LRS decay rate is improved three times at room temperature. The memory window was stabilized after 30 I-V sweeps, due to the reduction of the filament length.

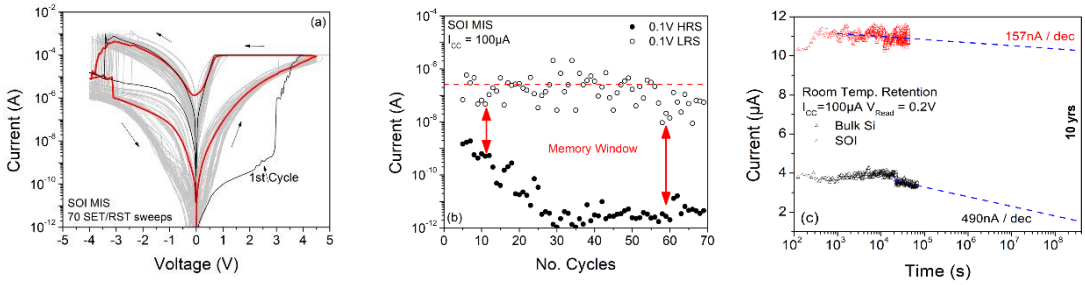

Figure 2: a) Multiple SET/RESET cycles of SOI 1R cells. b) HRS/LRS current values after multiple operation cycles. c) Retention characteristics of SOI and bulk Si MIS 1R cells.

The Nyquist plots for LRS (Fig. 3b) show that bulk Si MIS 1R cells are SET at lower resistance compared to SOI cells due to the enhanced current overshoot and the series resistance. LRS Nyquist graphs are semicircles and thus can be modelled successfully by an equivalent circuit with a resistance in parallel to a capacitance, Rp || Cp and a serial resistance Rs, as described in the inset of Fig. 3(b). Physically, Rp and Cp correspond to the resistance of the conductive paths formed during SET and the capacitance of the remaining insulating (no-switched) material region, respectively. Low-frequency noise spectral analysis indicated that there is no additional group of characteristic traps related to the SOI substrate.

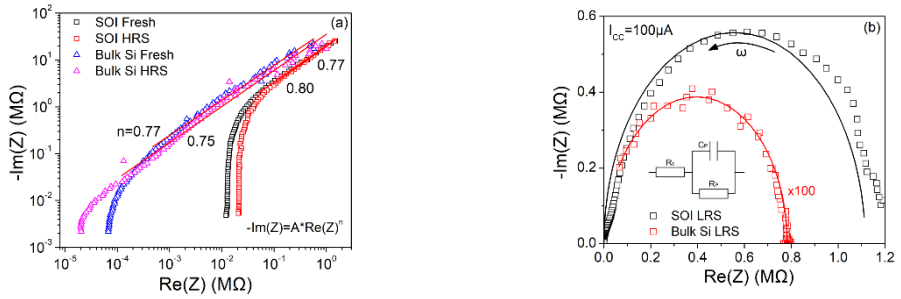

Figure 3: Nyquist plots at (a) Fresh and HRS and (b) LRS, for bulk Si and SOI MIS 1R cells

Acknowledgements

This work was financially supported by research project "3D-TOPOS" (MIS 5131411) funded by GSRI.

References

[1] N. Vasileiadis, et al., IEEE Trans. on Nanotechnology 20 (2021): 356-364

[2] N. Vasileiadis, et al., Materials 2021, 14, 5223

[3] N. Vasileiadis, et al., Chaos, Solitons & Fractals 153 (2021): 111533

Modeling the Resistive-Switching Characteristics of Silicon Nitride ReRAM devices: A TCAD approach

Emmanouil Stavroulakis[1,2], Nikolaos Vasileiadis[1,2], Alexandros Mavropoulis[1], Panagiotis Dimitrakis[2] and Georgios Ch. Sirakoulis[1]

[1] Department of Electrical and Computer Engineering, Democritus University of Thrace, Xanthi, 67100, Greece

[2] Institute of Nanoscience and Nanotechnology, NCSR "Demokritos", Ag. Paraskevi 15341, Greece

*emmastav5@ee.duth.gr

Memristors, also known as "memory resistors", have been primarily investigated as essential components in artificial synapse systems, where the memristor serves as the synaptic weight between two nodes utilizing its resistive-switching properties. Among different types of memristor devices, ReRAM have emerged as a great candidate for the integration of synaptic weights in neuromorphic hardware. Especially Si_3N_4 based ReRAM devices' showcase intriguing performance characteristics of low switching threshold, high endurance and retention that lay the foundations for the development of the next-generation low-power artificial synaptic devices. In this work, an approach to accurately simulate resistive-switching of Si_3N_4 memristors using Synopsys Sentaurus – an industry standard suite of TCAD tools which models and simulates the fabrication process, operation and reliability of semiconductor structures. Sentaurus' Kinetic Monte Carlo (KMC) engine is used to model and simulate the temporal dynamics of the conductive filament (CF) formation and recession. The CF is modelled as nitrogen vacancies which act as electron traps, consistent with experimental data showing conductivity in Si_3N_4 films having high nitrogen vacancy concentrations. Pulse train stimuli is applied to the system – which consists of nitrogen ions, mobile vacancies and immobile vacancies, and its IV characteristics are obtained. The occurrence rate of KMC events supported are governed by a single equation. The parameters for this equation, for each particle type present in the device, are obtained using the optimization framework provided by Synopsys Sentaurus. This simulation approach allows for direct visualization of the CF electrostatics as well as the incorporation of a nonlocal, trap-assisted-tunnelling model to approximate current voltage characteristics during the switching event. Effective masses and work functions for the Top Electrode (TE) and Bottom Electrode (TE) are considered as influencing parameters to the CF dynamics. As illustrated, this method may be utilized to offer information at both the device and circuit level, such as forming voltage, resistance levels and success rate of programming operations.

Drain current global variability analysis in nanoscale junctionless FinFETs utilizing a compact model

T.A. Oproglidis,[1,*] A. Tsormpatzoglou[2], D.H. Tassis,[1] and C.A. Dimitriadis[1]

[1]Department of Solid State Physics, Aristotle University of Thessaloniki, Thessaloniki, 54124, Greece

[2]Department of Informatics and Telecommunications, University of Ioannina, Arta, 45110, Greece

*thoprogl@physics.auth.gr

This work investigates the global variability in nanoscale triple-gate junctionless FinFETs utilizing an analytical symmetric and continuous compact model[1] combined with Monte Carlo simulations. Initially, the device parameters are extracted from the experimental transfer characteristics, such as threshold voltage, ideality factor, low-field mobility, source-drain series resistance, channel length modulation factor and mobility degradation factor. Then, statistical analysis is performed to calculate the mean values and standard deviations of the differences of the aforementioned parameters for a large number of devices with reference to the mean value of all dies. Monte Carlo simulations allow the compact model to reproduce successfully the drain current global variability.

The Si n-channel TG JLTs were also fabricated at IMEC (Leuven, Belgium) and have fin height H_{fin} = 37 nm, fin width W_{fin} = 11 and different channel lengths while maintaining the same number of fins. For global variability, channel length varies from 34 nm to 101 nm and the number of fins is fixed to 4. The analysis of this paragraph refers to 4-fins transistors with three different gate lengths, namely 34, 71 and 101nm. Initially, typical I_d-V_g characteristics of the experimental data of global variability with L = 34 nm, 45 nm and 101 nm are presented in Fig. 1.

The drain current global variability is calculated using the expression $\Delta I_d / I_d$, where I_d is the mean value of the drain current and ΔI_d is the difference between I_d and the drain current of each of the devices for a certain value of the gate voltage, V_g. Fig. 2 showcases the outcome of the application of $\Delta I_d / I_d$ on the global variability investigation; the dispersion of the drain current variability is significantly larger in the subthreshold region (V_{gt}<0) for all channel lengths and becomes smaller as the gate voltage increases and the transistors reach accumulation.

The utilization of the analytical compact model allowed the extraction of the mean values and standard deviations of the model parameters (V_t, μ, η, R_{sd}).[1] These values were employed to execute Monte – Carlo simulation with a Gaussian distribution of σ. The I_d – V_g characteristics were reproduced

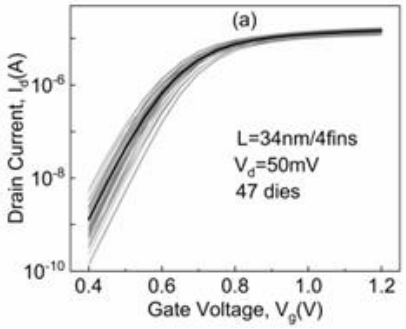

Fig. 1: Typical I_d – V_g characteristics of TG JLTS

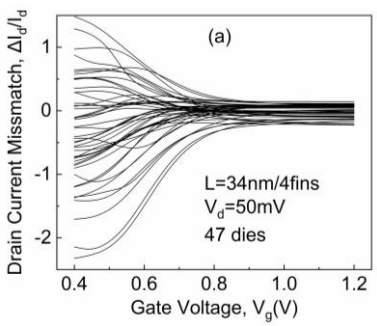

Fig. 2: I_d variability vs gate voltage (V_g)

[1] T.A. Oproglidis et al., IEEE TED, vol.67, 2, pp.4486 (2019)

by simulating a number of devices equal to ten times the number of the measured devices. Fig. 3 reveals the results of the Monte-Carlo simulations. The global variability of TG JLTs is reproduced accurately by possessing the same subthreshold dispersion that is evident in Fig. 2.

Then, the analysis quantification of the drain current global variability followed[2]. Fig. 4 presents the plots of $\sigma^2(\Delta I_d/I_d)$ versus V_g for a channel length of L = 34nm. The lines represent the Monte-Carlo simulated data of $\sigma^2(\Delta I_d/I_d)$ produced from the compact model and the symbols the experimental results of $\sigma^2(\Delta I_d/I_d)$. The model proves to be accurate by closely reproducing the plot curve.

It is possible to investigate the on-current of the devices by comparing experimental and simulated data. The experimental mean values of I_{on} as well as the deviation of the on-current ($\sigma\Delta I_{on}$) were calculated at V_g= 1.0V and V_d= 50mV. The same process was followed to extract the mean values and standard deviations of the on-current for the Monte-Carlo simulated devices. Fig. 5 presents this comparison for a length of 34nm with a selection of V_g = 1.0V and V_d = 50mV. The bars show the distribution of the experimental data whereas the lines are used to represent the distribution of the simulated data. The results of Fig. 6.27 show good accuracy in terms of I_{on} and $\sigma\Delta I_{on}$. Additionally, there is good accordance with the on-currents distributions of the experimental and the Monte-Carlo simulated data. The global variability analysis of this paragraph showcases that the compact model is suitable for variability-prediction purposes.

Finally, the decomposition of the on-current variability to its variation sources can be achieved with the utilization of the compact model.[3] At first, the total variation σI_{on} is calculated with the inclusion of the experimental mean values and standard deviations of all model parameters. Then, one parameter maintains its standard deviations and the others are given their fixed mean values.

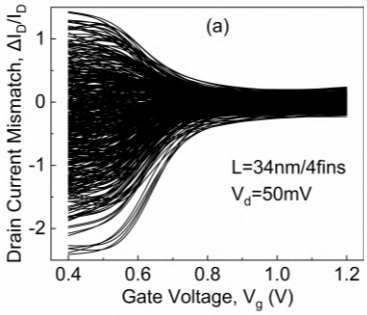

Fig. 3: Reproduced $I_d - V_g$ Monte Carlo characteristics

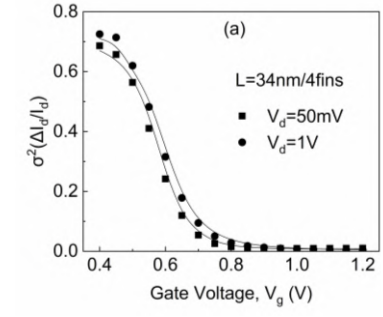

Fig. 4: Squared standard deviation of I_d vs V_g

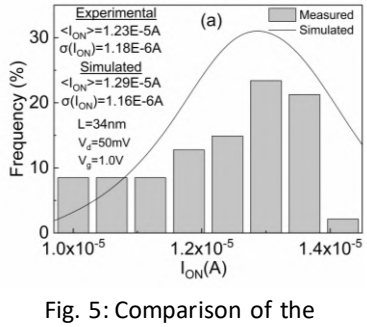

Fig. 5: Comparison of the distributions of I_{on}

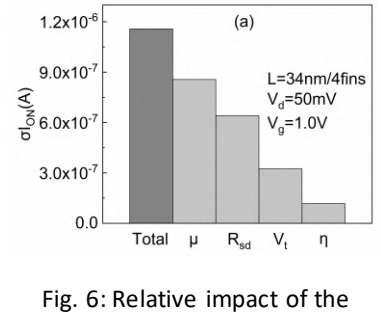

Fig. 6: Relative impact of the model's parameters to the total σI_{on}

In order to investigate the contribution of every parameter to the total σI_{on}, this process was repeated for all the parameters of the compact model. Each time, the deviation in the on-current derives solely from the deviating parameter and thus its contribution to the total σI_{on} is revealed. The results are presented in Fig. 6 for L = 34nm. The mobility as well as the series resistance are the main contributors to the on-current variability of TG JLTs when it comes to relatively short channel lengths.

[2] C.C. McAndrew, IEEE TED, vol.66, 1, pp.12, 2019

[3] T. Matsukawa et al., ECS Transactions, vol.45, pp.231, 2012

Active Load Inverter Design based on FORTH FET technology based on bilayer MoS_2

Alexia Papadopoulou[1,*], Fabrice Iacovella[1], George Fanourakis[1,2] and George Deligeorgis[1,L]

[1] Foundation for Research and Technology Hellas (FORTH), Institute of Electronic Structure and Laser (IESL)N. Plastira 100, Vassilika Vouton, Heraklion 70013, Crete, Greece

[2] Department of Materials Science and Technology, University of Crete,Heraklion 70013, Greece

* alpapadopoulou@iesl.forth.gr

The ongoing research on two-dimensional (2D) materials, such as graphene and transition-metal dichalcogenides (TMDCs), is setting the path for a new generation of nanoelectronics. Specifically, molybdenum disulfide (MoS_2), among TMDCs, is being extensively studied and successfully used as a channel material in field-effect transistors (FETs). MoS_2 is a suitable candidate as channel material due to its high crystalline quality and high level of thickness scaling, mandatory attributes for the miniaturization of electronic circuits. [1], [2]

In this work, we explore the possibility of designing a simple inverter circuit which is the building block for both analogue and digital applications and present simulations of an active load inverter using the process design kit which is developed for FORTH's in-house second generation technology of 450nm normally ON MoS_2 FETs.[3]

The layout of the MoS_2 FET is depicted In Fig.1a. A dedicated design kit for Cadence ® EDA tool is in constant development in order to cover MoS_2 FET static and dynamic behaviour. Its DC behaviour was modelled using Stanford 2D Semiconductor (S2DS version 1.2.0) Verilog-A model and its good agreement with the measurements is demonstrated in Fig.1b. [4]

In Fig.2 (a) an inverter implementation is demonstrated, using the custom MoS_2 FET graphic symbol, and in Fig.2 (b) the simulation results for the voltage transfer characteristics of the inverter are presented in three different transistor sizing ratios. Due to the lack of p-type MoS_2 device, the pull up network is designed with the available n-type MoS_2 device connected as active load. The dimensions of each device are critical to define the inverter switching point and it is shown in Fig.2 (b) that with an increase in ratio the switching point increases. By achieving a rail-to-rail output voltage swing, the design of logic gates is made plausible. In conclusion, we show that MoS_2 FETs can be used as an alternative to traditional CMOS technologies.

[1] L. Yu, D. El-Damak, U. Radhakrishna, X. Ling, A. Zubair, Y. Lin, Y. Zhang, M.-H. Chuang, Y.-H. Lee, D. Antoniadis, J. Kong, A. Chandrakasan, and T. Palacios, Nano Lett., 16(10), 6349-6356(2016)
[2] B. Radisavljevic, M. Br. Whitwick, and A. Kis, ACS Nano, 5 (12), 9934-9938(2011)
[3] L. Wang, L. Chen, S. L. Wong, X. Huang, W. Liao, C. Zhu, Y.-F. Lim, D. Li, X. Liu, D. Chi, K.-W. Ang, Adv. Electron. Mater., 5, 1900393 (2019).
[4] S. V. Suryavanshi and E. Pop, J. Appl. Phys. 120, 224503 (2016)

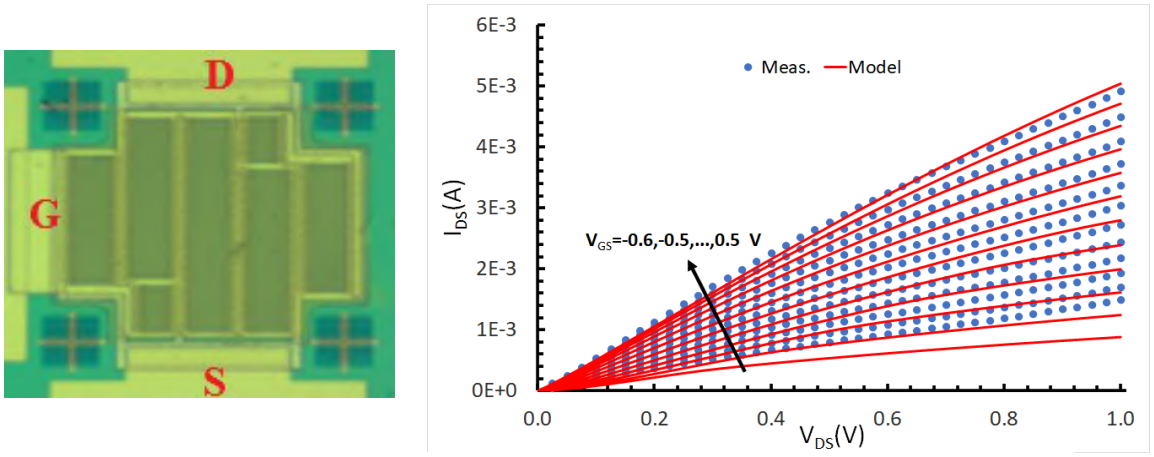

(a) **(b)**

Fig.1(a) FORTH MOS2 FET SEM picture (b) MOS2 FET (W=2.7mm & L=450nm) Output Characteristic, VGS= -0.6 to 0.5V@T=25oC

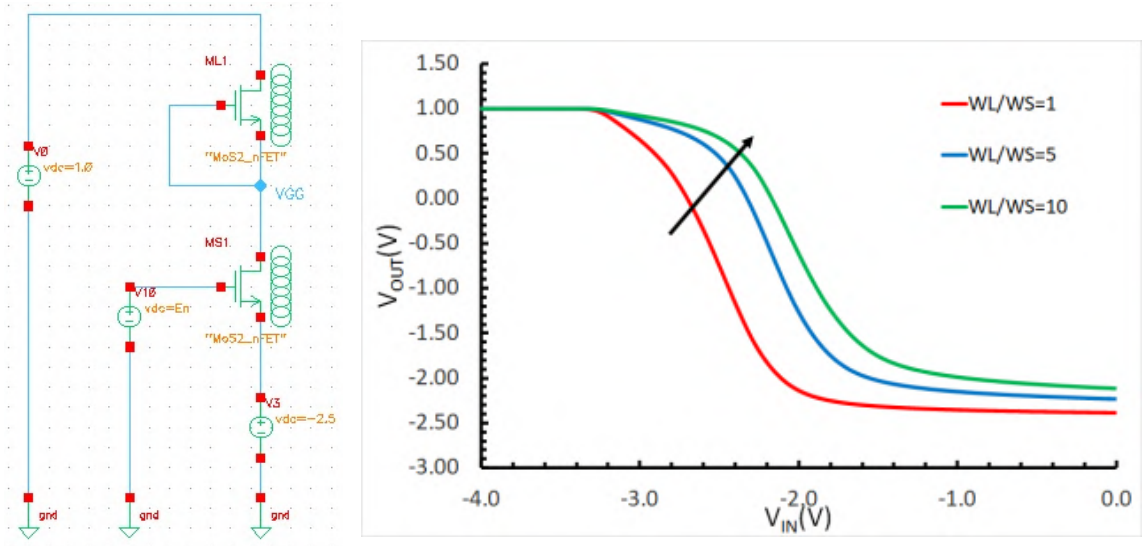

(a) **(b)**

Fig.2 (a) FORTH MOS2 inverter schematic testbench (b) MOS2 inverter Voltage Transfer Characteristics

Intermodulation phenomena in MEMS capacitors operating in Field Emission and Townsend breakdown regimes

J. Theoharis[1], G. Konstantinidis[2], and G. Papaioannour[1,*,]

[1] Condensed Matter Physics Section, Physics Dot, University of Athens, Athens, Greece

[2]IESL FORTH, Heraklion Greece

gpapaioan@phys.uoa.gr

RF-MEMS capacitive switches are very attractive for their linearity at high frequencies up to GHz. These devices operate in two discrete states OFF-state (pull-out) when the moving armature is in the up-state and ON-state (pull-in) when the moving armature has landed on a dielectric film, The device is actuated by applying a voltage larger than the pull-in voltage (V_{pi}) (Fig.1) and released when the applied voltage is smaller than the pull-out (V_{po}) one. During pull-in state the applied electric field exceeds the level of 1MV/cm. This is locally increased due to surface roughness and the presence of asperities and gives rise to field emission in dielectric-less areas[1] or through the dielectric film[2]. The field emission induced harmonic generation has been investigated when a microwave signal of large amplitude is superimposed on the DC applied bias [[3]]. In spite of this no investigation has been done on the low-level signal intermodulation.

The field emission current is given by the Fowler-Nordheim equation, hence when two RF signals of amplitudes v_{RF1}, v_{RF2} and frequencies f1, f_2 respectively are superimposed over a DC one (V_{DC}) the current through the gap of an RF MEMS switch should be

$$I(t) = A[V_{DC} + v_{RF1}sin(2\pi f_1 t) + v_{RF2}sin(2\pi f_2 t)]^2 \times e^{-\frac{B}{V_{DC}+v_{RF1}sin(2\pi f_1 t)+v_{RF2}sin(2\pi f_2 t)}} \quad (1)$$

In Eq. (1), A and B are constants (explained in detail in [[4]]) related with the emitting area and the field enhancement factor. In the case of low-level RF signals ($v_{RF1}, v_{RF2} \ll V_{DC}$) Eq1 can be simplified to

$$I(t) \cong I_{DC}\left(1 + 2\frac{v_{RF1}(t)+v_{RF2}(t)}{V_{DC}}\right) \times exp\left[-\frac{B(v_{RF1}(t)+v_{RF2}(t))}{V_{DC}^2}\right] \quad (2)$$

where I_{DC} is the DC current in absence of RF signals. Considering Eq.2 we are led to the conclusion than when low level signals are superimposed the intermodulation process arises from the exponential term.

The intermodulation process has been investigated with MEMS capacitors, which design was same with RF MEMS capacitive switches but with a gap of 1.5μm and rigid bridge (6μm thick)

[1] J. Theocharis, S. Gardelis, G. Papaioannou, "Effect of Ambient on the Field Emission Induced-Damage in Dielectric-Less MEMS Capacitive Structures|, IEEE Transactions on Device and Materials Reliability Vol. 22, pp. 205 – 21,6(2022)

[2] J. Theocharis, S. Gardelis, G. Papaioannou. "Impact of dielectric film thickness on field emission in MEMS capacitive switches". Microelectronics Reliability, accepted for publication

[3] L. Michalas, G. Konstantinidis and G. Papaioannou, "RF Signals over Field Emission Currents: A Theoretical Study for MEMS Capacitive Switches", Microelectronics Reliability, accepted for publication

[4] Wong TKS, Ingram SG. Observation of Fowler-Nordheim tunnelling at atmospheric pressure using Au/Ti lateral tunnel diodes. J. Phys. D: Appl. Phys. 26 (1993) 979-985.

so that to minimize any displacement when applying high voltages across the capacitor. A bias-T was designed to withstand voltages more than 300V and flat response up to 1GHz. The RF signals frequencies were 520MHz and 560MHz to avoid any interference from bridge series inductance and any intermodulation effect from substrate parasitic back-to-back MOS capacitors. Fig.3 shows the typical V-I characteristic with sequential breakdown processes. Fig.3 shows typical V-I characteristic of gas discharge and Fig,4 the schematic of experimental setup for simultaneous DC and RF measurements. The DC I-V characteristic showing the Townsend and subnormal glow discharges is presented in Fig.5. The magnitude of superimposed RF signals is shown in Fig.6 and the intermodulation results at 40MHz and second harmonic at 80MHz are shown in Fig.7a and b respectively. The investigation has been extended on capacitors with a thin dielectric film with thickness of 50nm, 100nm and 200nm. The impact of field emission current intensity as well as the onset of Townsend breakdown on the intermodulation efficiency is analyzed. The analysis is extended on the presence of dielectric barrier (Fig.9).

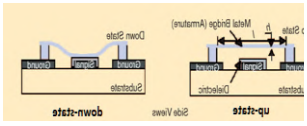

Fig.1 RF MEMS capacitive switch

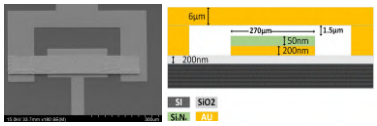

Fig.2 The MEMS capacitor

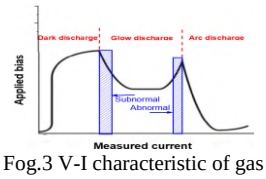

Fog.3 V-I characteristic of gas discharge

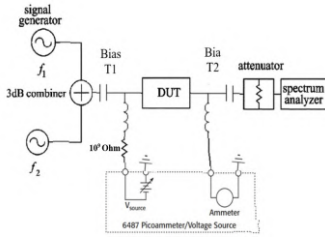

Fig.4 DC & RF measurements setup

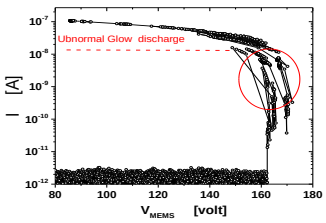

Fig.5 I-V characteristic of MEMS capacitor

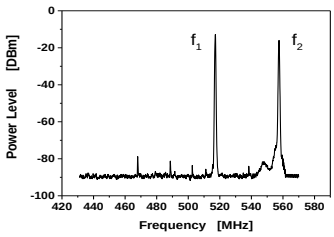

Fig.6 Superimposed RF signals spectrum

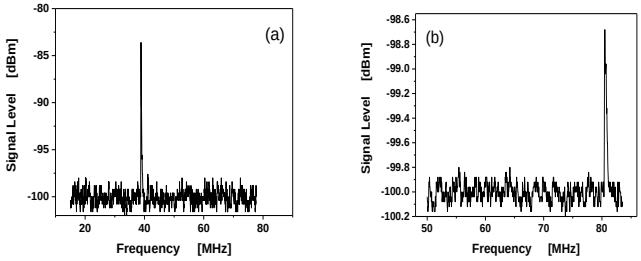

Fig.7 Intermodulation products at 40MHz and second harmonic at 80MHz

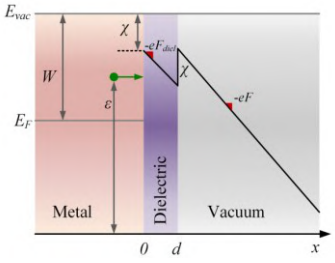

Fig.9 Field emission through dielectric barrier

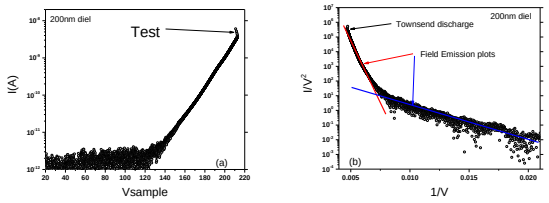

Fig.10 (a) I-V characteristic and (b) Fowler-Nordheim plot

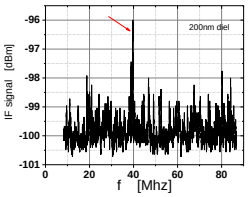

Fig.11 Intermodulation spectrum

Magnetic Nanoparticles/Epoxy Resin Hybrid Nanocomposites: Development, Characterization and Multifunctionality

A. C. Patsidis[1,*], S. Gioti[1], A. Sanida[1], G. C. Manika[1], G. N. Mathioudakis[2], N. Petropoulos[3], A. Kanapitsas[3], C. Tsonos[3], Th. Speliotis[4], and G. C. Psarras[1]

[1]Smart Materials &Nanodielectrics Laboratory, Department of Materials Science, School of Natural Sciences, University of Patras, Patras 26504, Greece

[2]Institute of Chemical Engineering Sciences (ICE-HT), Foundation for Research & Technology Hellas (FORTH), 26504 Patras, Greece

[3]Department of Physics, University of Thessaly, Lamia, Greece

[4]Institute of Nanoscience and Nanotechnology, NCSR "Demokritos", Athens 15310, Greece

*patsidis@upatras.gr

Nowadays, polymer matrix nanocomposites are considered an important class of engineering materials for various technological applications. Epoxy resins are the most popular matrices for the development of advanced composites, since they are characterized by low weight, ease of processing, flexibility, good wetting and adhesion with the majority of the employed fillers, at low cost. Their properties can be improved by integrating various fillers, which advance their thermomechanical properties, dielectric and electrical response, magnetic properties, and the ability to store and recover electrical energy. By these means, multifunctional performance can be induced by integrating suitable fillers, which exhibit supplementary properties/responses[1-4].

In this study series of hybrid epoxy nanocomposites with magnetic nanoparticles (Fe_3O_4, or $ZnFe_2O_4$, or $SrFe12O_{19}$) and $BaTiO_3$ or multiwall carbon nanotubes (MWCNTs) have been prepared and studied. Fabricated hybrid systems should be able to respond under various loading conditions, exhibiting suitable mechanical/thermal properties, tunable electric conductivity, variable electric polarization/dielectric permittivity, adjustable magnetic response, and thermally induced phase changes. All these responses contribute to the overall multifunctional performance. $BaTiO_3$ particles provide functionality to the systems, via their thermally induced ferroelectric to paraelectric transition, while CNTs enhance mechanical endurance and electrical conductivity. Hybrid nanocomposites were characterized by means of Scanning Electron Microscopy (SEM), X-Ray Diffraction (XRD), Differential Scanning Calorimetry (DSC), Thermogravimetric Analysis (TGA), Dynamic Mechanical Analysis (DMA), Static Mechanical tests, Environmental effects (effects of hydration and ultra-visible radiation) and Storing/Recovering energy under dc conditions. Results imply the successful fabrication of nanocomposites and the fine dispersion of the inclusions. Thermal stability is enhanced by the presence of reinforcing phases and both static and dynamic properties of the systems are improved. Systems with MWCNTs exhibit increased conductivity, while systems with barium titanate present adjustable polarization/dielectric response and are able to

store/recover energy. Finally, magnetic particles induce magnetic properties to the nanocomposites, which vary with the type and the mount of the employed magnetic phase.

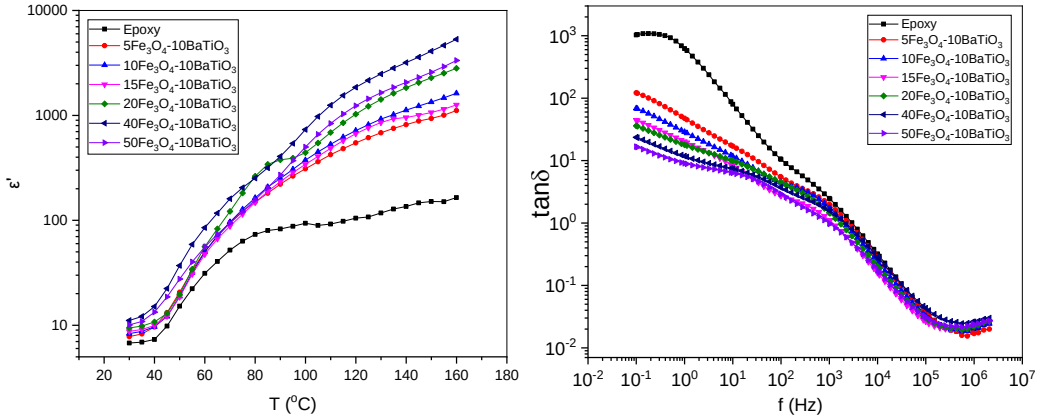

Fig. 1: Real part of dielectric permittivity (left) as a function of temperature at 0.1 Hz and loss tangent (right) as a function of frequency at 160°C for the epoxy/Fe_3O_4/$BaTiO_3$ set of systems.

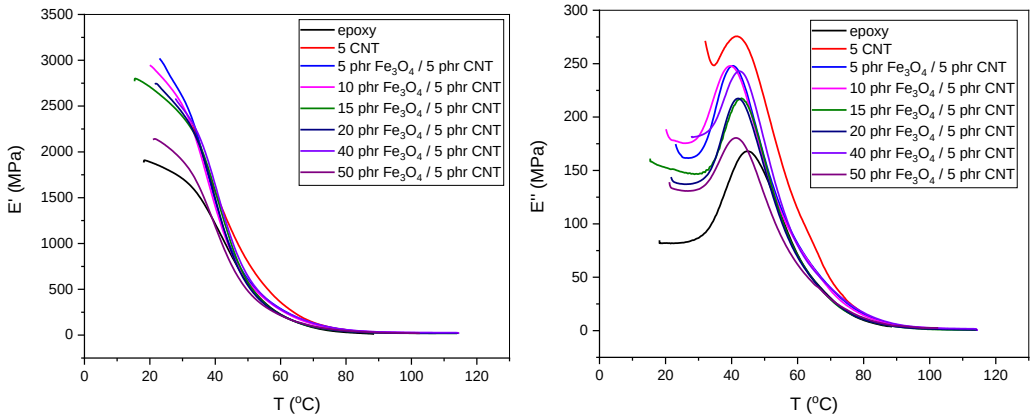

Fig. 2: Storage and loss modulus for the epoxy/Fe_3O_4/MWCNT set of systems.

Acknowledgments

The research work was supported by the Hellenic Foundation for Research and Innovation (H.F.R.I.) under the First Call for H.F.R.I. Research Projects to support Faculty members and Researchers and the procurement of high cost research equipment grant (Project Number: 2850).

[1] Multifunctionality of Polymer Composites (K. Friedrich, U. Breuer) Elsevier, 2015 (3-41).
[2] K. Song, J. Z. Guo, C. Liu, Polymer Based Multifunctional Nanocomposites and Their Applications, Elsevier, 2018.
[3] A. Sanida, S. G. Stavropoulos, Th. Speliotis, G. C. Psarras. Polymer, Evaluating the multifunctional performance of polymer matrix nanodielectrics incorporating magnetic nanoparticles: A comparative study, 236, 124311 (2021).
[4] S. Gioti, A. Sanida, G. N. Mathioudakis, A. C. Patsidis, Th. Speliotis, G. C. Psarras, Materials, Multitasking Performance of Fe_3O_4/$BaTiO_3$/Epoxy Resin Hybrid Nanocomposites, 15, 1784 (2022).

Temperature and Strain evaluation of screen-printed Ag and Carbon-based inks on flexible substrates

Aggelos Pilatis [1,2,*], Guillermo Enrique De la Cruz Karnavas [1], Frisela Skendaj [1], Dimitrios N. Pagonis [1, 2] and Grigoris Kaltsas [1]

[1] microSENSES Laboratory, Department of Electrical and Electronics Engineering, University of West Attica, Egaleo 122 41, Athens, Greece

[2] Department of Naval Architecture, University of West Attica, Egaleo 122 43, Athens, Greece

*apilatis@uniwa.gr

Nowadays the printed electronics technology attracts enormous interest from both the research and the industrial community as it offers the possibility of manufacturing cost-effective innovative devices on flexible substrates [1]. In the context of this work, the behavior of two of the most commonly used commercial ink types inks was studied in detail in relation to temperature and strain [2]. Specifically, the inks that were used in this work are the water based HPR-059 Carbon Black (Carbon content 10 wt%) and the HPS-FG77 Silver Nanoflake (Ag content 85 wt%) from Noavacentrix – USA. Line-shaped devices of different thicknesses were printed using a screen printing semi-automatic machine (Ever-bright, S-200HFC). For the thermoelectric characterization, a standard probe-station system was used in combination with a thermal camera (UNI-T, UNi690B), which was employed to remotely monitor the temperature of the samples. The characterization of the samples under tension was performed by a custom-made system which utilizes a high precision x-y motorized stages with integrated motor and controller system. The Ag-based devises were printed on three different substrates, namely HP premium plus Photo paper (280gr/m^2), Polyamide (PI) film (DuPont Kapton HN, thickness 125μm) and Polyethylene terephthalate film (Polyester, PET, thickness 125μm). In the case of Carbon-based ink, no stable structures could be obtained on glossy paper, thus the evaluation was performed on Kapton and PET substrates.

Fig. 1 presents the relative resistance change as a function of temperature for Ag-based ink structures with three different line-widths (1.0, 1.3 and 1.5mm) on the three different substrates. A positive TCR can be extracted in all the cases with mean values: 2.23×10^{-3}, 3.02×10^{-3}, 4.17×10^{-3} Ω/°C for paper, Kapton and PET substrates respectively. The corresponding evaluation for the Carbon-based ink on Kapton and PET substrates is illustrated in fig. 2, where samples with two different line-widths are indicated (1.3 and 1.5mm). The TCR in this case is negative and can be extracted as: -31.84 and -4.87 Ω/°C for Kapton and PET respectively. The Ag-based ink showed no significant change with strain. In particular, some insignificant changes were presented, that were not systematic and are essentially of no interest. On the contrary in the case of Carbon-based ink quite interesting results were found. Fig. 3 presents the relative resistance change as a function of tension (fig3a) - compression (fig.3b) distance for samples on Kapton with 1.0mm line-width. The graph indicates the response in three successive cycles (push and withdraw). It can be observed that the response in the first cycle is different for the others, which is a behavior that occurs in all samples. Fig. 4a,b presents the corresponding results in the case of PET substrate. A detailed discussion and analysis of all the experimental results will be carried out in the related paper.

References

[1] Jenny Wiklund et al., J. Manuf. Mater. Process., 5(3), 89 (2021).

[2] Tatiana Treputneva et al., MATEC Web of Conferences 143, 01015 (2018).

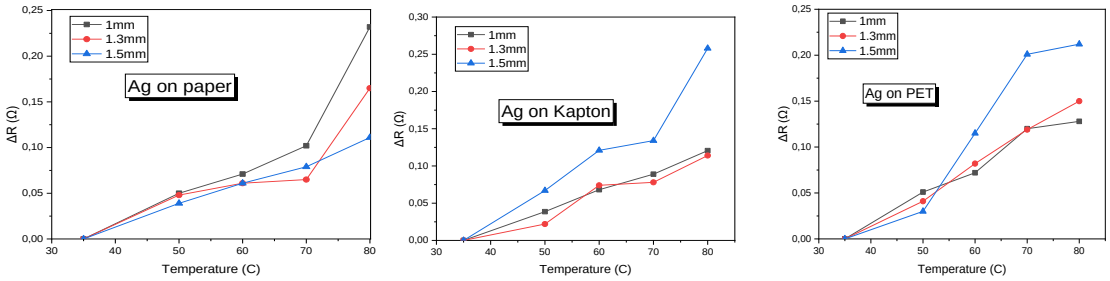

Figure 1: Relative resistance change as a function of temperature for Ag-based ink structures.

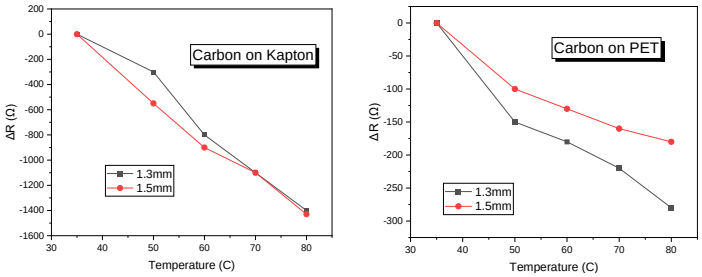

Figure 2: Relative resistance change as a function of temperature for Carbon-based ink structures.

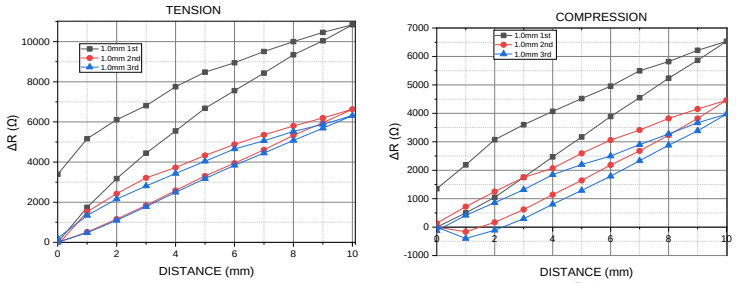

(a) **(b)**

Figure 3: Relative resistance change as a function of compression-tension distance for samples on Kapton

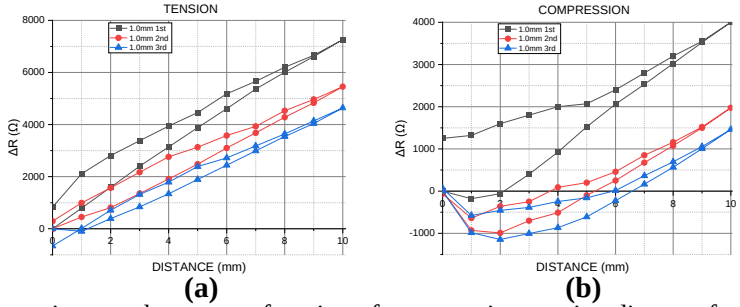

(a) **(b)**

Figure 4: Relative resistance change as a function of compression-tension distance for samples on PET

Multifunctional Performance of Hybrid Epoxy Resin/Ceramic Particles Nanodielectrics

S. Gioti[1], A. Sanida[1], G. C. Manika[1], G. N. Mathioudakis[2], N. Petropoulos[3], A. Kanapitsas[3], C. Tsonos[3] Th. Speliotis[4], A. C. Patsidis[1], and G. C. Psarras[1,*]

[1]Smart Materials &Nanodielectrics Laboratory, Department of Materials Science, School of Natural Sciences, University of Patras, Patras 26504, Greece

[2]Institute of Chemical Engineering Sciences (ICE-HT), Foundation for Research & Technology Hellas (FORTH), 26504 Patras, Greece

[3]Department of Physics, University of Thessaly, Lamia, Greece

[4]Institute of Nanoscience and Nanotechnology, NCSR "Demokritos", Athens 15310, Greece

*G.C.Psarras@upatras.gr

The scientific and technological impact of nanostructured and stimuli responsive materials is highly appreciated and recognised globally in our days. Nanodielectrics are insulating or semiconductive materials with grain size at the nanoscale level, or polymer matrix nanocomposites integrating filler with at least one dimension lower than 100 nm. Multifunctionality can be achieved when a material or a materials' system exhibit various desirable properties simultaneously, responding different external stimuli of loading conditions. In order to characterize a materials' system as multifunctional, its behaviour could include, mechanical durability, suitable thermal response and strength, corrosion resistance, adjustable polarization/dielectric permittivity and conductivity, stimuli induced phase changes, magnetic properties, and energy storing/retrieving ability[1-4].

Monolithic materials are not able to present, at the same time, many of the previously mentioned responses and typically are characterized by the numerical values of specific properties (i.e., mechanical strength, modulus of elasticity, permittivity, conductivity etc.). The subject of the present study targets to the development of a composite material/device being able to respond to various external stimuli or signal controls, having the versatility to execute functions and displaying the properties needed at service.

In the present study hybrid nanodielectrics consisting of an epoxy resin as the matrix, $BaTiO_3$ ferroelectric particles, and various magnetic nanoparticles (Fe_3O_4, or $ZnFe_2O_4$, or $SrFe12O_{19}$) were developed and studied under various loading conditions/external stimuli. All fabricated nanocomposites underwent morphological, structural, thermal, mechanical, dielectric, magnetic, and corrosive characterization. In addition, the ability of nanodielectrics to act as storing electrical energy devices was examined under dc conditions. Electrical energy was stored and then retrieved varying the charging field and the type and the amount of the employed filler. Ferroelectric particles provide functional performance via their thermally induced structural transition form the polar ferroelectric phase (tetragonal crystal lattice) to the non-polar paraelectric one (cubic crystal lattice)[4]. All the employed fillers are dielectric

materials and thus the real part of dielectric permittivity cab be adjusted by controlling the type and the content of the reinforcing phases. Dielectric relaxation phenomena related to the polymer matrix (glass to rubber transition, reorientation of polar side groups) and the filles (interfacial polarization, variable polarization of ferroelectric particles) were recorded and studied. The thermomechanical behaviour of the nanocomposites was improved, while the effect of environmental factors seems not to degrade their response. The presence of magnetic inclusions induces magnetic properties to the nanocomposites, which increase with magnetic filer content. With respect to the employed magnetic filler type, soft or hard magnetic response can be achieved. Finally, the examined systems are suitable for storing and recovering energy in a fast charge/discharge process.

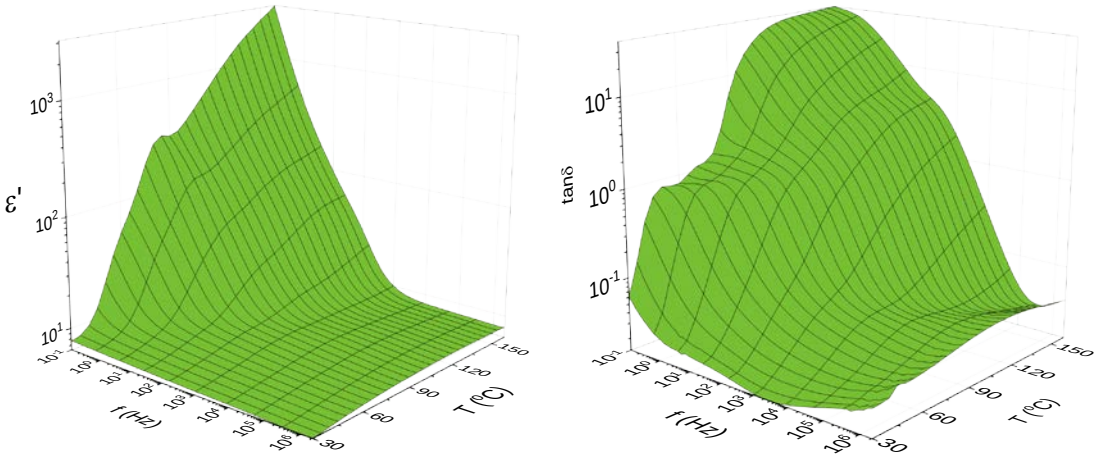

Fig. 1: Real part of dielectric permittivity (left) and dielectric loss tangent (right) as a function of frequency and temperature for the Epoxy/5 phr nano $SrFe_{12}O_{19}$/10 phr micro $BaTiO_3$ nanocomposite.

Obtained results and derived conclusions from the multiple characterization of the hybrid nanocomposites, indicate that the occurring physical mechanisms, synergistically construct the multifunctional performance of the systems.

Acknowledgments

The research work was supported by the Hellenic Foundation for Research and Innovation (H.F.R.I.) under the First Call for H.F.R.I. Research Projects to support Faculty members and Researchers and the procurement of high cost research equipment grant (Project Number: 2850).

[1] Multifunctionality of Polymer Composites (K. Friedrich, U. Breuer) Elsevier, 2015 (3-41).
[2] K. Song, J. Z. Guo, C. Liu, Polymer Based Multifunctional Nanocomposites and Their Applications, Elsevier, 2018.
[3] A. Sanida, S. G. Stavropoulos, Th. Speliotis, G. C. Psarras. Polymer, Evaluating the multifunctional performance of polymer matrix nanodielectrics incorporating magnetic nanoparticles: A comparative study, 236, 124311 (2021).
[4] S. Gioti, A. Sanida, G. N. Mathioudakis, A. C. Patsidis, Th. Speliotis, G. C. Psarras, Materials, Multitasking Performance of Fe_3O_4/$BaTiO_3$/Epoxy Resin Hybrid Nanocomposites, 15, 1784 (2022).

Multi Area Reflectance Spectroscopy biosensor: rapid & label-free determination of sepsis biomarkers at the Point-of-Care

D. Tsounidi[1], D. Goustouridis[2], V. Tsaousis[3], C. Mitropoulos[3], S. Kakabakos[1], P. Petrou[1], I. Raptis[2*]

[1] Immunoassay/Immunosensors Lab, INRASTES, NCSR "Demokritos", Aghia Paraskevi, 15341, Greece

[2] ThetaMetrisis S.A., Athens, 12132, Greece

[3] Medicon Hellas S.A., Gerakas, 15344, Greece

*raptis@thetametrisis.com

Sepsis is the most common cause of death in hospitalized patients worldwide, therefore, its early diagnosis is very important for effective treatment and increase of survival chances[1]. To this direction, the aim of this work is the fast and accurate determination of two biomarkers related to sepsis diagnosis, procalcitonin (PCT), and interleukine-6 (IL-6) at the Point-of-Care, by using an optical immunosensor based on Multi Area Reflectance Spectroscopy (MARS). MARS grounds on White Light Reflectance Spectroscopy (WLRS) detection principle that enables the label-free monitoring of biomolecular reactions by monitoring the shift of the interference spectrum created when white light is reflected by a Si chip with a SiO_2 layer on top [2]. In MARS, Si chips with multiple areas of SiO_2 of different thickness are used, each one modified with the specific antibody against each biomarker. These sensing areas are simultaneously illuminated, and the reflected interference spectrum is the combination of the spectra from the sensing areas, allowing the simultaneous monitoring of biomolecular reactions for the determination of the related biomarkers (Figure 1).

For the simultaneous determination of PCT and IL-6 a one-step immunoassay was developed according to which the immobilized onto each SiO_2 area antibody reacts with the biomarker molecules in the calibrators/samples in presence of a second biotinylated antibody followed by streptavidin as a signal enhancement step. The assays developed had detection limits of 2, and 0.01ng/mL for PCT, and IL-6, respectively. The assays were characterized by high reproducibility (the intra- and inter-assay coefficients of variation were less than 10% for both analytes) and accuracy (the percent recovery values ranged from 80 to 113%). For the sepsis diagnosis at the Point-of-Care, a bench-top automated bioanalytical device was developed encompassed all the necessary electronic and optical components for the performance of the assay along with a dedicated software. The analytical method developed was evaluated by analyzing human serum samples and the concentrations determined were compared with those obtained for the same samples by standard clinical laboratory methods, indicating a good agreement.

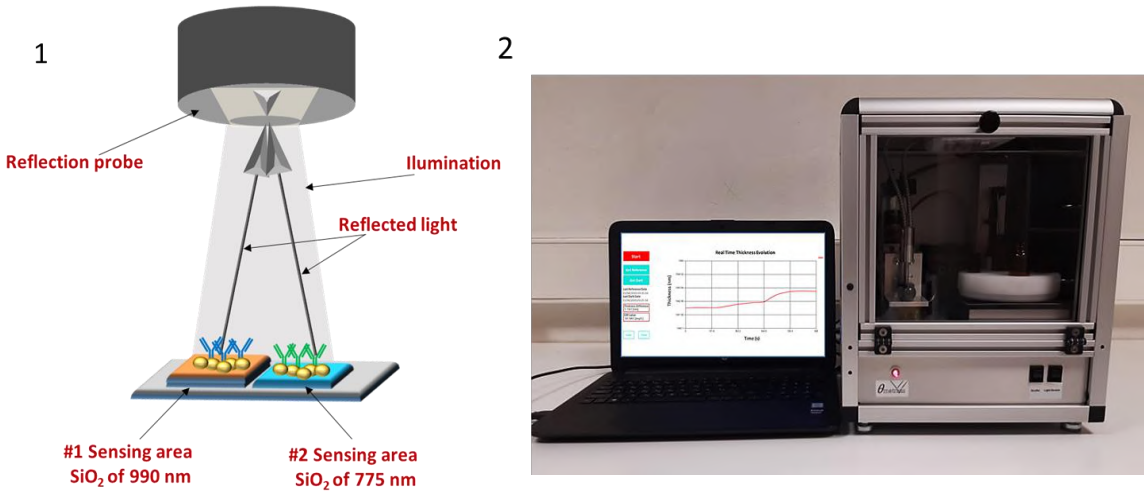

Fig. 1. Schematic of dual-analyte detection principle with the MARS set-up employing biochips with two SiO_2 sensing areas of different thickness. Fig.2. Image of the bioanalytical device employed for the development of the proposed immunosensor.

[1] M. Singer et al., JAMA, 315, 801-810 (2016).

[2] Anastasiadis et al., Biosens. Bioelectron. 153, 112035 (2020).

.

Holistic sensing platform based on InterDigitated Electrodes for the quantitative determination of concentration of VOCs

A. Botsialas[1], P. Oikonomou[1], M. Sanopoulou[1], I. Raptis[1*]

[1] Nanoelectronics, Photonics & Microsystems division, Institute of Nanoscience & Nanotechnology, NCSR "Demokritos", Aghia Paraskevi, 15341, Greece

*i.raptis@inn.demokritos.gr

InterDigitated Electrodes (IDEs) is a generic platform for a wide range of diverse applications with their implementation in sensing modules being a major one. In particular, IDEs coated with appropriately selected polymeric materials operate as capacitors (InterDigitated Capacitors, IDCs) and have found application as sensing elements for several substances either in the research field (e.g. Volatile Organic Compound) or as commercial products (e.g. humidity).

In the majority of IDCs, the interdigitated electrodes are equally spaced with width of a few micrometers. Very limited work is reported in the literature on IDCs with electrode width in the 1um or narrower range. However, as it has been shown in the literature that shrinkage of the electrode width (W (μm)) and the of gap between electrodes (G (μm)) to the sub-micron regime would result in higher sensitivities, i.e. at larger capacitance changes upon changes in their environment with the pronounced effect of improved limit of detection values.

In the present work we demonstrate the design, realization and evaluation of the IDE sensing platform for use in the detection of Volatile Organic Compounds (VOCs) in air and in the analysis of liquids. In particular, IDE arrays fabricated with conventional microelectronic processes on glass and Silicon substrates are coated with appropriate sensing layers for the detection of minute concentrations of certain analytes (VOCs) in the presence of humidity. In parallel, the same IDE devices after the deposition of appropriate passivation layers are evaluated as sensing devices of liquids through the real time monitoring of changes in the dielectric constant.

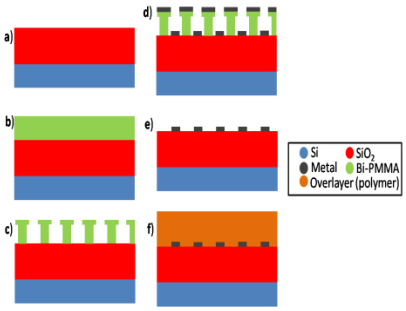

Figure 1. IDC fabrication flowchart. The processing steps are performed with standard microelectronic processes (see text)

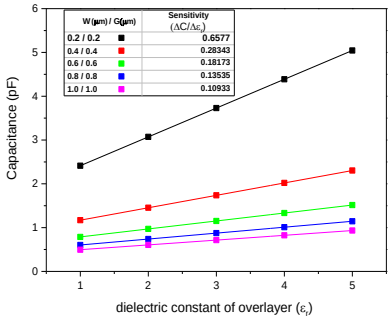

Figure 2: Simulation data for various IDEs layouts with 50nm aluminum thickness and 0.04mm^2 sensing area.

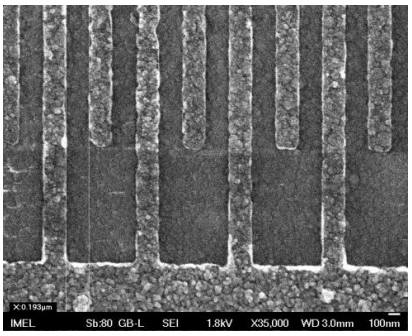

Figure 3. Top down SEM image of fabricated IDE on SiO_2 deposited by PECVD. Due to the deposition methods employed for both SiO_2 and Al the relevant material grains are visible.

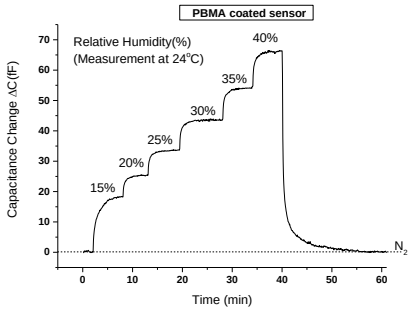

Figure 4. Dynamic measurement of a PBMA coated sensor of 200nm critical dimension, upon exposure to different levels of humidity.

References

[1] P.Oikonomou, A.Botsialas, A.Olziersky, E.P.Hadjigeorgiou, S.Katsikas, D.Dimas, G.Sotiropoulos, I.Raptis, M.Sanopoulou Sens. Act. B 237 509(2016).
[2] K.N. Chappanda, M.R. Tchalala, O. Shekhah, S.G. Surya, S.G.; M. Eddaoudi, KN Salama, Sensors 18 3898(2018).
[3] CJ Dias, R Igreja Sens. Act. A 256 95(2017)

.

Modification of Kapton surfaces with ZnO nanoparticles for triboelectric energy harvesting

A. Segkos, A. Bardakas and C. Tsamis*

NCSR "Demokritos", Institute of Nanoscience and Nanotechnology,

15310 Aghia Paraskevi, Athens, Greece

*c.tsamis@inn.demokritos.gr

Triboelectric generators have attracted considerable attention as a power supply for self-powered electronic devices and sensors due to their inexpensive fabrication processes, the vast variety of available materials and high-power output. Triboelectric energy harvesting, based on the contact electrification and electrostatic induction of two surfaces in relative motion, has emerged as a significant mechanism for converting mechanical energy to electrical energy. The triboelectric signal depends on material as well as surface properties. In this work we study the modification of triboelectric surfaces using zinc oxide nanoparticles (ZnO NPs) on Kapton® substrates for the development of flexible triboelectric generators (TENGs).

Sol-gels containing ZnO NPs were synthesized using zinc acetate dihydrate in ethanol absolute in various molarities under constant stirring and heating at 60 ºC for one hour. The sol-gels were left to age for 24 hours in ambient conditions before the deposition of multiple layers on Kapton® substrates by spin coating. A series of specimens was produced using different spin coating parameters (rpm, number of layers, thermal processing etc.) resulting in different surface roughness (Fig. 1).

Electrical characterization of the samples was performed in contact-separation mode (Fig. 2). As a reference surface two different electrodes were used for the triboelectric generator, corresponding to different electron affinities: a) PET/ITO film and b) commercially available Kapton® sheet. The output voltage was monitored as a function of time using an oscilloscope. In addition, charging experiments were performed through a rectifier bridge and capacitor (0.47μF) circuit (Fig. 3). The capacitor voltage was monitored using a Keithley 617 electrometer as a function of time when the triboelectric pair reached a steady-state Vp-p voltage.

The results demonstrate the effect of the different sol-gel compositions and deposition parameters on the output of flexible triboelectric generators, giving insight on the correlation of surface treatment and device performance as well as the design of TENGs with improved electrical performance.

Acknowledgment: This research has been co-financed by the European Union and Greek national funds through the Operational Program Competitiveness, Entrepreneurship and Innovation, under the call RESEARCH – CREATE – INNOVATE (EFOS, project code: T2EΔK-00350).

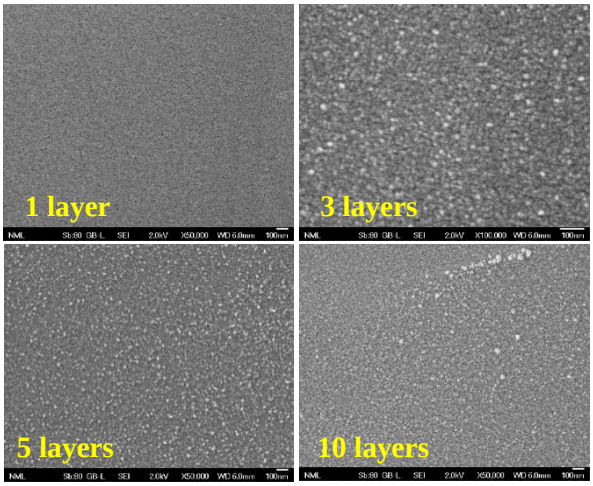

Figure 1: SEM images of ZnO modified Kapton.

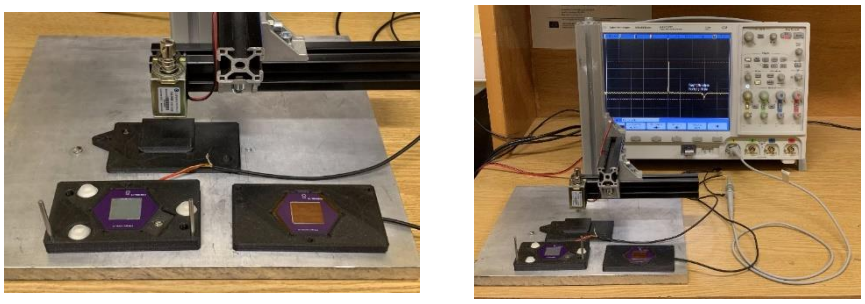

(a) **(b)**

Figure 2: a) Photograph of the triboelectric generator with Kapton® reference electrode and b) photograph of the experimental setup.

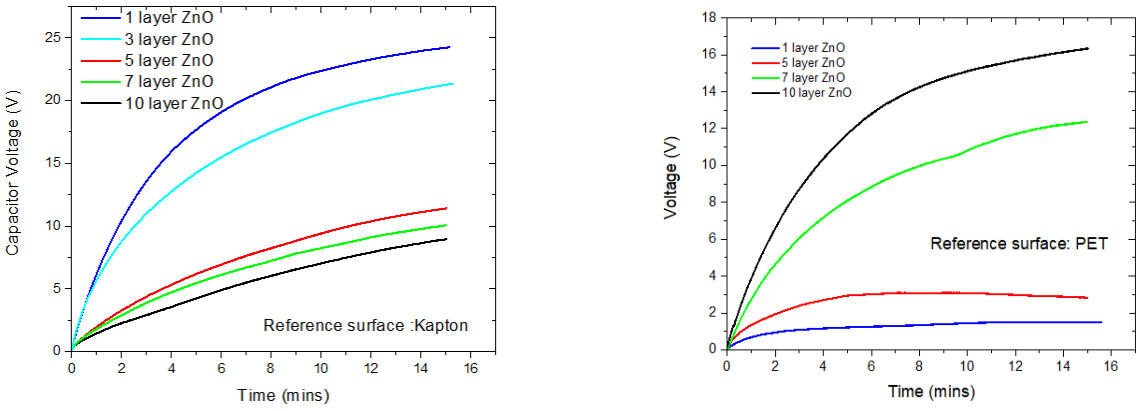

(a) **(b)**

Figure 3: Capacitor charging using a) Kapton® and b) PET as reference electrodes.

Towards a scale-enhanced microscopy enabled by Fourier Spectra Stitching method

Eleni Stai[1,2], Vassilios Constantoudis[1,3], Evangelos Cogolides[1,3] and Dimitris Nioras[1,2]

[1]Institute of Nanoscience and Nanotechnology, NCSR Demokritos, Agia Paraskevi, Attiki 15310, Greece

[2]Department of Physics, National and Kapodistrian University of Athens, Greece

[3]Nanometrisis p.c., Agia Paraskevi, Attiki 15310, Greece

*e.stai@inn.demokritos.gr

A great challenge in the characterisation of multiscale hierarchical surfaces is that the widely used Scanning Probe Microscopy (SPM) images for their inspection depict only a limited range of their morphology scales. In order to overcome this challenge, we propose a computational method based on the hybridization of SPM images obtained with different magnifications, i.e. pixel size and measurement range. The method generates scale-enhanced images containing the scales and frequencies of the images of both high and low magnifications, ranging from the higher resolution (smaller pixel size) to the larger measurement range of the input images. The key process of the method is the stitching of the Fourier Spectra of the input images with different resolution so that we get a wide-scale Fourier spectrum. By inverting the obtained wide-scale Fourier spectrum and randomizing their phases, we derive an artificial scale-enhanced image of the full-scale surface morphology. The so-called Fourier Spectra Stitching (FSS) method can be applied in all types of SPM images of surfaces with stochastic morphologies. A schematic representation of the flowchart of FSS method is illustrated in Fig.1.

In literature, image enhancement has been intensively studied with machine learning methods and also more conventional computational techniques based on interpolation models or Bayesian inference. Both of these approaches have resulted in resolution enhancement of a wide variety of images[2-3]. However, they suffer from the need of a large set of properly collected training data sets in the case of machine learning methods or the use approaches. The main concern of FSS method is to fit well to the existing practise of experimental researchers with no requirements for special and time consuming efforts for collecting and storing huge amounts of data. Furthermore, FSS method has been designed to be easily implemented and make its predictions in very short time. Finally, we should emphasize that FSS method is designed to be applied in images depicting stochastics morphologies which is the usual case in the majority of nanotechnology applications. Therefore, there is no need to reconstruct the true image on a pixel-by-pixel basis. The key idea is to generate an image statistically similar to the true one which is characterized by the true Fourier spectrum of amplitudes produced by the stitching of the input experimental images of different magnifications. The FSS method has been validated in synthetic surfaces with controlled roughness characteristics and then applied in a large variety of experimental cases with interesting results (see an example in Fig.2).

The next steps of our work will target to a) extend the method in all kind of surface morphologies including anisotropic patterns, b) explore the limitations of the method and seek for remedies and c) apply it in more experimental cases focusing on the morphologies of carbine films before and after plasma treatment.

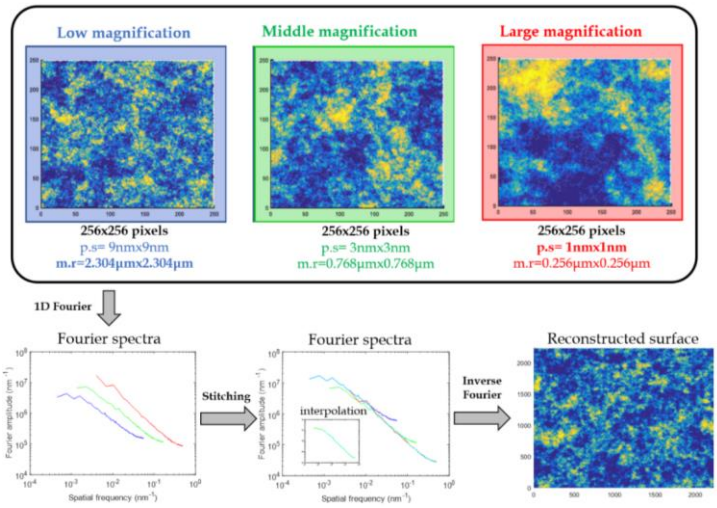

Fig.1 Graphical representation of the FSS method.

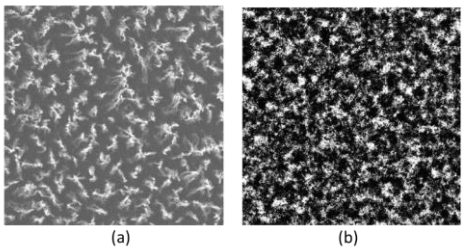

Fig.2 The real SEM image of low magnification (a) with pixel size =18.868nm and the reconstructed image (b) by FSS method with pixel size=4.695nm, i.e. with increased resolution by a factor 4. One can notice the successful reproduction of density and size of features on one side and on the other the failure to capture the fine details of nanofilament bundle shapes.

References

(1) Stai, E.; Nioras, D.; Gogolides, E.;Contantoudis, V. "Hybridization of Scanning Probe Microscope measurements of multiscale surfaces with different resolution: Fourier Spectra Stitching" (in preparation)

(2) Qian, Y.; Xu, J.; Drummy, L. F.; Ding, Y. Effective Super-Resolution Method for Paired Electron Microscopic Images. *IEEE Trans. Image Process.* **2019**, *29*, 7317–7330. https://doi.org/10.1109/TIP.2020.3000964.

Acknowledgement

This work has been funded by the ERANET Project 'Carbyne Films: Synthesis of a New Class of Carbon Allotrope and Novel Applications in Sensors and Biosensors (CarbyneSense)', MIS 5161208.

Με τη συγχρηματοδότηση της Ελλάδας και της Ευρωπαϊκής Ένωσης

The Effect of Temperature on Single Electron Transistor

P. Papadopoulou[1], E. Philippousi[1], M. Hanias[1], K. Ovaliadis[1], L. Magafas[1], D. Tassis[2*] and S.G. Stavrinides[1]

[1]International Hellenic University, Physics Department, St. Loucas Campus, Kavala, Greece

[2]Aristotle University of Thessaloniki, Physics Department, Thessaloniki, Greece

*dtassis@auth.gr

Single Electron Transistor (SET) is a promising nanodevice, expected to demonstrate a high switching speed at room temperature, allowing for its utilization as a RAM with ultra-low power consumption[1]. It may be considered as a FET having a limited conducting region of low capacitance, due to source-drain coupling through tunnel junctions; the capacitive coupling to the gate is controlling the single electron transfer mechanism. The fundamental physical principle driving the operation of SET is the tunnelling effect through a Coulomb blockade[2], which controls the number of electrons in a small quantum dot within the channel, further allowing for the demonstration of I-V characteristics clearly exhibiting a Negative Differential Region (NDR) [3]. In this brief, simulations of a typical SET operation based on semi-classical models and depicted on the demonstrated I-V characteristics, are utilized for investigating the influence of temperature on SET's operation, focusing on the effect of the emergence of a NDR.

For simplicity we consider that our SET consists of a semiconducting channel separated by an insulator layer, while the metallic gate surrounds the channel. A positive gate voltage V_G lowers the energy levels in the channel, rendering it as an n- type channel, while when a negative gate voltage is applied the channel becomes a p- type one. The mathematical equations describing the SET's characteristic curves have been derived[4] and briefly are:

the total potential energy: $$U = \frac{C_G}{C_E}(-qV_G) + \frac{C_D}{C_E}(-qV_D) + \frac{q^2}{C_E}\Delta N \quad (1)$$

chanel broadening due to coupling: $$D_\varepsilon(E) = 2\frac{\frac{\gamma}{2\pi}}{(E-\varepsilon)^2+\left(\frac{\gamma}{2}\right)^2} \quad (2)$$

and the current through the SET: $$I = \frac{q}{\hbar}\int_{-\infty}^{+\infty} D_\varepsilon(E-U)\frac{\gamma_1\gamma_2}{\gamma_1+\gamma_2}[f_1(E) - f_2(E)]dE \quad (3)$$

We assume that q^2/C_E=0.25eV, γ_1= γ_2=0.005eV, ε=0.2eV, V_G=0V, k_BT =0.0025eV and C_D/C_E =0.5. Studying the electrical behavior of the SET we consider that μ_1=-0.2eV, $C_G=2K_e\varepsilon_0WL/t$, $C_S=C_D=0.05C_G$, W=1μm, L=10 nm, insulator thickness t=1.5nm[5], where K_e=4.

Focusing on investigating the influence of temperature T in SET's electrical behavior. In specific the I_D-V_{DS} characteristic curve is presented in Fig.1(a), for V_G=0. As illustrated in this figure, the I_D-V_{DS} curves demonstrate a very clear negative differential resistance (NDR) region. This effect is due to the enhancement of one of the two tunnelling barriers of the transistor by the source-drain electric field. What is important is that the value of V_{DS} for which the NDR region emerges can be controlled by the temperature; as the temperature increases NDR threshold (V_{DS} value) decreases, while the value of current' s peak also increases. In Fig. 1(b), zoom-in on the characteristics for temperature values (100K, 300K, 400K), are presented

clearly depicting the described behavior.

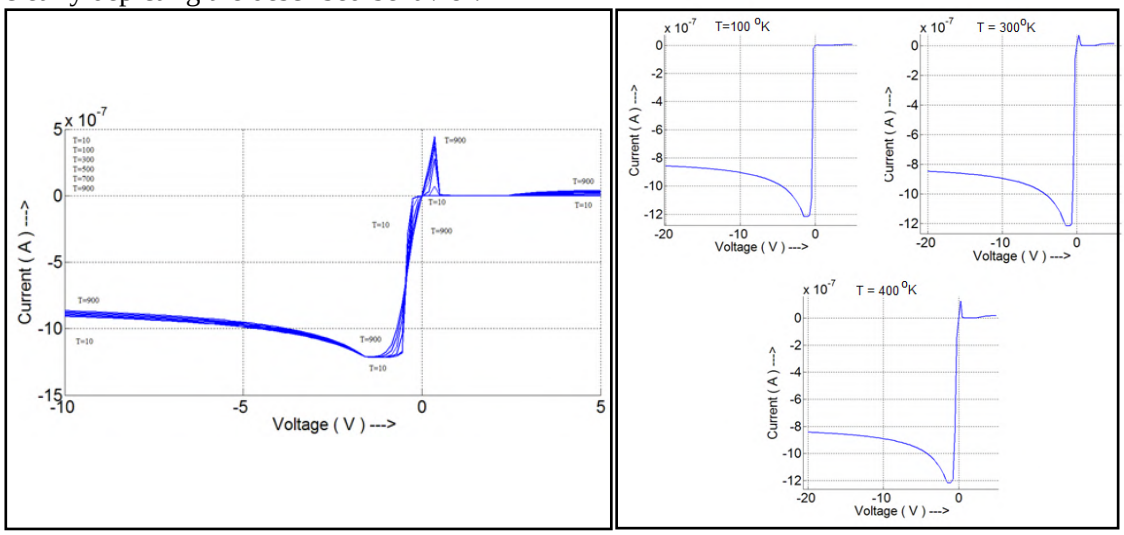

(a) (b)

Fig. 1. (a) The effect of temperature on SET's electrical behavior. The emergence of a NDR is evident. (b) Zoom-in the NDR region for three different temperatures i.e., 100K, 300K, 400K.

The described effect of temperature agrees with other model simulations, such as the Fermi Golden Rule[6]. Keeping the temperature T constant equal to 0.025K. i.e., almost zero, and by changing V_G, we observe that as it increases from 0V to 10V the NDR region disappears, while current begins to increase, for higher V_{DS} (Fig. 2(a) and (b)). Apparently for negative values of V_G the NDR region gradually disappears, and the I_D-V_{DS} curves become the typical ones for a symmetric SET junction (Fig. 2(c) and (d)).

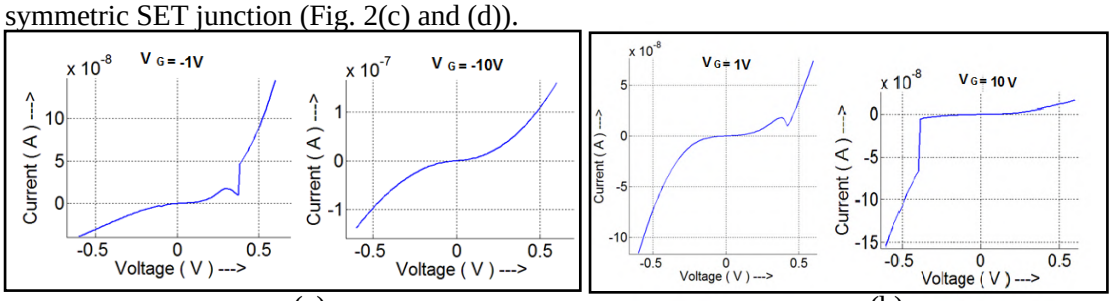

(a) (b)

Fig. 2. Disappearance of the NDR region, in the case of (a) positive V_G and (b) negative V_G.

Since SET operation involves pure quantum processes that cannot be adequately described by classical models, the semi-classical approach followed in this brief, which involves broadening functions and Landauer's formula, describes the NDR effect due external parameters like temperature. Finally, the important result is that with proper choice of parameters SET can operate as a NDR, a typical on–off transistor or a simple resistor.

[1] A.Touati,S. Chatbouri and K. Adel, Nanotechnology 1 (2013).
[2] H.V. Khadem et al., J. of Nanoelectronics and Optoelectronics, Vol (13-1), 138 (2018).
[3] B. Sui,L. Fang, Y. Chi, C. Zhang, IET CircuitsDevices Syst., **Vol** (4-5), 425 (2010).
[4] S. Datta, Nanotechnology, 15S433-S451, (2004).
[5] B.Sui,X. Chen,L.Fang, International Conference on Systems and Informatics,(2012)
[6] A.Deyasi, A.Sarkar, Microsystem Technologies,1(2018).

TCAD simulation of TIPS-Pentacene:PS OFETs

Tryfon Kaimakamis[1,*], Matthias Bucher[2] and Dimitrios Tassis[1]

[1]Aristotle University of Thessaloniki, School of Physics, 54124, Thessaloniki, Greece

[2]Technical university of Crete, School of Electrical and Computer Engineering, 73100, Chania, Greece

*tkaimaka@physics.auth.gr

In this study we initially investigated the variability of similar experimental TIPS-Pentacene:PS OFETs by comparing the input characteristics from a batch of devices with the same channel length (L), as can be seen in Fig.1. Specifically, Fig.1a refers to a bottom-gate top-contact (BG-TC) OFETs with a channel length of 30 μm. An effective low field mobility variation was found in the range from 0.22-1.12 cm^2/Vs and has been discussed in a previous work[1]. It is important to note here that, the capacitance density (C in nF/cm^2) variation also affected the effective low field mobility extracted values. Additionally, the subthreshold slope (SS) and the I_{ON}/I_{OFF} values changed from 7.69 to 3.38 V/dec and from 4.22×10^3 to 6.59×10^5, respectively. An effective low field mobility variation from 0.39-1.10cm^2/Vs was also observed in Fig.1b, indicating that it is not only limited to the TIPS-Pentacene:PS OFETs having 30μm channel lengths. In the same figure a variation of the SS electrical parameter is also apparent with its value ranging from 4.0 to 2.73 V/dec. Consequently, to simulate similar experimental TIPS-Pentacene:PS OFETs we need to specify for each experimental device new simulation parameters (such as mobility parameters, interface charges, interface and/or bulk traps) due to the inherent variability.

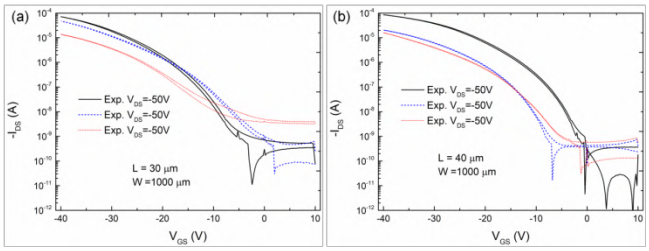

Fig.1. Variability of input characteristics (I_{DS}-V_{GS}) of similar OFETs with (a) 30 μm and (b) 40μm channel length.

Further, to simulate with a TCAD tool (Silvaco-Atlas) the experimental TIPS-Pentacene:PS blend OFETs we took into account the physical quantities concerning the interface charges as well as the shallow donor-like interface and bulk traps density of states (DOS). The physical models we used included the constant low-field mobility model and the band-to-band tunneling model. To obtain more realistic simulations we also included another important physical parameter, such as the interface roughness which has a great impact on the OFET's electrical performance. We introduced the roughness at the active interface through inserting different patterns (square, sinusoidal, trapezoidal). By keeping constant the amplitude

[1]T. Kaimakamis, RSC. Adv., 6, 97077-97083(2016)

(A=1.25nm) and the number of periods (9) of the different patterns we studied their impact on the I_{DS}-V_{GS} characteristics (Fig.2). The ON current was mainly affected showing a reduction from 1.44×10^{-5} A to 1.33×10^{-5} A and 1.02×10^{-5} A with the pattern alteration from square (Fig.2a) to sinusoidal (Fig.2b) and trapezoidal (Fig.2c). In Fig.3 the comparison between the simulated input (Fig.3a) and output (Fig.3b) characterisitcs and the xperimental data revealed a significantly improved match when a square wave pattern (RMS=1.25 nm, periods=9) is

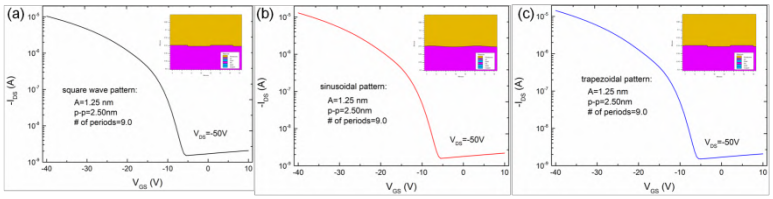

Fig.2. I_{DS}-V_{GS}s with a (a) square, (b) sinusoidal and (c) trapezoidal pattern at the active interface.

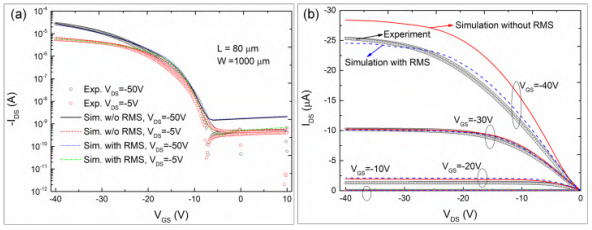

Fig.3. Comparison between the simulated (with and without RMS) and the experimental I-Vs.

considered at the active interface. We also considered the TIPS-Pentacene thickness non-uniformity (as revealed by AFM). The simulation results indicated that the non-uniformity has the most dramatic impact on the I_{DS}-V_{DS} characteristic when the local thickness near the drain side is smaller (Fig.4a) in respect to the mean thickness of 80 nm. An obvious degradation of the drain current is also observed in Fig.4b when the local thickness near the drain side is decreased down to 10 nm.

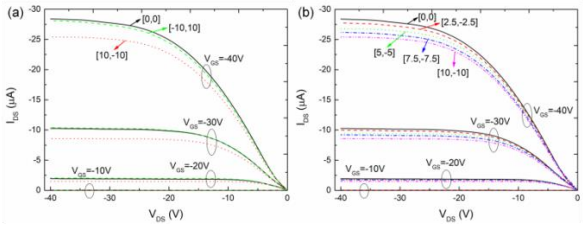

Fig.4. TIPS-Pentacene non-uniformity effect on I_{DS}-V_{DS} (a). Local thickness effect on I_{DS}-V_{DS} (b). The two numbers in brackets indicate local thickness difference in source and drain side.

Finally, by comparing the ideal device with the "all inclusive" one, a severe degradation of the I_{DS} is observed in Fig.5b. The I_{ON} was reduced from 2.87 (ideal)–2.23×10^{-5} A (all inclusive) at V_{DS}=-50V and from 7.01 (ideal)–5.29×10^{-6} A (all inclusive) at V_{DS}=-5V (Fig.5a).

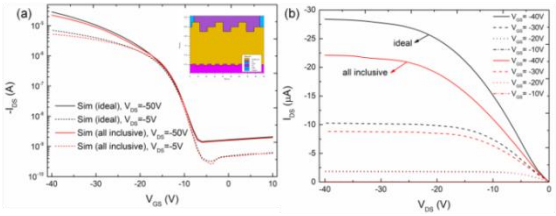

Fig.5. Comparison between "the all inclusive" (roughness and non-uniformity) and the ideal devices.

Behavior of InGaAs MOSFET short channel effects down to deep cryogenic conditions

Francesco Serra di Santa Maria[1], Cezar Zota[2], Eunjung Cha[2], Gerard Ghibaudo[1], Christoforos Theodorou[1,*]

[1]Univ. Grenoble Alpes, Univ. Savoie Mont Blanc, CNRS, Grenoble INP, IMEP-LAHC, Grenoble, 38000, France

[2]IBM Research GmbH Zürich Laboratory, Säumerstrasse 4, CH-8803 Rüschlikon, Switzerland

*christoforos.theodorou@grenoble-inp.fr

In order for quantum computers to function properly, the readout electronics in direct communication with the qubits[1] need to operate at a few Kelvins. A very attractive device candidate for this type of circuits is the III-V channel MOSFET, thanks to its high ON current and transconductance[2]. However the short channel effects may jeopardize the circuit performance when downscaling the gate length. In this work we present an investigation of effects like the roll-off of threshold voltage, V_t, the drain-induced V_t shift (DITS), as well as the dependence of channel mobility, μ_0, and subthreshold swing, SW, with length, from T = 300 K down to 10 K. The devices under study were fabricated by IBM Zurich[3], utilizing an InGaAs channel of 20 nm thickness on a SiO_2 buried oxide. The gate width is W = 1 μm and the channel lengths range from L = 300 down to 10 nm. We performed the measurements using a HP 4155A analyser and a 200mm cryostation. For the extraction of V_t and μ_0, we used the well-established Y-function[4], $Y=I_d/\sqrt{g_m}$, which suppresses any first order degradation effect like the series resistance.

Fig. 1 shows two examples of input characteristics in linear region for L = 300 nm and L = 50 nm, from where we can already observe certain peculiarities: the threshold voltage seems to stabilize below 200 K, whereas the sub-threshold swing continues improving down to 10 K. A knee is also visible around V_g = 0.2 V, which we have previously attributed to the onset of L valley conduction[5]. In saturation region (Fig. 2), the input characteristics seem to almost superpose in strong inversion, with a huge improvement of gate leakage at 50 and 10 K.

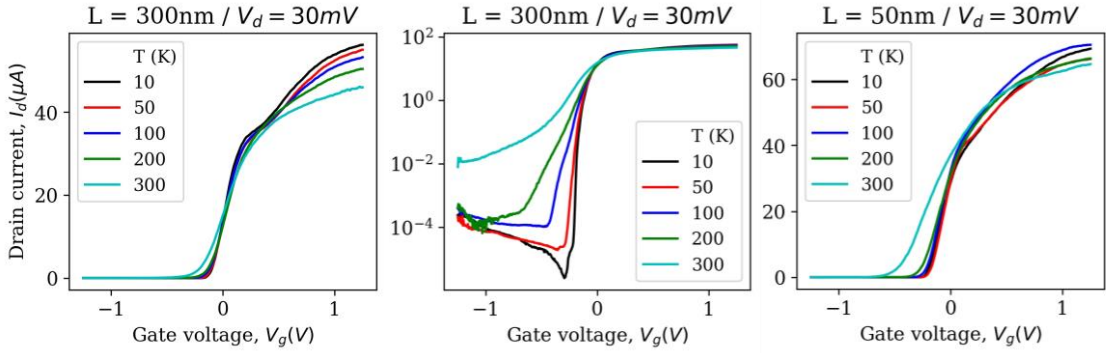

Fig. 1. Measured drain current versus gate voltage in linear region (V_d = 30 mV) for gate length L = 300 nm (left and center) and L = 50 nm (right) and temperatures ranging from 300 K down to 10 K

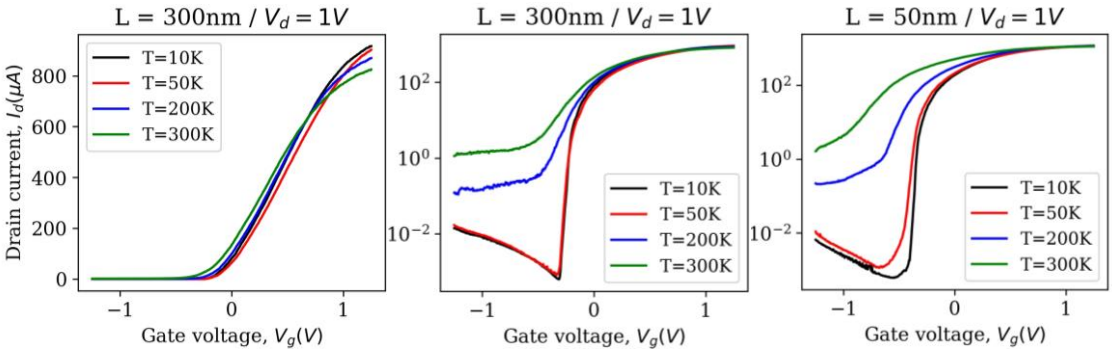

Fig. 2. Measured drain current versus gate voltage in saturation region (V_d = 1 V) for gate length L = 300 nm (left and center) and L = 50 nm (right) and temperatures ranging from 300 K down to 10 K

Concerning V_t (Fig. 3), it is found to roll-off at short channels significantly at 300 K, but to be almost constant from L = 100 nm down to 10 nm at lower temperatures. The DITS ($V_{t,lin}$-$V_{t,sat}$) is surprisingly improving at lower temperatures, becoming independent of L at 10 K. SW (Fig. 4) seems L-independent at all T, while reaching impressive values close to 10mV/dec at 10 K, however μ_0 appears to be much more dependent on L than T, revealing important scattering occurring near the source/drain regions.

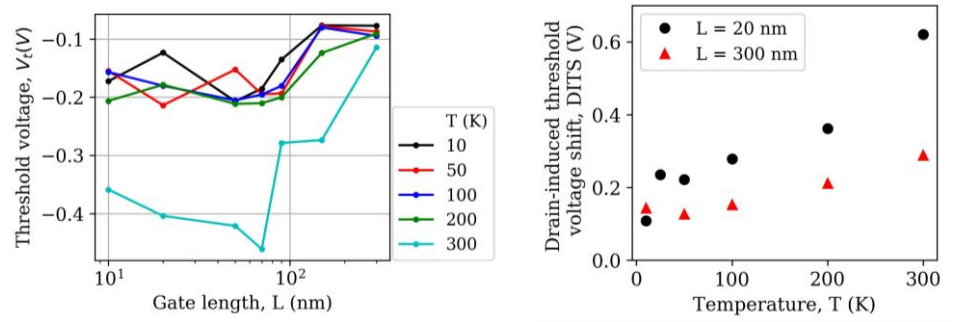

Fig. 3. Extracted threshold voltage versus gate length for T ranging from 300 K down to 10 K (left) and drain-induced threshold voltage shift versus temperature for long and short device (right)

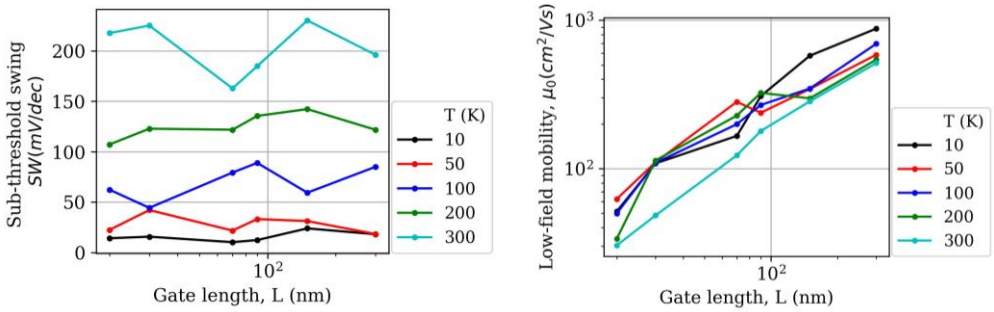

Fig. 4. Extracted sub-threshold swing (left) and low-field mobility (right) in linear region (V_d = 30 mV) versus gate length, for temperatures ranging from 300 K down to 10 K

Acknowledgement: This work was supported by the European Union H2020 program SEQUENCE (Grant – 871764).

[1]J.M. Hornibrook et al., Phys. Rev. Applied, 3, 024010 (2015)
[2]C. Convertino et al, 2018 IEEE IEDM, p. 39.2.1-39.2.4
[3]C. Zota, C. Convertino, D. Caimi, M. Sousa, L. Czornomaz, Proceedings of EUROSOI-ULIS (2019)
[4]G. Ghibaudo, Electronics Letters, Volume 24, Issue 9, 28 April 1988, p. 543 – 545
[5]Francesco Serra di Santa Maria, Proceedings of ESSDERC/ESSIRC (2022), p. 257 – 260

THE EFFECT OF BENDING OF HUMIDITY FLEXIBLE SENSORS FABRICATED WITH GRAPHENE OXIDE AND ZIF-8

Theodoros Tsapekos and Filippos Farmakis

Micro- and Nano-Technology Lab, Electrical Engineering and Computer Engineering dept., Democritus University of Thrace, Vas. Sofias 12, 67100, Xanthi, Greece.

theotsap1@ee.duth.gr

Introduction

Humidity sensors have attracted increasing attention due to their widely application in numerous fields such as industry, medicine, agriculture, environmental monitoring[1] and general domestic use. Over the years, many different types of humidity sensors have been proposed, utilizing several sensing materials, yet the research for low-cost and high functional ones is an ongoing procedure. Recently, graphene has aroused significant interest for various gas sensing applications due to its large specific area for molecular adsorption and high carrier mobility[2]. In a previous work, the enhancement of the humidity sensing properties of graphene oxide was demonstrated with the addition of a metal organic framework nanomaterial Zeolitic imidazolate framework (ZIF-8)[3]. In this work we fabricate and compare graphene oxide-based humidity sensors that are deposited on a flexible polyethylene terephthalate (PET) substrate, with the addition of ZIF-8, serving as an extra sensing layer.

Experimental

Two types of sensors were fabricated using drop casting of graphene oxide (GO) diluted in DI water with 2.5 mg/mL of concentration (GO sensors), followed by drop casting ZIF-8 (GO/ZIF-8 sensors). After the drop casting processes, the sensors were dried on a hot plate at 60^{o}C for 1 hour. Devices were defined by a shadow mask and the electrical contacts were grown by DC sputtering. Electrical measurements were carried out in a humidity chamber, where we could adjust the humidity levels by combining humidified air and nitrogen gas under controlled temperature. Finally, the devices were characterized under bending conditions.

Experimental results

Figure 1 shows that the fabricated humidity GO sensors exhibit more than 5 decades of resistance change within 0 and 70% of relative humidity (RH) that has already been attributed to the strong ionic transport mechanisms and the related oxygen groups of GO[3] . It can be also observed that the sensor bending provokes an irreversible change to the electrical characteristics of the sensor, since the resistance vs relative humidity remains unchanged performing 50 degrees bending. In addition, for the same RH values, sensor resistance increases after the first bending. In the case of GO/ZIF-8 sensor (Figure 2), the effect of the sensor bending to the resistance is not pronounced especially for RH values higher than 25%. Indeed GO/ZIF-8 sensor exhibited the exact same response in resistance change from medium to high levels of RH (30%-70% RH) while flat and bended 30 and 50 degrees. A slight increase in

resistance is observed when the sensor was measured at flat mode for medium to high RH (35%-70% RH).

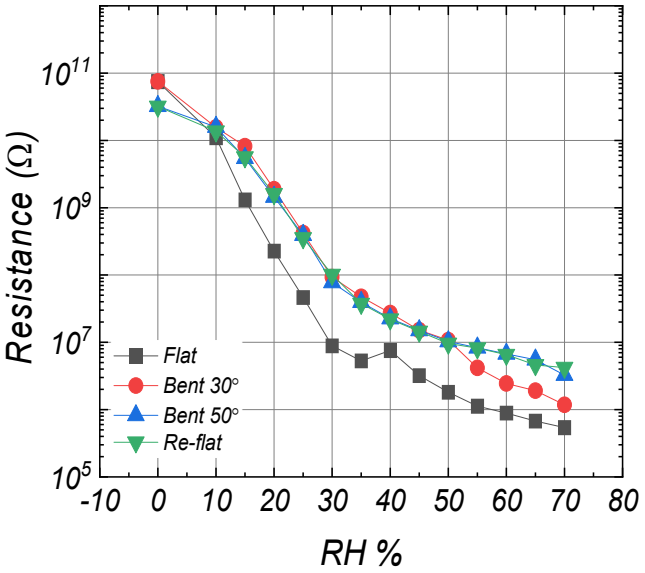

Figure 1 Resistance vs relative humidity for plain GO sensor

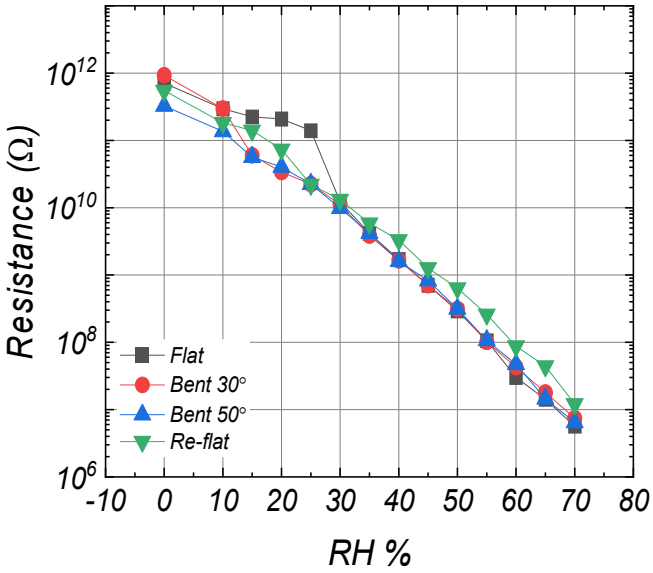

Figure 2 Resistance vs relative humidity for GO/ZIF-8 0.8% w/v sensor

Conclusions

In this work, we demonstrate that bending a graphene oxide-based humidity sensor fabricated on a PET substrate is an irreversible procedure. Both GO and GO/ZIF-8 sensors exhibit high resistance change (more than 5 decades) over a wide range of relative humidity levels (0% to 70% RH). An increase in the resistance of the plain GO sensor can be observed after the first bending. The GO/ZIF-8 sensor shows no pronounced change in the resistance under bending conditions, particularly when the RH levels are 25% or above.

REFERENCES:

[1] Dongzhi Zhang, Jun Tong, Bokai Xia, Qingzhong Xue, Ultrahigh performance humidity sensor based on layer-by-layer self-assembly of graphene oxide/polyelectrolyte nanocomposite film, Sensors and Actuators B 203 (2014) 263-270

[2] Dongzhi Zhang, Jun Tong, Bokai Xia, Sensors and Actuators B 197 (2014) 66-72 https://doi.org/10.1016/j.snb.2014.02.078.

[3] G. Zardalidis, M. K. Daletou and F. Farmakis, "Enhanced Proton Conduction of Graphene Oxide by the Addition of ZIF-8 for Room Temperature Relative Humidity Sensors," in *IEEE Sensors Journal*, vol. 21, no. 24, pp. 27290-27297, 15 Dec.15, 2021, doi: 10.1109/JSEN.2021.3126377

Pulse-stream impact on recognition accuracy and power consumption of reservoir computing from SiO_2-based memory devices

Charalampos Tsioustas*, Panagiotis Bousoulas, George Klitsiotis and Dimitris Tsoukalas

Department of Applied Physics, National Technical University of Athens, Athens, 15780, Greece

*charalampos_tsioustas@mail.ntua.gr

During the last decade memristive devices proved to be a potential candidate for developing novel memory devices[1], due to their small footprint, especially when they are developed in the form of crossbar architecture structures (CBA). At the same time, they have low energy requirements and they are capable of replicating the computational capacity of biological synapses and develop complex artificial neural networks (ANNs)[2]. Among the various ANNs, recurrent neural networks (RNNs) dominate in terms of temporal processing of input signals and by extension can export features with the corresponding sequential information. Reservoir computing (RC) belongs to the RNNs family and can transform input data into a higher spatiotemporal dimensional space via the non-linear reservoir block. The reservoir block utilizes the short-term memory (STM) properties of the memristor without the requirement of training, thus only the CBA of the final readout layer requires training, consisting of non-volatile memristors.

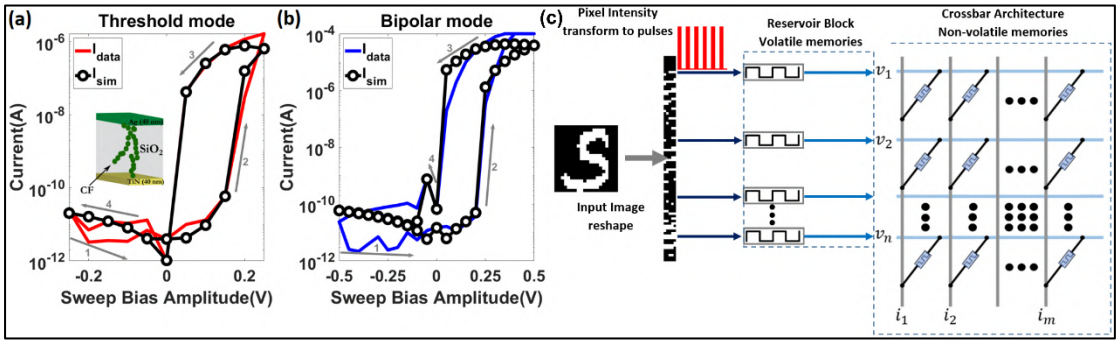

Fig. 1:(a) Threshold mode (volatile switching), (b) Bipolar mode (non-volatile switching), (c) RC system for the supervised learning of digits 0-9 for the case of 5-bit pulse-stream.

The developed memristive devices participating in the RC system have the ability to behave in dual mode. Initially, they present volatile behaviour (Fig. 1(a)), and under the application of a higher external voltage, a transition to non-volatile switching is observed (Fig. 1(b)). The self-selective devices operate below 0.5 Volt and do not require the use of external switches, such as transistors, thus reducing complexity and energy requirements. Furthermore, a self-selective

simulation model was developed and in order to evaluate the RC system's performance[3], the following neuromorphic application was designed (Fig. 1(c)). The application accepts as input the pixels' intensity of binary images with sizes 21x20 pixels, containing the information of handwritten digits from the MNIST dataset. Each image is reshaped and every row of the new image is transformed into a pulse-stream according to the state of each pixel (black or white). The reshaping process depends on the chosen pulse-stream; thus the reshaped image's sizes are (420/pulse-stream)xpulse-stream.

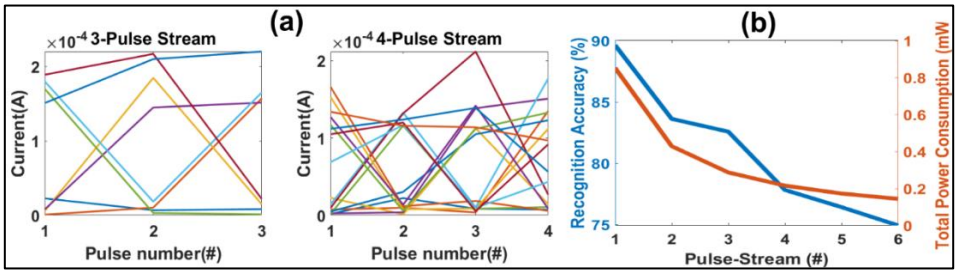

Fig. 2: (a) AC analysis of the volatile devices in the reservoir for the case of pulse-stream 3 and 4. (b) Pulse-stream impact on recognition accuracy and total power consumption.

The purpose of this neuromorphic application is to study the impact of the pulse-stream on the recognition accuracy as well as on the RC system power consumption. For this reason, the results of the corresponding AC analysis on the STM are shown in Fig. 2(a), where the applied square pulse series has 0.1 V pulse amplitude, 100ns pulse duration and 100 ns delay. The experimental values are taken 100 ns after the pulse duration. The results indicate that the devices have taken different distinct conductance levels. This is very important, as these conductance values will be exploited by the final readout layer and it is desirable that each final conductance level corresponds to a different coding of the input image intensity[4]. The impact of choosing the appropriate pulse stream can be seen in Fig. 2(b). Although, the pulse-stream increase is equivalent to the reduction of the total power consumption in the system of 0.84 mW, as the number of the required volatile memories and synapses are lessened, it has the disadvantage that the recognition accuracy is diminished from 89.63% to 74.94%. Specifically, for the case of a 3-bit pulse-stream the RC system has a recognition accuracy of 82.58% over the test set. Training required a total of ten epochs, while the 50.000 training images were organized into 10.000 training batches per epoch.

The authors acknowledge support of this work by the Hellenic Foundation for Research and Innovation (H.F.R.I.) under the "First Call for H.F.R.I. Research Projects to support Faculty members and Researchers and the procurement of high-cost research equipment grant" (Project Number: 3830).

1. P. Bousoulas, et al., Nanotechnology, 31 (2020).
2. P. Bousoulas, et al., IEEE Transactions on Electron Devices, 69, 2360-2376 (2022).
3. C. Tsioustas, IEEE Transaction on Nanotechnology (2022).
4. D. Chao, et al., Nature Communications, 8, 2204 (2017).

A Microfluidic System for Biomedical Applications

T. Koutsis[1*], P. Tzani-Tzanopoulou[2], S. Taka[2], N. G. Papadopoulos[2], G. Kaltsas[1]

[1]microSENSES Laboratory, Department of Electrical and Electronic Engineering, University of West Attica, Athens, 12243, Greece,
[2] Second Pediatric Clinic, National and Kapodistrian University of Athens, Greece

*t.koutsis@uniwa.gr

This work presents a microfluidic system for biomedical applications. The system can provide continuous nutrition flow to cultured epithelial cells on **T**ranswell **I**nserts (TI), simulating the real-world conditions. Additionally, the system has embedded electrodes that allow for **T**rans**E**pithelial **E**lectrical **R**esistance (TEER) and **I**mpedance **S**pectroscopy (IS) measurements to be conducted [1].

The microfluidic system is made of **P**oly**C**arbonate (PC) material making the system robust, reusable, and low cost for various cell culture experiments. The PC is machined with a high-precision CNC ColinBus Laboflex. The system consists of two parts namely, the base and the cover. The base incorporates, the microfluidic channels, the nutrition compartment and one of the two Ag AgCl electrodes needed for TEER measurement, facing the lower side of the membrane of the TI, Fig. 1d. The other electrode needed for the TEER measurement, was placed manually to the upper side of the of membrane of the TI, Fig. 1c. The inlet channel dimensions are 1.5mm (W) and 1mm (H) and the widest/narrowest point of the outlet channel are 5.1mm/1.5mm respectively, having the same depth as the inlet. The design of the outlet channel exhibits low resistance to air bubbles that were formed during the flow cycle. The nutrition compartment's dimensions are 16mm (D) and 2mm (H). The cover incorporates a hole and an O-Ring where the TI is placed to ensure that there is no leakage when nutrition flows. Furthermore, the base and the cover are secured together via screws, to form the final microfluidic system and a second O-Ring along the whole perimeter of the flow cycle is installed to prevent any leakage between them. The dimensions of the assembled microfluidic system are 75mm (L), 30mm (W) and 10mm (H), Fig. 1a.

The Transwell method incorporates a static 2D cell culture, that requires the circulation of 0.5ml cell nutrition every 48 hours. To achieve the same renewal rate at the microfluidic system a **B**asic **F**low (BF) of 0.17μl/hour is required. Flow simulations have been conducted for 41 different flow values, up to $BF*5*10^4$ with a logarithmic step, to examine whether the flow profile affects the cell viability and the growth rate, Fig. 2. Additionally, flow experiments have also been performed to investigate the consistency between the theoretical and experimental data regarding the pressure to the flow cycle that ensures the waterproofness of the microfluidic system, Fig. 3a.

The sensitivity of the TEER measurement is determined by the homogeneity of the current field applied to the membrane of the TI [2]. In this study, the current density applied to the membrane has been simulated for an input current value of 1A. The geometry of the electrode applying the signal is a ring with inner 5.1mm (D) and outer 6.3mm (D). The sensing AgCl electrode is a 4mm (D) disk located at the centre of the ring Fig.1d, resulting to a homogenous current density applied to the membrane of the TI shown in Fig. 3b. The microfluidic system was evaluated with living cells and reliable data were extracted.

References

[1] B. Srinivasan, et al., "TEER Measurement Techniques for In Vitro Barrier Model Systems," J. Lab. Autom., vol. 20, no. 2, pp. 107–126, 2015
[2] J. Yeste, , et al., "Geometric correction factor for transepithelial electrical resistance measurements in transwell and microfluidic cell cultures," J. Phys. D. Appl. Phys., vol. 49, no. 37, 2016

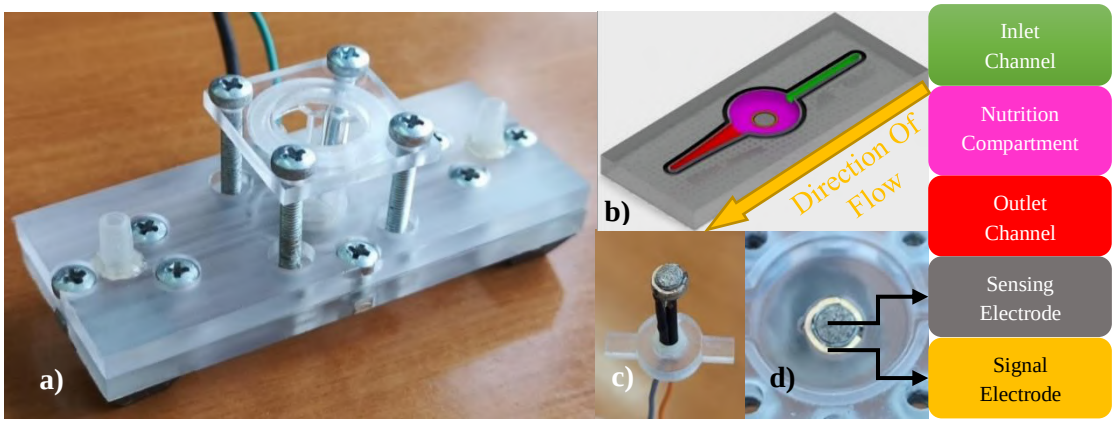

Figure 1.**a**) The Microfluidic Device with The Transwell Insert Attached, **b**) 3D Representation of the Base Part **c**) Upper Electrode **d**) Lower Electrode.

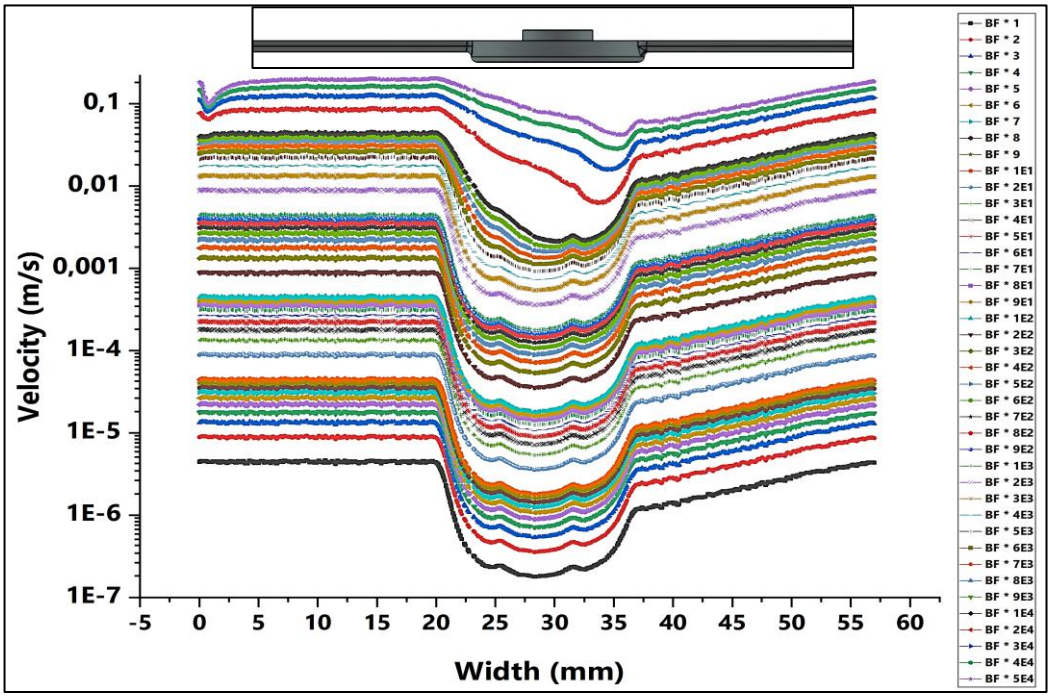

Figure 2. Flow profile along the length of the microfluidic device.

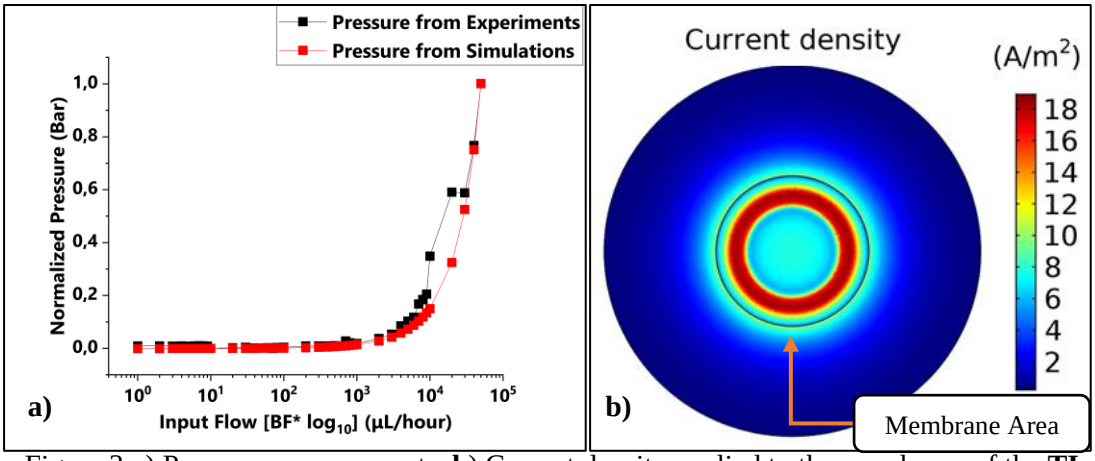

Figure 3.**a**) Pressure measurements, **b**) Current density applied to the membrane of the **TI.**

Sensors integrated in Organ-on-a-Chip microfluidic platforms

Dimitra Valadorou[1,2], Myrto - Kyriaki Filippidou[1], Dimitra Tsounidi[3], Dionysia Kefallinou[1], Panagiota S. Petrou[3], Stavros Chatzandroulis[1] and Angeliki Tserepi[1,*]

[1]Institute of Nanoscience and Nanotechnology, NCSR "Demokritos", Aghia Paraskevi, Attiki, Greece

[2]Physics Department, National Technical University of Athens, 15780 Zografou, Greece

[3]Institute of Nuclear & Radiological Sciences & Technology, Energy & Safety, NCSR "Demokritos", Aghia Paraskevi, Attiki, Greece

*a.tserepi@inn.demokritos.gr

Organ-on-a-chip (OoC) is a promising technology for mimicking the complexity of the human body environment, therefore it provides an alternative, preferable to conventional preclinical models for drug screening, where cell cultures and animal studies often fail.[1] However, there is a lack of continuous, non-invasive, and real-time monitoring, that remains one of the biggest challenges in OoC technology, as most current approaches rely on off-chip analysis and imaging techniques.[2] In the present work, we present an OoC-based microfluidic platform with an integrated biosensor for protein detection. The chip consists of an apical channel separated from a bottom reservoir by a porous membrane suitable for cell culture (Fig. 1). The upper micro-channel was fabricated by a master mold, constructed through photolithography of dry photoresist on the surface of PCB, and then casting of PDMS into the master mold. The bottom reservoir was made from a cured PDMS piece with a cut-out rectangle, and was bonded with the microfluidic channel and the porous polyester membrane, using plasma-induced surface modification. A microfluidic channel with integrated graphene oxide (GO) biosensors is connected in series with the chip (Fig. 2a), to detect, in this work, interleukin-6 (IL-6). IL-6 is a proinflammatory cytokine that increases early in the serum of patients with trauma, injury, or inflammation,[3] recently proven to be also a successful target to control inflammation.[4] The sensing area of the microfluidic channel consists of 3 pairs of gold electrodes (0.25 x 0.22 mm), at a distance of 3 mm, patterned on a commercially fabricated PCB substrate. For the fabrication of the transducer layer, graphene oxide is first drop-casted between the two gold electrodes and then is thermally reduced via a mild thermal treatment at 180°C for 1h. Afterwards, a PDMS micro-channel is sealed on the sensor area by using a spin-coated thin layer of PDMS, as a planarizing layer over the metal tracks (Fig. 2b). Reduced graphene oxide (rGO) allows the direct immobilization of the IL-6 specific antibody through adsorption.[5] Thus, IL-6 gets captured by the antibody immobilized on the sensor, and a resistance change is measured which is proportional to the IL-6 concentration in the solution

run over the sensors. Preliminary experiments indicate that IL-6 can be detected in the course of a few minutes at concentrations of a few ng/ml. In addition to IL-6, other biomarkers such as the Kidney Injury Molecule (KIM-1), a transmembrane protein that serves as a tissue marker for renal injury, are planned to be detected with the presented graphene oxide sensor integrated in our OoC platform, useful for cytotoxicity studies of drugs.

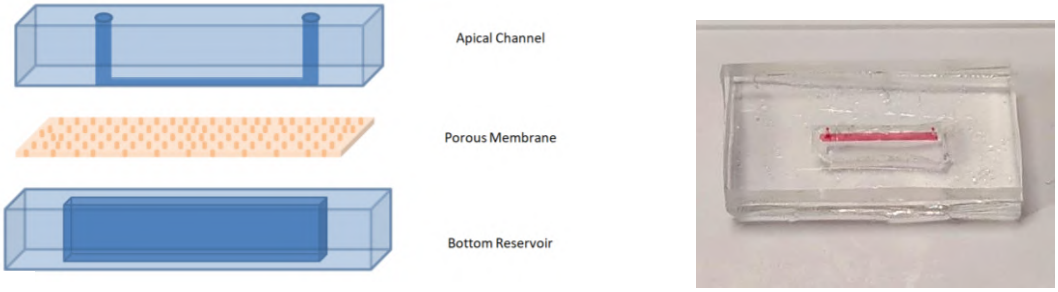

(a) (b)

Fig. 1 (a) Schematic representation of the OoC platform. (b) OoC microfluidic platform with red colored water for micro-channel visualization.

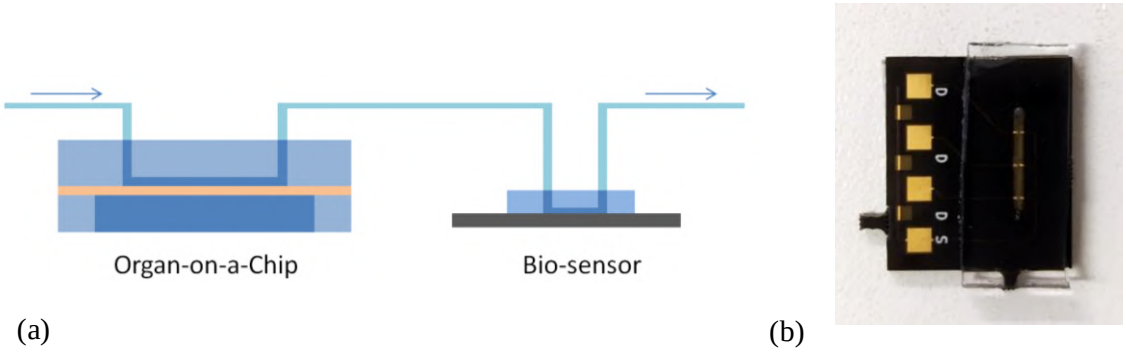

(a) (b)

Fig. 2 (a) Bio-sensor connected in series with the OoC. (b) Bio-sensor with a PDMS micro-channel on top.

[1] Kim, Sejoong, and Shuichi Takayama. "Organ-on-a-chip and the kidney." Kidney research and clinical practice 34.3 (2015): 165-169.
[2] Ferrari, Erika, et al. "Integrating biosensors in organs-on-chip devices: A perspective on current strategies to monitor microphysiological systems." Biosensors 10.9 (2020): 110.
[3] Song, Mingchen, and John A. Kellum. "Interleukin-6." Critical care medicine 33.12 (2005): S463-S465.
[4] Rincon, Mercedes. "Interleukin-6: from an inflammatory marker to a target for inflammatory diseases." Trends in immunology 33.11 (2012): 571-577.
[5] Filippidou, M. K., et al. "Detection of BRCA1 gene on partially reduced graphene oxide biosensors." Microelectronic Engineering 216 (2019): 111093.

Quantum walks on graphene nanoribbons under the effect of external potentials

Georgios D. Varsamis[1,*] and Ioannis G. Karafyllidis[1,2]

[1] Department of Electrical and Computer Engineering

Democritus University of Thrace

Xanthi, 67100, Greece

[2] Research Associate National Centre for Scientific Research Demokritos

Athens, 15342, Greece

*gevarsam@ee.duth.gr

Quantum gate model is the most popular model of quantum computation. Despite that, many physical problems are difficult to implemented directly as quantum circuits. Quantum walks, introduced by Aharonov et al. in 1993[1], are proven to be a universal and equivalent model for quantum computation to the dominant quantum gate model[2]. Quantum walks can directly be mapped onto quantum circuits and executed by quantum computers[3,4,5] and can also be implemented in various platforms[6]. Physical problems that quantum walks have been utilized are quantum transport in graphene[7] , simulation of bosonic and fermionic quantum systems[8], as well as finding the lowest eigenstate of tight binding Hamiltonians[9], among others. In most cases the quantum walk evolution occurs in free spaces, meaning that the motion of the walker is not affected by external stimuli, but rather form the structure of the evolution space. Although, as all quantum systems, so can quantum walks be described by the Schrödinger equation. The Hamiltonian operator comprises a kinetic and a potential energy term. By utilizing the quantum field effect operator and the quantum annihilation and creation operators, we introduce an external potential to the evolution space. The quantum walker now carries a "charge", which is affected from the external applied potential. We considered the case of the graphene honeycomb lattice to act as the evolution space of the discrete time quantum walk, presented in Fig. 1. The probability distribution of the quantum walker localization is associated with the electron density[7]. We introduce a linear applied potential to the evolution space (Fig. 2(a)). Our results show that the particle motion is affected by the potential and that the walker's location probability distribution tends to shift towards the lower potential (Fig. 2(b)). The study of carrier transport properties in nanostructures is a very important problem and it is approached with the combination of tight binding Hamiltonians and the NEGF method[10,11] . In this paper we investigate the possibility of using discrete time quantum walks evolving in spaces where external potentials are applied, to compute the conductance of nanomaterials and especially of graphene.

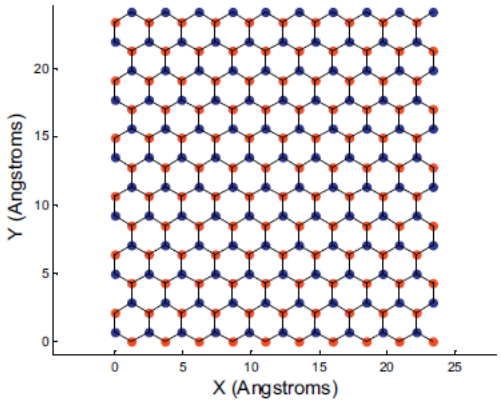

Fig.1 Graphene nanoribbon. The honeycomb graphene lattice serves as the evolution space and comprises two sub-lattices, indicated by red and blue dots.

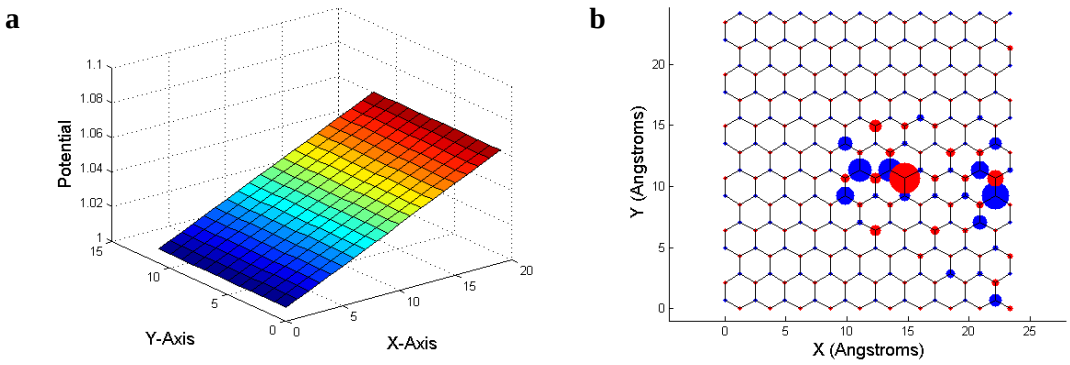

Fig.2 (a) Linear applied potential, (b) probability distribution of the walker's location at the 20th time step. Walker's initial location is at the middle right on the graphene lattice

[1] Y. Aharonov, L. Davidovich, and N. Zagury, Phys. Rev. A, 48, 1687 (1993)
[2] N. B. Lovett, S. Cooper, M. Everitt, M. Trevers, and V. Kendon, Phys. Rev. A, 81, 042330 (2010)
[3] B. L. Douglas and J. B. Wang, Phys. Rev. A, 79, 052335 (2009)
[4] T. Loke and J. B. Wang, Phys. Rev. A, 86, 042338 (2012)
[5] F. Acasiete, F. P. Agostini, J. K. Moqadam and R. Portugal, Quantum Inf. Process., 19, 426 (2020)
[6] J. Wang, K. Manouchehri, Physical Implementation of Quantum Walks, Springer Berlin, Heidelberg, 2014 (39)
[7] I. G. Karafyllidis, J. Comput. Sci., 11, 326 (2015)
[8] L. Sansoni, F. Sciarrino, G. Vallone, P. Mataloni, A. Crespi, R. Ramponi, and R. Osellame, Phys. Rev. Lett., 108, 010502 (2012)
[9] G. D. Varsamis and I. G. Karafyllidis, Int. J. Quantum Inf., 20, (2022)
[10] S. Datta,Superlattices Microstruct., 28, 253 (2000)
[11] I. G. Karafyllidis,IEEE Trans. Nanotechnol., 13, 820 (2014)

Random Telegraph Noise Analysis of RRAM Devices: A systematic approach on unstable filaments

Nikolaos Vasileiadis[1,2], Alexandros Mavropoulis[1], Panagiotis Loukas[1], Georgios Sirakoulis[2] and Panagiotis Dimitrakis[1]

[1] Institute of Nanoscience and Nanotechnology, NCSR "Demokritos", Ag. Paraskevi 15341, Greece

[2] Department of Electrical and Computer Engineering, Democritus University of Thrace, Xanthi 67100, Greece

*n.vasiliadis@inn.demokritos.gr

Abstract− Resistive memories (RRAMs) are one of the most anticipated non-volatile memory technologies. The crossbar architecture offers an excellent opportunity for achieving the smallest memory cell, a crucial component of in-memory and neuromorphic computing accelerators, and the ensuing development in low power mobile IoT edge computing hardware. RRAM cells are ideal for this architecture. However, there are a lot of challenges until commercialization in all fabrication levels including the physics behind the resistive switching phenomenon. The analysis of low-frequency noise signals generated by semiconductor devices yields important knowledge about their physical mechanisms and origin, commonly related to the presence of traps, enabling the reduction of noise sources and enhancing device performance. Specifically, random telegraph noise (RTN) analysis can provide important information about the energy of the traps and their mobility thus playing an important role in the fine tuning of the device. Furthermore, multi-level resistive tuning is a fundamental desired aspect on all RRAM devices to be used in neuromorphic computing. It has been observed that several resistance states are not stable in time and noise analysis of such signals becomes a difficult procedure. For this reason, we propose a method by which we can remove the unwanted fluctuations while stabilizing the RTN signal that concerns us. This method is based on the removal of the disturbing signal causing the instability through average detrending according to relation (1) :

$$I_s[t] = I_o[t] - (I_o * G)[t] + \overline{I_o[t]}, \quad G[t] = \left[\underbrace{1/M, 1/M, \dots, 1/M}_{M\ times}\right] \qquad (1)$$

where I_s and I_o are the stabilized and original RTN signal, respectively and G is the filtering mask. In fig. 1, the noise signal from a SiN-based memristor is demonstrated. The region of the signal (green) that shows a significant current drop due to a remarkable filament's instability is completely removed (fig. 2). Moreover, the micro-fluctuations at the beginning of the signal (fig.1 - blue region) disappeared as shown in the inset of fig. 2. The performance of this method becomes clearer in fig. 3 where in the case of the original signal's histogram the levels detected by the multi-Gaussian fitting method are completely off. After de-trending, the histogram of the stabilized signal has two peaks and with less deviation. As for the new mean value of the

stabilized signal, it was defined as the mean value of the original resistive level. The original histogram (Fig. 3 - Grey) now represents the maximum variation of the mean value of the stabilized signal. The power spectra density (PSD) S_I of the RTN signal is not affected by the proposed stabilization method as shown is fig. 4. Evidently, the high frequency regime ($f > f_T$ =1058Hz) in the S_I remains intact. The value of this method becomes more obvious with fig. 5 where the estimated trapping levels decoupled from the signal instabilities and thus the dwell times (Fig. 6) of these levels are estimated accurately.

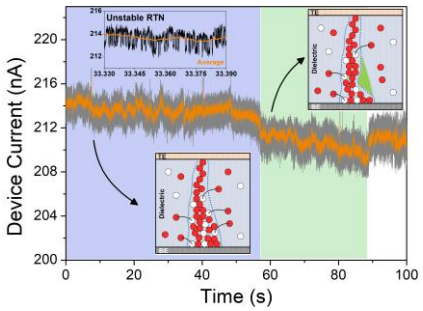

Fig. 1 Original RTN signal along with average signal. Insets show the trapping/de-tarping phenomenon along with filament deformation due to generation/ recombination of defects (green region).

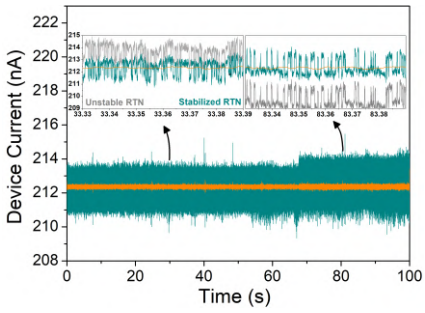

Fig. 2 Stabilized RTN signal after the average de-trending method which was described above.

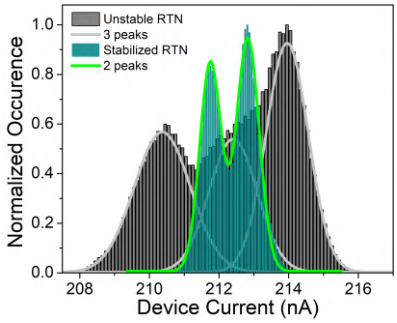

Fig. 3 Comparison of normalized occurrences in original and stabilized signal.

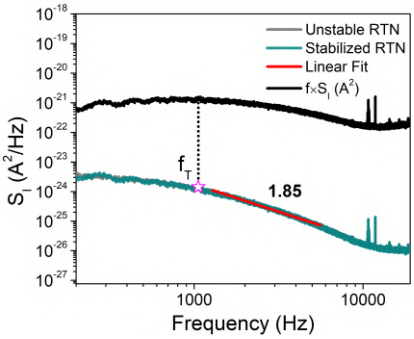

Fig. 4 PSD plots of the original and the stabilized RTN signal.

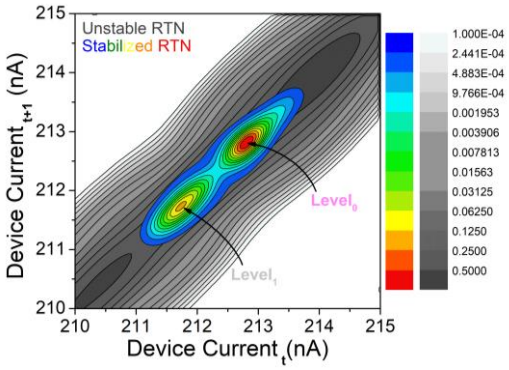

Fig. 5 Weighted time lag plots of the original and the stabilized RTN signal.

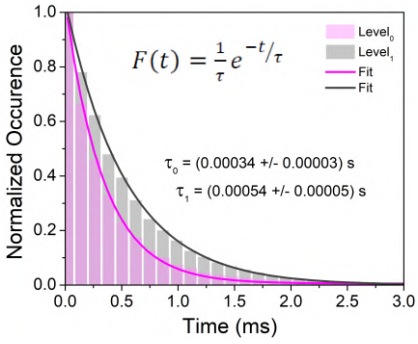

Fig. 6 Accurate extraction of the traps' dwell times through stabilized RTN signal.

Field emission from a subnanometric carbon tip: experiment and theory

J.P. Xanthakis[1,*], P.A. Zestanakis[1] and V.I. Kleshch[2]

[1]ECE Dept National Technical University of Athens Zografou Campus Athens 17500 Athens Greece

[2]Lomonosov Moscow State University, Moscow Russia

*jxanthakcentral.ntua.gr.

Abstract text[1] We report a combined experimental and theoretical investigation on a subnanometric carbon tip with the apex radius of 0.8 nm. The tip was created by field-emission assisted structural modification of a diamond needle-like crystal [1], see figure1. The field emission current-voltage characteristics were measured at a distance of 500 μm between the tip and a flat anode. In particular, a current of less than 1 nA was achieved at a voltage of 80 V. Electrostatic modeling based on TEM images showed that at this voltage the electric field at the emitter apex is about 15 V/nm. When the Fowler- Nordheim (FN) theory was employed to predict the current using the calculated value of the electric field the result was $4*10^4$ nA. On the other hand when the Simmons theory was employed using the calculated full potential variation along the axis the result was 10^3 nA – a minor improvement on the FN result. Using the generalized FN for nanoscopic emitters [2] did not help either. Satisfactory agreement between theory and experiment that eliminates this difference of orders of magnitude was accomplished when a theory [3] that takes account of the serious distortion of the wavefunctions is employed. This theory is not using simple plane waves for the electron states but takes due account of the emitter shape, see figure2 and takes account also of localization effects. The supply of electrons function of this emitter is radically different from the traditional Fowler-Nordheim one. The implications are discussed.

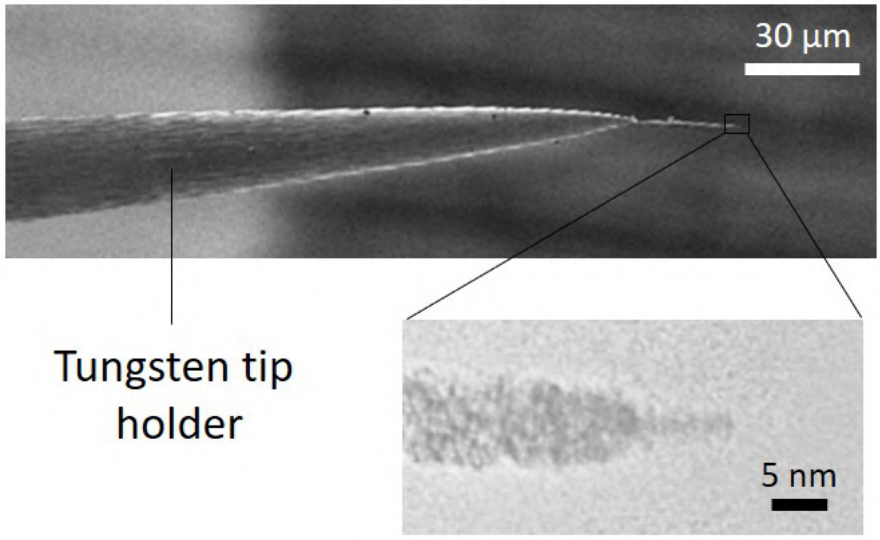

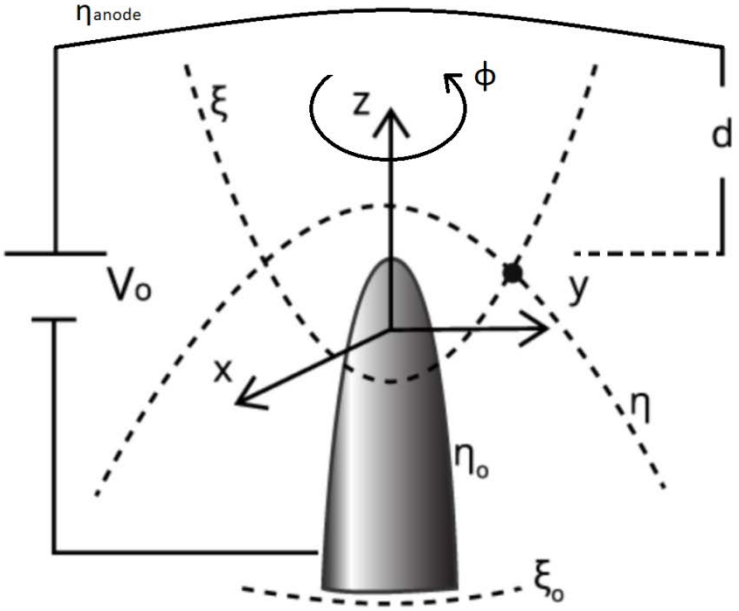

[1] V. I. Kleshch, V. Porshyn, A. S. Orekhov, A. S. Orekhov, D. Lützenkirchen-Hecht, and A. N. Obraztsov, *Carbon single-electron point source controlled by Coulomb blockade*, Carbon 171, 154 (2021).

[2] A. Kyritsakis and J.P. Xanthakis *Derivation of a generalized Fowler–Nordheim equation for nanoscopic field-emitters, Proc. R. Soc. A 471, 2014 (2015).*

[3] A. Chatziafratis and J. Xanthakis, *Field emission from a nanometric paraboloidal emitter*, Journal of Electron Spectroscopy and Related Phenomena **241**, 146871 (2020).

The use of microsensors for in-operando monitoring of internal pressure in lithium-ion batteries

Anestis Topalidis, George Zardalidis*, Filippos Farmakis

Department of Electronics and Computer Engineering, Democritus University of Thrace, Xanthi, 67100, Greece

*gzardali@ee.duth.gr

The evolution of gas in lithium-ion batteries (LIBs) at a charged state is one of the main problems in the industry because it causes significant distortion or swelling of the batteries that can lead to uncontrolled explosions. However, measuring gas pressure is an additional source of information about the state of the battery life. The scope of this study is the in-operando sensing of the internal pressure of different battery cells in order to study and benchmark the behaviour for a microsensor application. The study covers different active materials such as graphite and silicon for the anode as well as different electrolytes, while Lithium Iron Phosphate (LFP) is used as a cathode material. The battery cells were subjected to various charging/discharging cycles in order to evaluate the impact of different C-rates on their internal pressure. The cycles were performed at ambient temperature. According to the obtained results, it can be deduced that the pressure of the cell with the salt LiPF6 presents remarkable variations during the formation phase compared to the cells with the salt LiTFSI as can be seen in fig. 1, leading to the production of more gases.

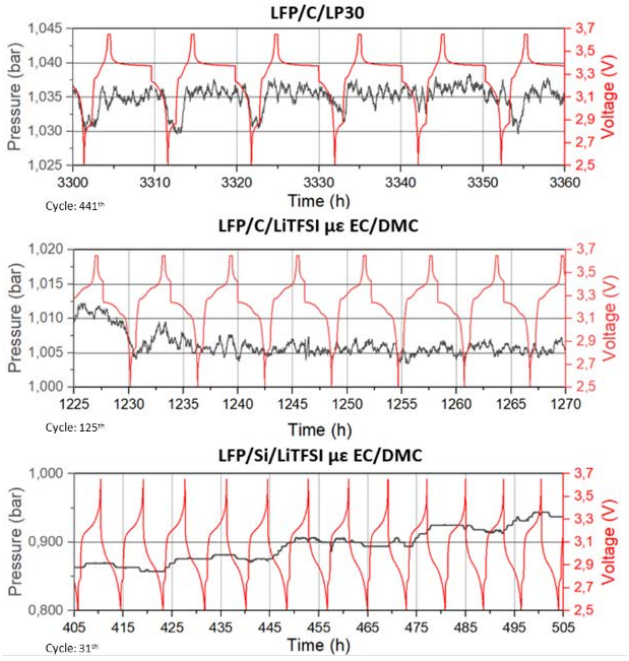

Fig.1 The evolution of pressure inside the battery with graphite anode and LFP cathode with LP30 (top), EC/DMC (middle) and silicone anode and EC/DMC electrolyte (bottom).

Moreover, during the cycling tests, it has been observed that the internal pressure and the voltage of the cell with LiPF6 salt present the same variations, i.e., when the voltage increases, the pressure increases as well. On the other hand, the pressure of the cell with graphite anode and LiTFSI salt has not been significantly modified during the switching between the charging and discharging process. Finally, it can be generally observed that the pressure of the cell with silicon anode decreases with operating cycles up to a certain extent; for higher values, the pressure starts increasing denoting the cell aging.

Microring Resonator-Assisted Semiconductor Optical Amplifier Direct Amplification and Modulation

Zoe V. Rizou[1] and Kyriakos E. Zoiros[2,*]

[1]University of Western Macedonia, Department of Electrical and Computer Engineering, Kozani, Greece

[2]Democritus University of Thrace, Department of Electrical and Computer Engineering, Lightwave Communications Research Group, Xanthi, Greece

*kzoiros@ee.duth.gr

Semiconductor optical amplifiers (SOAs) are key elements in optical communications circuits, systems and networks. The primary use of SOAs is to provide straightforward signal amplification (Fig. 1(a))[1]. Furthermore, SOAs can be used as external modulators (Fig. 1(b)) to provide both data amplification and modulation[2]. However, enabling these functions is challenging due to the SOA finite carrier lifetime[1]. This intrinsic limitation does not allow to achieve direct amplification in a SOA which is heavily saturated by the input data, or data encoding at rates well beyond the SOA electrical bandwidth. In fact, the pattern effects that manifest in both cases are deleterious for the quality of the amplified (Fig. 1(a)-circled point '1') or encoded (Fig. 1(b)-circled point '1') signal and result in performance degradation. In the effort to mitigate these effects and help employ SOAs for linear amplification or intensity modulation purposes, it is proposed here to exploit a microring resonator (MRR) as optical notch filter. This is possible when the MRR operates in the critical coupling regime, where the microring internal losses are equal to the coupling losses[3]. The MRR is connected at the SOA output and compensates for the instantaneous frequency deviation components induced due to the irregular SOA gain variation. The impairments associated to these components are converted by the MRR response into amplitude changes which counteract those after the SOA[4].

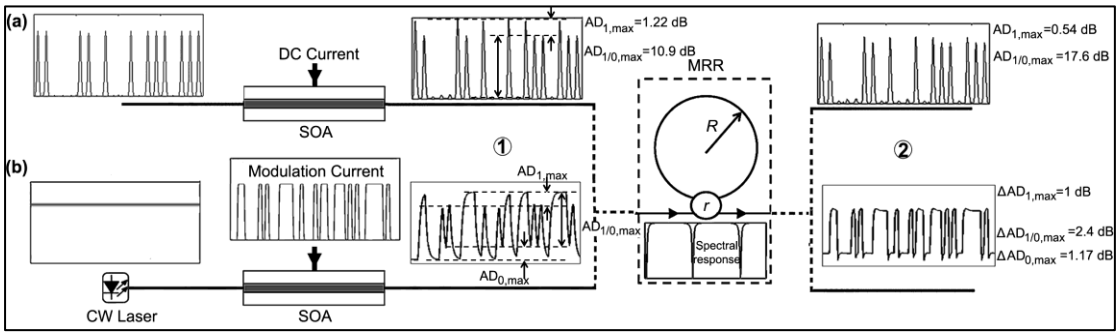

Fig. 1. Configuration of MRR-assisted SOA in direct amplification (a) or modulation (b). $AD_{1,max}$ and $AD_{1/0,max}$ denote the maximum amplitude difference between marks and between marks and spaces, respectively.

The SOA response, *h(t)*, obeys the following general ordinary differential equation[5]

$$dh_{i=1,2}(t)/dt = \left\{ \Gamma \alpha N_{tr} \left[\frac{I_{i=1,2}(t)}{I_{tr}} - 1 \right] L - h_{i=1,2}(t) \right\} \Big/ T_{car} - P(t)_{i=1,2} \left\{ \exp\left[h_{i=1,2}(t) \right] - 1 \right\} \Big/ E_{sat} \quad (1)$$

where the involved SOA physical parameters are the confinement factor, Γ, differential gain, α, carrier density, N_{tr}, transparency current, I_{tr}, active region length, L, carrier lifetime, T_{car}, and saturation energy, E_{sat}. For SOA direct amplification of return-to-zero data of varying power $P(t)$, or $i = 1$, $I(t) = I_{dc}$, where I_{dc} is the SOA constant dc bias current, while for SOA direct modulation by a varying current, $I(t)$, or $i = 2$, $P(t) = P_{CW}$, where P_{CW} is the power of a continuous wave optical beam on which the electrical non-return-to-zero data are encoded. The SOA output electric field is then $E_{SOA_{i=1,2}}(t) = \sqrt{P_{i=1,2}(t)} \exp\left[(1 - ja) h_{i=1,2}(t)/2 \right]$, where a is the SOA linewidth enhancement factor. The MRR output electric field is $E_{MRR}(t) = F^{-1}\left\{ F\left[E_{SOA}(t) \right] T_{MRR}(\lambda) \right\}$, where $F[\bullet]$ and $F^{-1}[\bullet]$ stands for the Fourier Transform and its inverse implemented through the Fast Fourier Transform (FFT) and Inverse FFT operations, respectively, available in Matlab software. The MRR spectral response is[3] $T_{MRR}(\lambda) = \left\{ r - \tau \exp\left[jn_{eff} 4\pi^2 R \left((\lambda - \Delta\lambda)/\lambda^2 \right) \right] \right\} \Big/ \left\{ 1 - r\tau \exp\left[jn_{eff} 4\pi^2 R \left((\lambda - \Delta\lambda)/\lambda^2 \right) \right] \right\}$, where r, τ, R and $\Delta\lambda$ are the MRR field transmission coefficient, round-trip amplitude attenuation factor, radius and detuning, respectively.

By conducting numerical simulations, it has been possible to find a suitable combination of (R, $\Delta\lambda$) which strongly suppresses the SOA pattern-dependent distortion for both target applications. In the first case, R = 28 um, and the MRR is detuned so that its transmission peak lies on the left-hand side of the data carrier by less than 11%. In the second case, R = 20 um, and the MRR is detuned so that the wavelength offset between the data carrier and its shorter sideband transmission peak is 4.8%. In this manner, the MRR reduces the pronounced peak amplitude fluctuations on the amplified 10 Gb/s return-to-zero data signal down to approximately 0.5 dB, and increases the pulses' extinction ratio up to nearly 17.5 dB (Fig. 1(a)-circled point '2'). When the SOA is directly modulated at a data rate which is more than five times faster than that enabled by its electrical bandwidth, the MRR makes pulses of the same binary content more uniform in amplitude by at least 1 dB, and enhances the amplitude discrimination between pulses of different binary content within the encoded non-return-to-zero data stream by almost 2.5 dB (Fig. 1(b)-circled point '2'). The design of a MRR according to these specifications is practically feasible[3]. Therefore, the MRR can assist employing SOAs as direct amplification and modulation elements with high performance.

[1] M. J. Connelly, Semiconductor Optical Amplifiers, Kluwer Academic Publishers, 2002
[2] E. Udvary and T. Berceli, IEEE Trans. Microwave Theory Techn., 58, 3161-3166 (2010)
[3] D. G. Rabus, Integrated Ring Resonators: The Compendium, Springer-Verlag, 2007
[4] J. Wang, et al., IEEE Photon. Technol. Lett., 19, 1955-1957 (2007)
[5] G. P. Agrawal and N. A. Olsson, IEEE J. Quantum Electron., 25, 2297-2306 (1989)

Analysis of Quantum Computing Surface Codes implemented on Quantum Dot spin-based systems

Konstantinos Prousalis*, Chrysostomos Panis, Dimitrios Ntalaperas, Lefteris Angelis and Nikos Konofaos

School of Informatics, Aristotle University of Thessaloniki, Thessaloniki, Greece

*kprousalis@csd.auth.gr

Electron spins in quantum dots provide a promising platform for Quantum Computation (QC) [1-2], forming suitable systems for qubit creation. Quantum computation errors in the form of noise exist and all identified types of such noise effects could be considered under the umbrella of the measured charge and spin noise [3], both having a direct impact on qubit performance. Here, an analysis of the total amount of noise concerning multi qubit system, is addressed via calculations of the survival probability when a so called "surface code", which is an error correction code, is executed.

This study aims to manipulate the aggregated amount of noise by exploiting the discrete identification of noise mechanisms. Our simulation model is highly based on the classification of the relevant spin-relaxation processes as they are proposed in [4]. The main contributions to electron spin-dephasing (T_2^*) in a Quantum Dot (QD) spin-based QC system are summarized in Table 1. The term "decoherence" (T_2 time) refers to a single qubit and "dephasing" (T_2^* time) refers to the phase relaxation of a QC system consisting of many qubits (i.e., single-electron spin in a QD). Dephasing is therefore caused by decoherence ($T_2 \geq T_2^*$). The processes that cause phase diffusion of the multiqubit system without resulting in decoherence in the individual qubits are referred to as "random local fields" in this category. The decoherence or transversal relaxation has contributions from both the elastic and inelastic processes. The inelastic processes involve spin-flip transitions that result in the relaxation of the spin states energy (or longitudinal), i.e. T_1. The spin-phonon interaction induces the spin decoherence processes denoted by **. The uncontrollable interactions with the environment that are thought to be in a thermodynamic equilibrium are represented by the listed T_2 processes.

Dephasing (T_2^*)								
Decoherence (T_2)						***Random local fields***	***Rate***	***p-value***
Inelastic process (T_1)	***Rate***	***p-value***	***Elastic process***	***Rate***	***p-value***			
*V1: Direct spin flip***	*10%*	*$66*10^{-5}$*	*V5: Anharmonic vibration***	*2%*	*0.1*	*V9: g-tensor dispersion*	*1%*	*0.34*
*V2: Orbach***	*1%*	*0.6*	*V6: Local-field steps***	*3%*	*0.97*	*V10: Dispersion of HFI*	*1%*	*0.97*
*V3: Two phonon***	*5%*	*0.94*	*V7: Spectral diffusion*	*1%*	*0.22*	*V11: Impurity fields*	*-*	*-*
V4: Nuclear spins	*75%*	*$2*10^{-16}$*	*V8: Geometric phase***	*1%*	*0.6*	*V12: Interqubit interaction*	*-*	*-*

Table 1. Identified and classified contributions to electron spin-dephasing (T_2^*) in a QD spin-based QC system. The decoherence (aka transversal relaxation - T_2 time) of a single spin is affected from both elastic and inelastic processes. The "random local fields" list mentions the mechanisms that lead to phase diffusion of the multiqubit system without causing decoherence in the individual spin- qubits. The inelastic processes also involve spin-flip transitions that lead to the energy (or longitudinal) relaxation of the spin states (in T_1 time). The spin-relaxation processes induced by the spin-phonon interactions are denoted by **. HFI means hyperfine interaction.

In this study we focus on the experimentally mature architecture of self-assembled QDs such as the example Schottky diode [4] which is described in Fig. 1. Decoherence sources producing unwanted noise include magnetic noise among others, and the relevant contributions of each one of them are described in [4-8]. Profoundly, all types of noise sources do not equally contribute to the relaxation mechanism and this is what we are going to formulate: the fair contribution of each noise source either on a single qubit or the overall qubit system. Many processes behave in a stochastic way rendering necessary the employment of statistical tools for a reliable noise estimation.

Quantum error correction codes such as the Surface [9] code [[5,1,2]] (see Fig.1) are used to correct noise in QC systems. A generic Pauli noise model is employed to simulate surface systems which are subject to amplitude damping (T1) and dephasing (T2) types of noise. The characteristic time intervals of T_2 *and* T_2^* play a critical role (since $T_1 > T_2$ *and* $T_2 > T_2^*$) for the lifetime of a qubit as they determine their coherent operation or stability. Noise processes are described by the parametric global model of Pauli noise, which is defined by a set of 3 probabilities symbolized as [P_X, P_Y, P_Z]. These probabilities define respectively the probability of a Pauli X, Y, or Z gate operator getting applied to each qubit after each time step in idleness. The iterative random sampling of Monte-Carlo method was used to simulate noise behaviour in the [[5,1,2]] and [[13,1,3] surface codes.

The statistical model of survival curves was employed to analyze the surviving probability for both codes for the many variables of noise. By the occurrence of 3 or more and 7 or more data qubit errors, the system is considered collapsed for the [[5,1,2]] and [[13,1,3]], respectively. In the first plot in Fig. 2, the

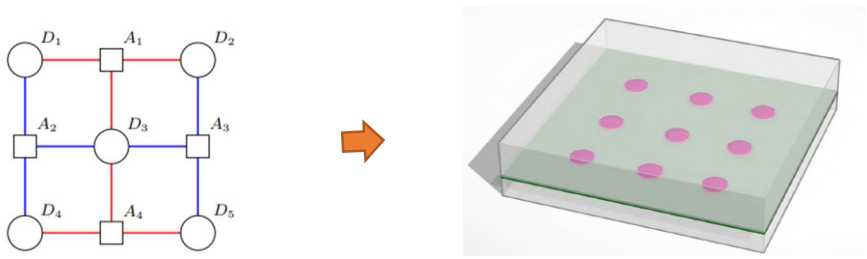

Fig.1 (a) Surface code [[5,1,2]]: 5 data and 4 ancilla qubits (b) Quantum dot nano-structure.

[[5,1,2]] is analyzed for three different error probability ranges 0-0.5%, 0.5-1%, 1-1.5%. In the second plot, the same analysis was conducted for the [[13,1,3]], where we observe that the median survival time for code [[13,1,3]] is almost 3 times longer than that of code [[5,1,2]]. We also see that for the first 250 time-units the [[13,1,3]] code reaches survival rates of 99% while the [[5,1,2]] code is at 65%. After 1000 time-units [[13,1,3]] survives with almost 50% probability while [[5,1,2]] survives with less than 10%.

Cox regression was also used to allocate in a proportional way the significance (rates) of each source of noise. The proportional allocation that was adopted in Table 1 is based on data proposed in [6,8]. The expected survival probability was calculated as a function of time which is related to the evolution of P_X, P_Z, and the adopted type of surface code. If a variable (noise source) does not significantly affect the survival time, it can be omitted from the prediction model without a large deviation in its accuracy. This is observed by calculating the p-value for each variable as in Table 1, if p-value > 0,05 it has no significant effect, while if p-value < 0,05 it has a significant effect. The statistical framework of R was used to estimate the time needed till the collapse of the code system.

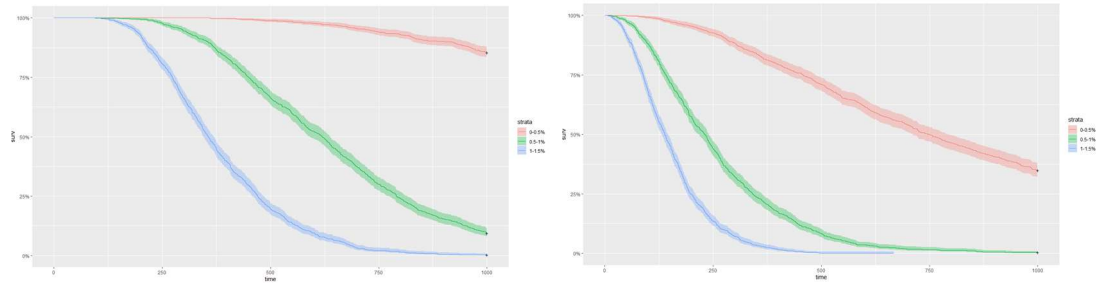

Fig. 2. Survival probability along time evolution for the [[5,1,2]] (on the left) and [[13,1,3]] (on the right) surface codes.

A comparison between the two codes is also conducted in Fig. 3. Over a general range of error probabilities from 0 to 1%, we observe that the median survival time for the [[13,1,3]] code is almost 3 times longer than that of the [[5,1,2]] code. We also see that for the first 250 time-units the [[13,1,3]] code reaches survival rates of 99% while the [[5,1,2]] code is at 65%. After 1000 time-units [[13,1,3]] survives with almost 50% probability while [[5,1,2]] survives with less than 10%.

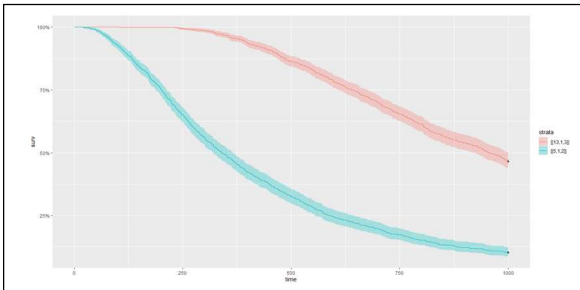

Fig. 3. Survival curves for code [[5,1,2]] (blue) and code [[13,1,3]] (red), with both P_X and P_Z, having error probability range 0-1%.

This statistical analysis provides a clear view of the contributing noise sources bridging the gap between theoretical and experimental studies. The multi-qubit surface encoding system is a promising modular system for large scale architecture in QC. The broader framework of all noise types has to be developed in a library for more demanding simulating projects. Furthermore, comparison with realistic data could help realize the relationship between noise sources and survival perspectives of surface encoding systems.

References

[1] Loss, D. & DiVincenzo, D. P. Quantum computation with quantum dots. *Phys. Rev. A* 57, 120–126 (1998).
[2] Ladd, T., Jelezko, F., Laflamme, R. *et al.* Quantum computers. *Nature* 464, 45–53 (2010).
[3] Kuhlmann, A., Houel, J., Ludwig, A. *et al.* Charge noise and spin noise in a semiconductor quantum device. *Nature Phys* 9, 570–575 (2013).
[4] K Prousalis, AA Iliadis, EK Evangelou, N Konofaos. Noise investigation in a spin-based four-qubit GaAs block of self-assembled quantum dots AIP Advances 11 (6),2021, 065126.
[5] Semenov, Yuriy G. and K. W. Kim. Elastic spin-relaxation processes in semiconductor quantum dots. *Physical Review B* 75 (2007): 195342.
[6] Bluhm, H. et al. Dephasing time of GaAs electron-spin qubits coupled to a nuclear bath exceeding 200 μs. *Nat. Phys.* 7, 109–113 (2011).
[7] Malinowski, F., Martins, F., Nissen, P. *et al.* Notch filtering the nuclear environment of a spin qubit. *Nature Nanotech* 12, 16–20 (2017).
[8] Urbaszek, Bernhard, et al. Nuclear spin physics in quantum dots: An optical investigation. *Reviews of Modern Physics* 85.1(2013): 79.
[9] Fowler, A. G., Mariantoni, M., Martinis, J. M., & Cleland, A. N. (2012). Surface codes: Towards practical large-scale quantum computation. *Physical Review A*, *86*(3), 032324.